Regularized Statistical Material Decomposition in Medical Imaging

by

Won Seok Huh

A dissertation submitted in partial fulfillment
of the requirements for the degree of
Doctor of Philosophy
(Electrical Engineering : Systems)
in The University of Michigan
2011

Doctoral Committee:

Professor Jeffrey A. Fessler, Chair
Professor Mitchell M. Goodsitt
Professor Douglas C. Noll
Assistant Professor Clayton D. Scott

TABLE OF CONTENTS

LIST OF FIGURES

Figure

LIST OF TABLES

Table

CHAPTER 1

Introduction

In viewing underlying pathology with medical imaging, often specific material components contain most of the diagnostic information. Therefore, material component separation is desirable in many medical applications. Recent generations of MRI and X-ray CT systems can collect multiple measured data sets by changing data acquisition parameters, *e.g.*, pulse sequence timing parameters in MRI and X-ray tube voltages in CT. These systems allow one to separate images of material components.

In this thesis, we present novel image decomposition methods for MRI and X-ray CT applications. These methods use regularization and multiple data sets. We also propose iterative algorithms to minimize appropriate regularized least-squares cost functions that are defined by a weighted least squares data fit term and a regularization penalty. Experiments on synthetic data and phantom data suggest that our methods can improve the quality and accuracy of the estimated images compared to conventional methods for material separation.

1.1 Water-Fat Decomposition in MRI

Separating water and fat components is desired in many MRI applications. The major motivation of this work is that the fat signal can obscure underlying pathology in the water

image, which often contains the majority of the diagnostic information [49].

In designing pulses and algorithms for magnetic resonance imaging, several simplifications to the Bloch equation are often used, such as ignoring magnetic field inhomogeneity, quantified spatially by a field map, and the chemical shift effect. As a case in point, the nuclear spin of ^1H in an object resonates at about 42.58 (MHz) when the object is placed in a 1T main field by the Larmor equation which is the precession of the magnetic moments about an external magnetic field. However, in practice, a specific spin system may have a range of resonance frequencies because of the chemical shift effect and magnetic field non-unformity map.

When the main field is not homogeneous, spins with the same gyromagnetic ratio in the Larmor equation will have different resonance frequencies at different spatial locations. The chemical shift effect is caused by the orbital motion of the surrounding electrons. A well-known example is that ^1H protons in "fat" tissue in biological objects have about a 220Hz shift in resonance frequency from "water" protons at 1.5T. By using this chemical shift effect, we can separate water and fat images in MR imaging.

In Chapter 4 and 5, we develop regularized methods for water-fat decomposition. We present a penalized-likelihood (PL) approach that includes a regularization term based on the smoothness of the field map. The water-fat component estimates are shown to be a function of the field map and hence the optimization problem reduces to a function of just the field map. Therefore, we can jointly estimate water components, fat components and the field map. We present an iterative algorithm that monotonically converges to a local solution. We also investigate a discretized ML implementation, which is a numerical search approach, and a penalized weighted least squares (PWLS) method. We used these simpler methods to initialize the PL algorithm. By providing a field map estimate that is inherently smooth even in regions of low signal intensity, the method may yield improved

water and fat images compared to conventional approaches.

1.2 Image Reconstruction for Dual-Energy Computed Tomography(CT)

In the field of X-ray CT, there is increasing interest in enhancing the information provided in the images through dual-energy imaging. Dual energy (DE) CT imaging was first proposed over 30 years ago [2], but only recently became available for routine use in clinical CT systems. Very recently, commercial systems with fast kVp switching have become available, extending an idea that previously existed only in prototype systems [31].

The conventional approach to DE CT imaging is the "dual rotate" mode where the source is rotated around the patient at one source voltage setting to collect a full set of data called a sinogram, and then the source voltage is changed (as quickly as the hardware permits) and the source is rotated around again with the new kVp to collect a second full sinogram. Using these two full sinograms, one can reconstruct separate images of two material components (such as soft tissue and bone) using sinogram material decomposition followed by conventional filter back projection (FBP) image reconstruction [2]. Model-based image reconstruction methods for fully sampled sinograms have also been proposed under monoenergetic [6, 61] and polyenergetic models [14, 48]. A drawback of this conventional "dual rotate" mode of DE CT is that the object may move between the two acquisitions, leading to inconsistencies between the two sinograms that can manifest as severe artifacts in the reconstructed images.

To reduce motion effects, the "fast kVp switching" mode alternates between high and low X-ray source tube voltages for the projection views. This allows DE data to be collected in a single rotation, so the motion artifacts should be comparable to those of conventional CT imaging. In this switching mode, two sinograms are collected with only half

as many projection views as could be collected otherwise.

The typical solution to this problem in fast switching DE imaging is to interpolate both sinograms in the angular direction to fill in the "missing" views. Then one can apply conventional sinogram domain DE decomposition followed by FBP reconstruction. However, such interpolation might compromise spatial resolution. Furthermore, DE decomposition is a noise-amplifying process, so statistical image reconstruction methods have the potential to improve image quality significantly relative to FBP in all types of DE imaging [14].

In Chapter 7, 8, and 10, we have investigated model-based image reconstruction methods for DE CT that reconstruct two material component images. In this work we focus on PWLS methods that estimates two material components from fast kVp-switching. We then combine those material component images estimates at 511 keV and reproject at the positron emission tomography (PET) resolution to form attenuation correction factors (ACFs). Accurate ACFs are essential in PET image reconstruction to make high quality, quantitively accurate emission images. By using suitable regularization methods applied to the basis material density images, the proposed method has the potential to improve ACF accuracy compared to previous sinogram-domain approaches [37, 46].

1.3 Thesis outline and Contributions

In this thesis, the overall goal is separating material images from medical images such as MRI and CT images. We proposed two statistical methods to separate water and fat material components in MR image and two model-based iterative algorithms to reconstruct material images in CT image:

- Iterative water-fat decomposition algorithm with regularized field map estimation.

  The method in Chapter 4 can estimate water components, fat components, and a field map with only one cost function. By using roughness penalty in the cost function,

we can estimate a smooth field map. We also proposed discretized ML method to select good initial images.

- Water-Fat decomposition from MR k-space data using regularized field map estimation

  The purpose of Chapter 5 is to reconstruct water and fat and field map from MR k-space data. In the method, the cost function includes readout information for considering the data acquisition time. The method can lead to better chemical components estimates than conventional approaches that ignore readout information.

- Model-based image reconstruction for Dual-Energy X-ray CT with Fast kVp switching.

  In Chapter 7, and 8, we present regularized PWLS methods for DE CT reconstruction. The methods reconstruct material density maps directly based from fast kVp switched sinograms without any interpolation. Improved estimated material images lead to more accurate attenuation correction factors for PET.

- Iterative image reconstruction for dual-energy X-ray CT using regularized material sinogram estimates.

  Chapter 10 proposed a dual-energy log-free approach that estimates material sinograms from raw DE CT data directly without any logarithm. (Using a logarithm is sensitive to noise especially when the raw CT data have small values.) We also developed a joint edge-preserving roughness penalty that considers two materials' edge positions jointly.

CHAPTER 2

Estimation Background

Many conventional image reconstruction methods are based on heuristic schemes or ignore the measurement noise. To solve this problem, this thesis uses statistical estimators and we review statistical estimation methods in this chapter.

2.1 Maximum-Likelihood Estimator

Maximum Likelihood (ML) estimation is a popular statistical method used for fitting a statistical model to data. It finds parameter vector x that best matches the data based on the likelihood function $p(y;x)$. The ML estimator using the log-likelihood is defined by

$$\hat{x}_{\mathrm{ML}} = \arg\max_{x \in X} \log p(y;x), \tag{2.1}$$

where X is the set of acceptable values of x.

2.2 Penalized-Likelihood Estimators

Although ML estimation has many desirable properties, the performance of the estimator can be poor for realistic medical image data because medical imaging problems are often ill-conditioned, leading to sensitivity to noise. To improve on the results of ML estimation, other penalty functions are included in Penalized-Likelihood (PL) estimators. A

PL estimator is defined by

$$\Psi(x) = -\log p(y;x) + \beta R(x) \tag{2.2}$$

$$\hat{x} = \arg\min_{x \in X} \Psi(x), \tag{2.3}$$

where Ψ is a cost function that contains a penalty function R and $\beta > 0$ is a penalty parameter controlling the weight of the penalty.

One common penalty function is a roughness penalty such as a quadratic roughness penalty on the difference between neighboring pixels:

$$R(x) = \frac{1}{2} \sum_i \sum_{j \in \mathcal{N}_i} (x_i - x_j)^2, \tag{2.4}$$

where $\mathcal{N}_i$ is a set of neighbor pixels of the ith pixel. This quadratic penalty is simple and easy to minimize but it usually blurs image edges. Another penalty function is edge-preserving roughness penalty that can preserve edges while suppressing noise:

$$R(x) = \frac{1}{2} \sum_i \sum_{j \in \mathcal{N}_i} \psi(x_i - x_j), \tag{2.5}$$

where $\mathcal{N}_j$ denotes the neighborhood of pixel j, $\delta^2 \propto \mathrm{Var}(\rho)$ and ψ is a potential function such as the hyperbola:

$$\psi(\Delta x) = \sqrt{1 + (\frac{\Delta x}{\delta})^2} - 1. \tag{2.6}$$

We can preserve sharp edges while suppressing noise by using this edge-preserving roughness penalty.

2.3 Spatial Resolution Analysis

The need to select the regularization parameter β in the PL estimator is one practical challenge of the PL method. In (2.2), a large value for β would cause a bias because it discourages disparities between neighboring pixel values, whereas when β is small, the

estimated image will be based more on the original data and the image may be rough and noisy. These are conflicting goals, and the regularization parameter controls the trade-off between the two. Fortunately, we can select the parameter β efficiently by analyzing the spatial resolution properties of this problem. Additionally, by spatial resolution analysis, we can achieve more uniform resolution by modifying the penalty function. We focus on PL estimators with cost functions of the form:

$$\hat{x}(y) \triangleq \arg\min_x \psi(y,x), \quad \psi(y,x) = -L(x,y) + \beta R(x), \tag{2.7}$$

where $L(x,y) = \log p(y;x)$ denotes the log-likelihood, $R(x)$ is a roughness penalty function, β is a regularization parameter. The estimator $\hat{x}(y)$ is well defined by the implicit function theorem [63]. After many simplifications, one can show that the gradient of this estimator is [12]:

$$\nabla\hat{x}(y) = [-\nabla^{[2,0]}L(x,y) + \beta\nabla^2 R(x)]^{-1}[\nabla^{[1,1]}L(x,y)]|_{x=\hat{x}(y)}, \tag{2.8}$$

where $\nabla^{[2,0]}L(x,y)$ denotes the Hessian matrix with elements

$$[\nabla^{[2,0]}L(x,y)]_{jk} = \frac{\partial^2}{\partial x_j \partial x_k} L(x,y), \tag{2.9}$$

and $\nabla^{[1,1]}L(x,y)$ denotes the matrix with elements

$$[\nabla^{[1,1]}L(x,y)]_{jk} = \frac{\partial^2}{\partial x_j \partial y_k} L(x,y). \tag{2.10}$$

The local impulse response of an estimator $\hat{x}(y)$ is defined as follows

$$l^j(x) = \lim_{\varepsilon\to 0} \frac{\hat{x}(y + \varepsilon\nabla\bar{y}(x)e_j) - \hat{x}(y)}{\varepsilon} = \nabla\hat{x}(y)\nabla\bar{y}(x)e_j, \tag{2.11}$$

where e_j denotes the jth unit vector and $\bar{y} = \mathsf{E}[y]$. As shown in [15], for PL estimators of the form (2.7), the local impulse response is given by the gradient of the estimator times the gradient of the average data:

$$l^j(x) = [-\nabla^{[2,0]}L(\check{x},\bar{y}(x)) + \beta\nabla^2 R(\check{x})]^{-1}[\nabla^{[1,1]}L(\check{x},\bar{y}(x))]\frac{\partial}{\partial x_j}\bar{y}(x), \tag{2.12}$$

where $\check{x} = \hat{x}(\bar{y}(x))$ is the PL reconstruction from noiseless data. This local impulse response is very useful for investigating the spatial resolution properties estimators in a variety of imaging problems. We use it analysis further in Chapter 9.

CHAPTER 3

MRI Background

Magnetic Resonance Imaging (MRI) is an important tomographic imaging technique that produces images of an object's internal physical and chemical structure. Hydrogen's spin angular momentum is used in conventional MRI. Three external magnetic fields, the main field, a radio-frequency field, and gradient fields, create the signal measured in MRI. Conventionally, this signal is transformed via a Fourier transform to make the final image. For an introduction to MRI, see [44].

3.1 Signal expressions

A time varying voltage in an RF receive coil that is induced by changes in magnetic flux is measured as the signal in MRI. Using Faraday's law of induction, after many simplifications, the received signal, $S_r(t)$, is governed by:

$$s_r(t) = -\int_{\text{vol}} C_1(\mathbf{r}) \cdot \frac{\partial}{\partial t}\mathbf{M}_{XY}(\mathbf{r},t)d\mathbf{r}, \tag{3.1}$$

where $C_1(\mathbf{r})$ denotes the coil's receive sensitivity at spatial position $\mathbf{r}$ and $\mathbf{M}_{XY}$ denotes the transverse magnetization. Further simplifications lead to the following signal equation:

$$\begin{aligned} s(t) &= \int_{\text{vol}} m_0(\mathbf{r}) e^{-i\phi(\mathbf{r},t)} d\mathbf{r} \\ &= \int_x \int_y m_0(x,y) e^{-i2\pi k_x(t)x - i2\pi k_y(t)y} dxdy, \end{aligned} \tag{3.2}$$

where $m_0(x,y)$ is the integral of the magnetization over the slice and the "k-space trajectory" is defined in terms of the user-defined gradient waveforms as follows:

$$k_x(t) = \gamma/2\pi \int_0^t G_x(\tau)d\tau$$
$$k_y(t) = \gamma/2\pi \int_0^t G_y(\tau)d\tau,$$

where G_x denotes the gradient in the x direction, G_y denotes the gradient in the y direction, and γ denotes the gyromagnetic ration that is nuclei dependent. In (3.2), it is seen that there is a Fourier relationship between the MRI signal and the magnetization so each MRI signal value corresponds to a sample of the 2D Fourier transform of the object.

Noise added to the MR signal in (3.1) is modeled as Gaussian, additive noise [39]. Though some noise is produced from the coil, the major noise source is the imaging object. The noise of a typical reconstructed MR image is also Gaussian because the DFT is linear. The Gaussian noise in reconstructed images is white when the kspace samples are uniform on a Cartesian grid, because the DFT is unitary, otherwise it is colored noise.

3.2 Off-Resonance Sources

The resonance frequency is related to the external magnetic field and gyromagnetic ratio. In practice, the resonant frequency will not be uniform because of these two major reasons: (a) the existence of inhomogeneities in the main field, and (b) the chemical shift effect. In this section, we briefly introduce these reasons and in the next chapter, we can correct this inhomogeneity problem by joint estimating the object and field inhomogeneities and we can separate the object into water and fat images by using the chemical shift effect.

3.2.1 Field inhomogeneity

Inhomogeneous magnetic field and differences in the bulk magnetic susceptibility of the object can cause field inhomogeneity in MR imaging. Instead of ignoring the main field inhomogeneity in (3.2), a space variant static field is a more realistic model as follows:

$$\mathbf{B}_0(\mathbf{r}) = (B_0 + \Delta_B(\mathbf{r}))\vec{k}, \tag{3.3}$$

where B_0 is the ideal strength of the main magnetic field, and $\Delta_B(\mathbf{r})$ denotes perturbations of this field. Generalizing (3.2) to consider (3.3) leads to [44] the following more realistic expression for the MR signal:

$$s(t) = \int_{\text{vol}} m_0(\mathbf{r}) e^{-i\phi(\mathbf{r},t)} e^{-i\Delta_\omega(\mathbf{r})t} d\mathbf{r}, \tag{3.4}$$

where $\Delta_\omega(\mathbf{r}) = \gamma\Delta_B(\mathbf{r})$. Therefore, we can correct this undesirable effect by estimating the field map, $\Delta_\omega(\mathbf{r})$.

3.2.2 Chemical shift effect

Each nucleus of a molecule is surrounded by orbiting electrons. These orbiting electrons induce their own local magnetic fields such that the nucleus is partially shielded from the external magnetic field. The fact that nuclei in a spin system are attached to different chemical environments causes the chemical shift [44]. These orbiting electrons perturb the local magnetic field:

$$\mathbf{B}_{\text{eff}}(\mathbf{r}) = \mathbf{B}_0(\mathbf{r})(1 - \sigma(\mathbf{r})), \tag{3.5}$$

where $\sigma(\mathbf{r})$ is the shielding constant. Clearly, the corresponding frequency shift $\Delta\omega$ depends on both the strength of the main field B_0 and the shielding constant σ. The shielding constant, σ, depends on the chemical environment around the nucleus. For example, $\sigma_{fw} \approx 3.5$ppm, where σ_{fw} denotes the chemical shift of ^1H in fat relative to ^1H in water,

i.e.,:

$$\frac{\sigma_w - \sigma_f}{\sigma_w} = 3.5 \cdot 10^{-6}. \tag{3.6}$$

Thus the frequency shift of fat relative to water is:

$$\Delta_\omega = \omega_{fat} - \omega_{water} = -\sigma_{fw}\omega_{water} = -\sigma_{fw}\gamma_{water}B_0, \tag{3.7}$$

where $\gamma_{water} = 42.57\,\mathrm{MHz/T}$. Therefore, fat spins precess about 220 Hz slower than water spins at $B_0 = 1.5\,\mathrm{T}$. By using this chemical shift effect, we can separate water and fat signal in MR imaging.

CHAPTER 4

Water-Fat Decomposition with Regularized Field Map Estimation

This work is based on [29].

4.1 Introduction

We present a novel water-fat decomposition method that uses regularized field map estimation from multiple MR scans with different echo times. We also propose an iterative algorithm to minimize the regularized least-square cost function. Experiments on synthetic data and human knee data suggest that our method improves the water-fat image quality and accuracy of the estimated field map.

4.2 Multi Scan Field Map Estimation

4.2.1 Reconstructed Image Model

The input data is L reconstructed images with different echo times, denoted by $\underline{\mathbf{y}} = (\mathbf{y}^1, \mathbf{y}^2, \ldots, \mathbf{y}^L)$, where typically $L = 3$ and each image has N voxels. Let ω_j denote the unknown resonant frequency offset of spins within the jth voxel, and $-\mathrm{R}_j^{\mathrm{W}}$ and $-\mathrm{R}_j^{\mathrm{F}}$ denote the R_2^*, the relaxation rates, of water and fat respectively within that voxel. At 1.5T, the frequency shift of fat relative to water, Δf, is about -220 (Hz) caused by chemical shift. We

model the L images by

$$\mathrm{y}_j^l = (\mathrm{W}_j e^{-\mathrm{R}_j^{\mathrm{W}} t_l} + \mathrm{F}_j e^{-\mathrm{R}_j^{\mathrm{F}} t_l} e^{i2\pi(\Delta \mathrm{f})t_l}) e^{i\omega_j t_l} + \varepsilon_j^l, \tag{4.1}$$

for l $= 1, 2, ...,$ L and j $= 1, 2, ...,$ N, where t_l denotes the echo time difference of the lth scan relative to the the first scan, W_j and F_j denote the unknown water and fat components in the jth voxel, respectively, and ε_j^l denotes the complex noise. The goal here is to jointly estimate the field map $\omega = (\omega_1, \omega_2, \ldots, \omega_N)$, the water components $\mathbf{W} = (\mathrm{W}_1, \mathrm{W}_2, \ldots, \mathrm{W}_N)$, and fat components $\mathbf{F} = (\mathrm{F}_1, \mathrm{F}_2, \ldots, \mathrm{F}_N)$ from the images $\underline{\mathbf{y}}$. Because $-\mathrm{R}_j^{\mathrm{W}}$ and $-\mathrm{R}_j^{\mathrm{F}}$ are small relative to the echo time reciprocals, we assume $e^{-\mathrm{R}_j^{\mathrm{W}} t_l} \simeq 1$ and $e^{-\mathrm{R}_j^{\mathrm{F}} t_1} \simeq 1$ for all j and l, although the method could be generalized.

4.2.2 ML Field Map Estimation

We assume that ε_j^l in (4.1), the additive complex noise, are independent and identically distributed Gaussian random variables with mean 0 and variance σ^2. Under this assumption, the joint log likelihood for ω, $\mathbf{W}$, and $\mathbf{F}$ given $\mathbf{y}$ is

$$\begin{aligned} &\sum_{l=1}^{L} \log \mathrm{p}(\mathbf{y}^l; \omega, \mathbf{W}, \mathbf{F}) \\ &\equiv \frac{-1}{2\sigma^2} \sum_{l=1}^{L} \sum_{j=1}^{N} |\mathrm{y}_j^l - (\mathrm{W}_j + \mathrm{F}_j e^{-i2\pi(-\Delta \mathrm{f})t_l}) e^{i\omega_j t_l}|^2, \end{aligned} \tag{4.2}$$

where " $\equiv''$ denotes equivalence to within irrelevant constants. Rewriting in matrix-vector form, we can determine the maximum likelihood (ML) estimate of ω, $\mathbf{W}$, and $\mathbf{F}$ by solving the following minimization problem:

$$\underset{\omega \in \mathbb{R}^N \mathbf{W}, \mathbf{F} \in \mathbb{C}^N}{\arg\min} \sum_{j=1}^{N} \left\| \underline{\mathrm{y}}_j - D(\omega_j) A \mathrm{X}_j \right\|^2, \tag{4.3}$$

where $D(\omega_j) = \text{diag}(e^{i\omega_j \underline{t}})$, $e^{i\omega_j \underline{t}} = \begin{bmatrix} e^{i\omega_j t_1} \\ e^{i\omega_j t_2} \\ \vdots \\ e^{i\omega_j t_L} \end{bmatrix}$, $A = \begin{bmatrix} 1 & e^{-i2\pi(-\Delta f)t_1} \\ 1 & e^{-i2\pi(-\Delta f)t_2} \\ \vdots & \vdots \\ 1 & e^{-i2\pi(-\Delta f)t_L} \end{bmatrix}$, and $\mathrm{X}_j = \begin{bmatrix} \mathrm{W}_j \\ \mathrm{F}_j \end{bmatrix}$. Because (4.3) is quadratic in X_j, we can find the ML estimate of X_j, the water and fat components in terms of ω analytically as follows:

$$\hat{\mathrm{X}}_j(\omega_j) = [A^H A]^{-1} A^H D^H(\omega_j) \underline{\mathrm{y}}_j. \tag{4.4}$$

Substituting $\hat{\mathrm{X}}_j(\omega_j)$ into (4.3) leads to the following cost function for ML estimation of the field map ω :

$$\begin{aligned} \hat{\omega} &= \underset{\omega \in \mathbb{R}^N}{\arg\min}\, \Psi_{\mathrm{ML}}(\omega) \\ \Psi_{\mathrm{ML}}(\omega) &= \sum_{j=1}^{N} \left\| \underline{\mathrm{y}}_j - D(\omega_j) A \hat{\mathrm{X}}_j(\omega_j) \right\|^2. \end{aligned} \tag{4.5}$$

After solving this nonlinear minimization problem, we substitute $\hat{\omega}$ into (4.4) to determine the ML estimates of the water W_j and fat F_j components. We simplify (4.5) as follows:

$$\begin{aligned}
\Psi_{\mathrm{ML}}(\omega) &= \sum_{j=1}^{N} -\underline{\mathrm{y}}_j^H D(\omega_j) A [A^H A]^{-1} A^H D^H(\omega_j) \underline{\mathrm{y}}_j \\
&= \sum_{j=1}^{N} -\left\| B^H D(\omega_j) \underline{\mathrm{y}}_j \right\|^2 \\
&= \sum_{j=1}^{N} -\left\| V_j e^{-i\omega_j \underline{t}} \right\|^2 \\
&= \sum_{j=1}^{N} \sum_{l=1}^{L} \sum_{m=1}^{L} -\mathrm{C}_{j,l,m} e^{i\omega_j (t_l - t_m)} \\
&= \sum_{j=1}^{N} \sum_{l=1}^{L} \sum_{m=1}^{L} -\mathrm{real}(\mathrm{C}_{j,l,m} e^{i\omega_j (t_l - t_m)}) \\
&= \sum_{j=1}^{N} \sum_{l=1}^{L} \sum_{m=1}^{L} -|\mathrm{C}_{j,l,m}| \cdot \cos(\angle \mathrm{C}_{j,l,m} + \omega_j (t_l - t_m), \qquad (4.6)
\end{aligned}$$

where we define B such that $BB^H = A(A^H A)^{-1} A^H$, $\mathrm{V}_j \triangleq B^H D(\underline{\mathrm{y}}_j)$, $\mathrm{C}_{j,l,m} \triangleq \mathrm{V}_{j,1,m} \mathrm{V}^*_{j,1,l} + \mathrm{V}_{j,2,m} \mathrm{V}^*_{j,2,l}$. Since $\mathrm{C}^*_{j,m,l} = \mathrm{C}_{j,l,m}$, the ML cost function in (4.6) is equivalent to

$$\begin{aligned}
\Psi_{\mathrm{ML}}(\omega) \equiv \sum_{j=1}^{N} \sum_{l=1}^{L} \sum_{m=1}^{L} |\mathrm{C}_{j,l,m}| \cdot \\
[1 - \cos(\angle \mathrm{C}_{j,l,m} + \omega_j (t_l - t_m))]. \qquad (4.7)
\end{aligned}$$

Note that this ML cost function is similar to the cost function used in phase unwrapping problems, *e.g.*, [38] and [17], when $L = 0$ and $\mathrm{R}^*_2 = 0$. We will show that the ML estimate $\hat{\omega}$ is very noisy, but we include it for completeness.

4.2.3 Discretized ML Method

We can estimate the field map, $\tilde{\omega} = [\tilde{\omega}_1, \tilde{\omega}_2, ..., \tilde{\omega}_N]$, by minimizing (4.6) separately for each voxel. We implement the ML method numerically using a discretized search as follows:

$$\tilde{\omega}_j = \underset{\omega_j \in \mathbb{S}}{\arg\min} -\left\| B^H D(\omega_j) \underline{\mathrm{y}}_j \right\|^2, \qquad (4.8)$$

where $\mathbb{S} = \{|\Delta f/2| \times \frac{k}{n} : n = 55, k = -n, -(n-1), \ldots, n\}$. Note that $|\omega_j|$ is usually less than $|\Delta f/2|$ [57] and $|\Delta f/2|$ is about 110 (Hz) at 1.5T. We search $\tilde{\omega}_j$ using discrete steps from $-|\Delta f/2|$ to $|\Delta f/2|$ in 2 (Hz) increments. Therefore, this Discretized ML estimate is reasonable because when we consider the effect of the complex noise, a 2 (Hz) step size is small enough. This method has low computation complexity because it does not use an iterative algorithm.

4.2.4 PL Field Map Estimation

Finding the ML estimates of ω, W, and F as in [52] and [65], and (4.8) ignores the important prior knowledge that field maps are usually spatially smooth. The field maps of these methods are estimated independently on a voxel-by-voxel basis, using an overly simplified ML method. Specifically, these methods separate field map estimation from smoothing and final water-fat separation. Instead of low pass filtering or 2-D extrapolation, we propose a Regularized method that jointly estimates W, F, and ω, by using a PL approach, where we include a spatial roughness penalty $R(\omega)$ in the cost function as follows:

$$(\hat{\omega}, \hat{\mathbf{W}}, \hat{\mathbf{F}}) = \underset{\omega \in \mathbb{R}^N \mathbf{W}, \mathbf{F} \in \mathbb{C}^N}{\arg\min} \sum_{l=1}^{L} -\log \mathrm{p}(\mathbf{y}^l; \mathbf{W}, \mathbf{F}, \omega) + \beta R(\omega). \tag{4.9}$$

We regularize the field map, ω, only and not **W** or **F** because water and fat components are expected to be much more rough and complicated due to anatomical details. Minimizing over **W** and **F** again yields the solution (4.4). Substituting into (4.9) yields the PL cost function:

$$\Psi_{\mathrm{PL}}(\omega) \triangleq \Psi_{\mathrm{ML}}(\omega) + \beta R(\omega) = \sum_{j=1}^{N} \sum_{l=1}^{L} \sum_{m=1}^{L} |\mathrm{C}_{j,l,m}| \cdot$$

$$[1 - \cos(\angle \mathrm{C}_{j,l,m} + \omega_j (t_l - t_m))] + \beta R(\omega). \tag{4.10}$$

Note that

$$\sum_{l=1}^{L}\sum_{m=1}^{L}|\mathrm{C}_{j,l,m}| \propto \|\underline{\mathrm{y}}_j\|^2. \tag{4.11}$$

Therefore, the cost function in (4.10) gives less weight to any voxels where $\|\underline{\mathrm{y}}_j\|^2$ is small. These voxels have less valuable information because small $\|\underline{\mathrm{y}}_j\|^2$ means that such voxels have low SNRs. Thus, the regularization term, $\beta R(\omega)$, will extrapolate the field map estimation within them based on high SNR neighboring values.

When ω is an $N_1 \times N_2$ field map, the regularizing roughness penalty uses 2nd-order differences between horizontal, vertical, and diagonal neighboring voxel values as follows:

$$R(\omega) = \sum_n \sum_m (\psi(R_{10}[n,m]) + \psi(R_{-1-1}[n,m]) + \psi(R_{01}[n,m]) + \psi(R_{-11}[n,m])), \tag{4.12}$$

where $R_{kl}[n,m] = 2\cdot\omega[n,m] - \omega[n-k,m-l] - \omega[n+k,m+l]$, and ψ is a convex and differentiable function. Usually, $\dot{\psi}(t)/t$ is bounded by unity such as $\psi(t) = t^2/2$ which we assume hereafter. To perform minimization in (4.9), we use optimization transfer. The second derivative of $1-\cos(t)$ is bounded by unity. Thus, one can show that the following iteration monotonically decreases and converges to a local minimizer of $\Psi(\omega)$ based on [30]:

$$\omega^{(n+1)} = \omega^{(n)} - \mathrm{diag}\left\{\frac{1}{d_j + \beta\cdot c}\right\}\nabla\Psi(\omega^{(n)}),$$

where

$$c \triangleq \begin{cases} 4, & \text{regularization with 1st-order differences} \\ 16, & \text{regularization with 2nd-order differences,} \end{cases} \tag{4.13}$$

and where

$$d_j \triangleq \sum_{l=1}^{L}\sum_{m=1}^{L}|\mathrm{C}_{j,l,m}|(t_l - t_m)^2. \tag{4.14}$$

The initializer $\omega^{(0)}$ will be described in §4.2.6. We repeat this iterative algorithm until the root mean square change between each iteration is less than 0.5(Hz).

4.2.5 PWLS field map estimation method

Since usually time delays, t_l for $l = 1, 2, ..., L$, are chosen to avoid phase wrapping as much as possible [51], the $1 - \cos$ terms can be simplified with its second-order Taylor series: $1 - \cos \approx t^2/2$. In such cases, especially when $|\omega_j|$ is less than $|\Delta f/2|$, we can consider the cost function is a locally convex and smooth function of ω_j. An alternative to (4.12) is to estimate the field map $\hat{\omega}_{PWLS}$ as follows:

$$\hat{\omega}_{\mathrm{PWLS}} = \underset{\omega \in \mathbb{R}^N}{\arg\min} \sum_{j=1}^{N} \mathrm{g}_j (\omega_j - \tilde{\omega}_j)^2 + \alpha R(\omega), \tag{4.15}$$

where $\alpha \in \mathbb{R}$ and g_j is a weighting function. Empirically, we found that choosing α such that $\log_2 \alpha = \mathrm{median}(g_j)$ generated the best results over various SNR values. We define a weighting function, g_j, as follows:

$$\mathrm{g}_j \triangleq \|\underline{\mathrm{y}}_j\|^2. \tag{4.16}$$

As discussed above, voxels with low signal magnitude cause "outlier" problems. We shall call voxels with small $\|\underline{\mathrm{y}}_j\|^2$ as 'bad' voxels. We define the set of 'bad' voxels as follows:

$$\mathrm{J} = \{j : \min(\|\underline{\mathrm{y}}_j\|^2, \mathrm{m}_j) < \gamma \cdot \mathrm{M}\}, \tag{4.17}$$

where $\mathrm{M} = \max \|\underline{\mathrm{y}}_j\|^2$, $\mathrm{m}_j = \frac{1}{8} \sum_{k \in \mathrm{N}_j} \|\underline{\mathrm{y}}_j\|^2$, N_j denotes the set of the 8 nearest neighbors of voxel j and we set the threshold γ to include only voxels with only sufficiently small magnitude, *e.g.*, $\gamma = 0.5$.

To reduce 'bad' voxels' effect and to simplify processing, we put different weights on each voxel:

$$\mathrm{g}_j \triangleq \begin{cases} 0, & j \in \mathrm{J} \\ \|\underline{\mathrm{y}}_j\|^2, & \text{otherwise.} \end{cases} \tag{4.18}$$

The PWLS method has an important limitation caused by ignoring any phase wrap that may occur when evaluating a field map. However, as we discussed before, time delays are chosen to avoid phase wrap and we provide this method with a reasonable initial guess, the estimated field map of the discretized ML method $\tilde{\omega}$. Thus, for our initial field map of the PL method, this regularized version of $\hat{\omega}_{\text{PWLS}}$ is better than other initial guesses.

4.2.6 Initialization

Selecting a good initial field map is very important for the PL method. This is because the result of the above iterative algorithm (4.13) converges to a local minimizer of $\Psi(\omega)$ that lies within the "basin" containing the initial estimate [30]. Some conventional field map initialization methods are zero [52], using the output of the Pixel Independent method [65], and using the phase angle of the source images [17].

Using the zero initial guess or the output of Pixel Independent method easily leads to the phase "outlier" problem. The Region Growing method is not preferable because it is computationally very intensive. Initial field map based on the angle of $\mathbf{y}$ or matrix C in (4.6), however, results in larger than $\Delta f/2(\text{Hz})$ field map in some voxels. This is contrary to the fact that the magnitude of the field map in each voxel is usually less than $|\Delta f/2|$ [57]. Thus, we propose and investigate the Discretized ML method and the PWLS method to choose the initial field map, $\omega^{(0)}$.

First, the source images (512×512) are down sampled to a low resolution image (64×64). Next, the Discretized ML method is performed on the low resolution source image. As shown in §4.2.3, the generated low resolution field map, $\tilde{\omega}$, will not be smooth enough. This is because, as discussed in §4.2.3, each voxel in the field map is estimated independently. Thus, we need to spatially low-pass filter the estimated field map. However, the field map can be corrupted by some outlier values when we use a conventional

low-pass filter (*e.g.*, a gaussian low-pass filter). Therefore, to obtain a refined field map, we use the PWLS method for smoothing. Next, PL method is implemented using this refined estimated field map, ω_{PWLS}, as its initial guess. Finally, the estimated field map of PL method is up sampled (512×512). This final estimated field map is used as our initial field map, $\omega^{(0)}$, of PL method.

The down sampling factor, 8, was selected empirically. The optimal down sampling factor depends on the complexity of the true field map. For example, the more complex field map the smaller the down sampling factor. However, the down sampling factor 8 worked well generally.

4.2.7 Spatial Resolution Analysis for selecting β

The need to select the regularization parameter β in the penalized-likelihood estimator (4.13) is one limitation of the PL method. Fortunately, we can select the parameter β efficiently by analyzing the spatial resolution properties of this problem. By using the methods in [15], the local frequency response of the Regularized field map estimator at the jth voxel is

$$\mathrm{H}(\omega_{\mathrm{x}}, \omega_{\mathrm{y}}) \approx \frac{1}{1 + \frac{\beta}{d_j}({\omega_{\mathrm{x}}}^2 + {\omega_{\mathrm{y}}}^2)^p}, \tag{4.19}$$

where ω_{x} and ω_{y} are frequency variables in the Discrete Space fourier transform and

$$p = \begin{cases} 1, & \text{regularization with 1st-order differences} \\ 2, & \text{regularization with 2nd-order differences.} \end{cases} \tag{4.20}$$

The local frequency response (4.19) depends on the value of d_j and β.

From (4.11) and (4.14),

$$d_j = \sum_{l=1}^{L} \sum_{m=1}^{L} |\mathrm{C}_{j,l,m}|(t_l - t_m)^2 \propto \|\underline{\mathrm{y}}_j\|^2. \tag{4.21}$$

Therefore, in a voxel with small $\|\underline{y}_j\|^2$ there will be more smoothing and in the voxel with large $\|\underline{y}_j\|^2$ there will be less smoothing as we would expect. Normalizing the data values $\underline{y}_j$ by the square root of the median of the $\|\underline{y}_j\|^2$ results in typical values of $\|\underline{y}_j\|^2$ equal to unity. This factor has the effect of producing the same β to FWHM relationship based on [17]. After normalizing the source images, the FWHM depends only on β and increases monotonically with β as we desire. Thus, when we normalize the image magnitudes in regularized methods, the best value of β depends on the SNR. We need a high value of β for low SNR data to make the estimated field map smoother. However, with high SNR, a large value for β would cause a large bias because it would make the field map too smooth. If β is too small, the field map is not smooth enough. Empirically, we found that the following value of $\log_2 \beta$ worked well:

$$\log_2 \beta = \begin{cases} \dfrac{(18 - \mathrm{SNR})}{5}, & \text{for original images} \\ \dfrac{(-1.5 - \mathrm{SNR})}{7}, & \text{for low resolution images.} \end{cases} \tag{4.22}$$

4.3 Results

We applied the proposed method to a real MRI scan of a human knee and to a simulated data set. The real data was acquired at 1.5T with the IDEAL method (phase shifts = $-\pi/6, \pi/2, 7\pi/6$; time shifts = -0.4 ms, 1.2 ms, and 2.8 ms) and the simulated data were constructed with the same echo times [51].

Fig. 4.1 shows the simulated field map, the simulated water image the simulated fat image, and the three IDEAL source images, y_j^l for $l = 1, 2, 3$. (Each image is 512×512). We choose our simulated field map as a 2-d Gaussian image because a real field map usually is smooth. We designed the simulated water and fat images to be somewhat similar to a human knee. These images contain all levels of water-fat ratios to simulate all possible situations of the real data. The source images were made by following the formula in (4.1)

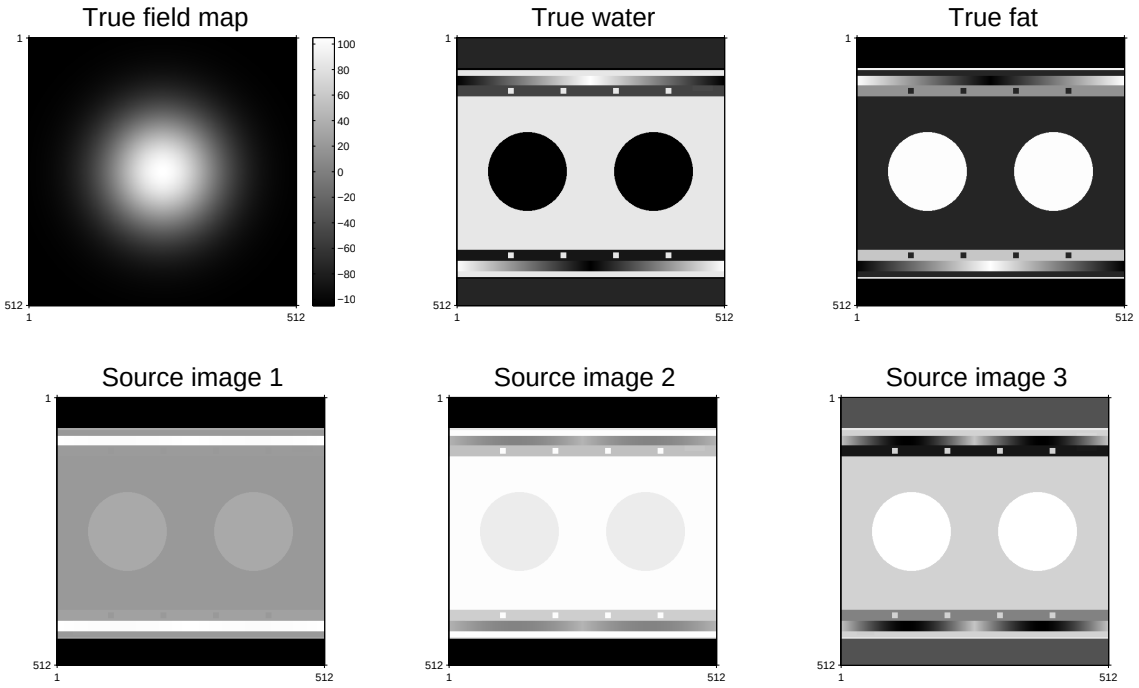

Fig. 4.1: Top row: the simulated field map, water image, fat image. Bottom row: the simulated source data at 1.5 T. (phase shifts = $-\pi/6, \pi/2, 7\pi/6$)

with these simulated field map, water image, and fat image. We added complex white Gaussian noise at many levels of SNR to these source images. In this paper, we used the following definition of SNR:

$$\text{SNR} = 20\log\frac{\|E[y]\|}{\|y - E[y]\|}, \tag{4.23}$$

where $E[y]$ is the original image and $y - E[y]$ is the noise.

Fig. 4.2 illustrates field map, water image, and fat image of the Pixel independent method and the corresponding images of the Region Growing method and PL method (SNR = 15dB). As shown in the first row in Fig. 4.2, the result of Pixel Independent method has several voxels which have outlier values. However, the PL method and the Region Growing method succeeded to reduce these outliers. It is very hard to distinguish the differences between the Region Growing method and the PL method. However, compared to the Region Growing method, the PL method yielded a more smooth field map image.

We shall quantify the error of estimated images by computing the root mean square error (RMSE) of the estimated field map and the normalized root mean square error (NRMSE) of the estimated water and fat images. We defined the RMS error (in Hz) and the NRMS error as follow:

$$\mathrm{RMSE}(\hat{\omega}) = \sqrt{\frac{1}{N}\|\omega - \hat{\omega}\|^2}$$
$$\mathrm{NRMSE}(\hat{\mathrm{W}}) = \frac{\|\hat{\mathrm{W}} - \mathrm{W}\|}{\|\mathrm{W}\|} 100\%,$$

where ω denotes the simulated field map, $\hat{\omega}$ denotes a estimated field map, and where W is the water component and $\hat{\mathrm{W}}$ is a estimated water component. The NRMSE of fat is defined similarly.

Fig. 4.3(a) displays the RMSE of the field map estimates produced the Pixel Independent method, Region Growing method, and the PL method. The RMSE of the Pixel independent method is much higher than other methods for all levels of SNR. Because of outlier voxels, the RMSE was not sufficiently low for high SNR. On the other hand, due to reasonable initial values, the Region Growing method reduced the RMSE for high SNR. However, many outlier voxels still existed especially at the boundary between water and fat region. The RMSE of the PL method was lower than the Region Growing method for all levels of SNR. Especially for low SNR levels, the PL method dramatically reduced the RMSE. For example, when SNR is 3dB, the RMSE of the PL method is 3.01 while the RMSE of Region Growing is 17.44.

The improvement in NRMSE of the PL method over other methods is shown in Fig. 4.3(b) and (c). Similarly, we observed reduced RMSE values for all SNR levels. It is difficult to distinguish the differences between the NRMSE of the PL method and the Region Growing method. However, the NRMSE of the PL method was still smaller than the NRMSE of the Region Growing method.

In Fig. 4.4, the processes of initialization are illustrated on simulated data and real data. The outputs of the Discretized ML method on the low resolution source images, shown in Fig. 4.4(a) and (e). Because these images were estimated pixel-by-pixel without any roughness penalty function or low-pass filter, they are rough images. These estimated field maps are filtered by using the PWLS method. Fig. 4.4(b) and (f) show refined field maps, the outputs of the PWLS method. We can regularize it without corrupting even though it contain several outlier voxels. The PL method is performed using these regularized field maps as our initial guess, shown in Fig. 4.4(c) and (g). Figs. 4(d) and (h) show the final initial field maps, the up sampled estimated field maps of PL method, for simulated data and real data respectively.

Fig. 4.5(a)-(c) compare the estimated field maps produced by the three methods. The estimated field map of the PL method, shown in Fig. 4.5(c), is the smoothest, especially in the background areas. Water and fat images of three methods are shown in Fig. 4.5(d)-(i). Though the differences between estimated field maps are substantial, the differences between the resulting fat and water images are subtle. However, the plot of the NRMSE of water and fat images shown in Fig. 4.3, suggests that the images from the PL Method are slightly improved. After this work was completed, we learned of the work of [21] that was developed independently.

4.4 Conclusion

We proposed a method for water-fat decomposition in MRI with regularized field map estimation. The experiments show that the proposed PL method can lead to smoother field map estimates than the Region Growing method [65] as seen Fig. 4.5(b) and (c). Simulation results showed that the PL method yields images with lower RMS errors than the Region Growing method. Another potential advantage of our technique is that it can

avoid the well known problem of water-fat swapping in voxels that contain just fat or water. To avoid such behavior, field map smoothness is used in the previous heuristic Region Growing approach [65]. In the presented approach, incorporating roughness penalty into reconstruction may solve this problem automatically.

4.5 Acknowledgement

We thank Prof. Samsonov Alexey for collecting the realistic MRI data used in this chapter.

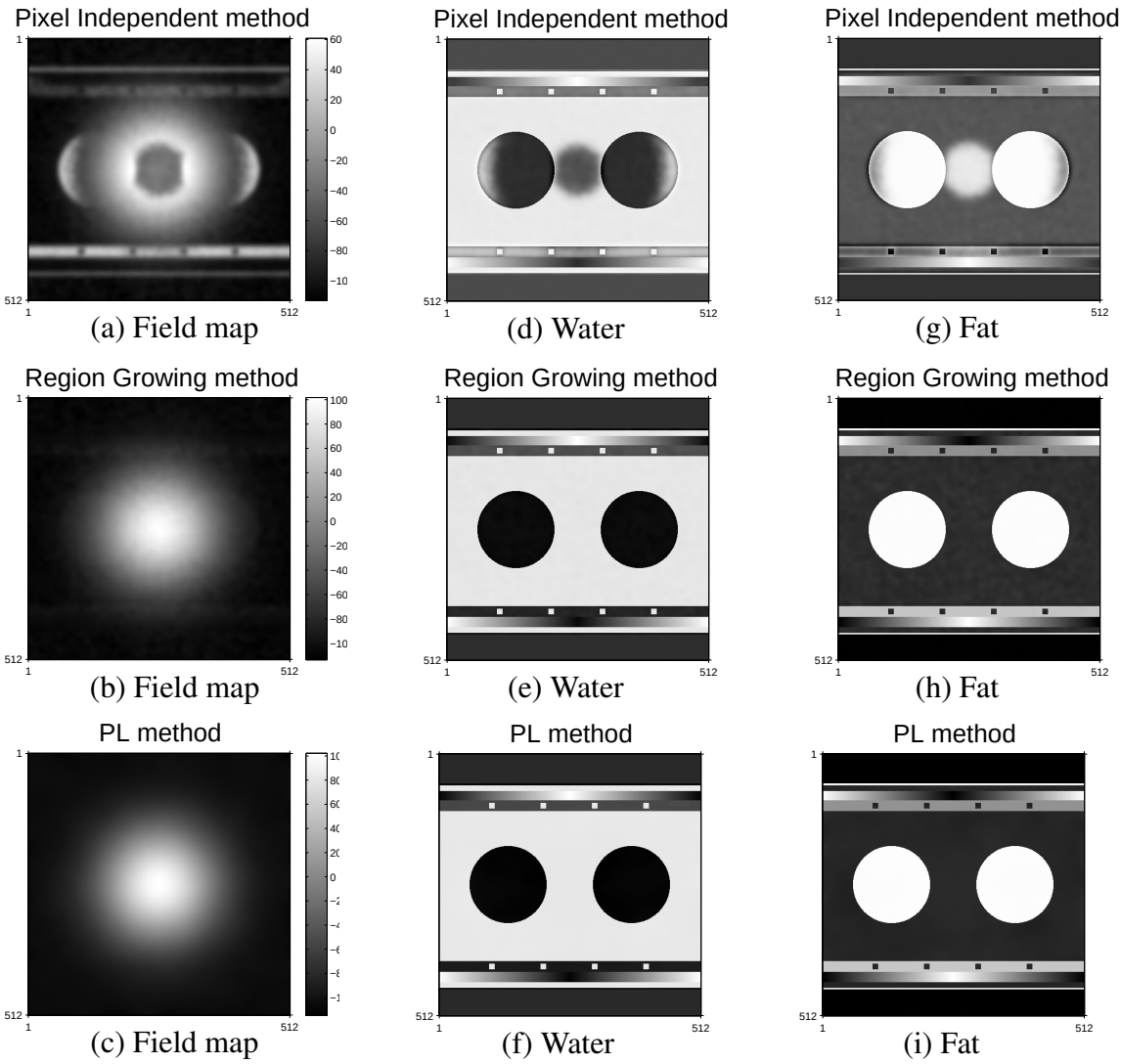

Fig. 4.2: First column: estimated field maps of three methods. Second column: estimated water images of three methods. Third column: estimated fat images of three methods. SNR = 15dB.

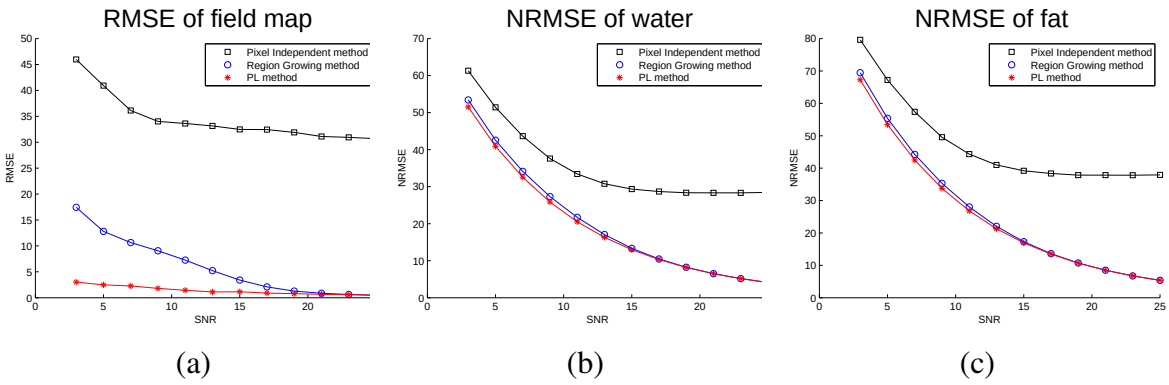

Fig. 4.3: Improvement of the PL method in the RMSE and NRMSE.

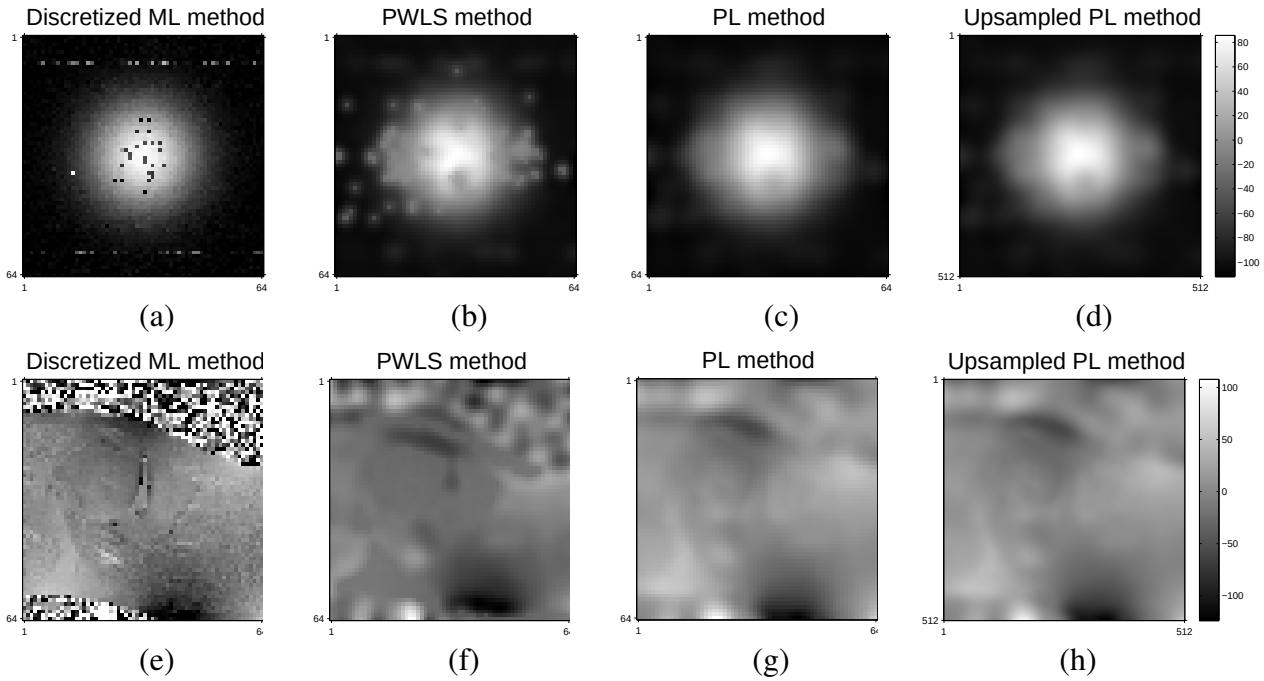

Fig. 4.4: Top row: Initialization on simulated data. Bottom row: Initialization on real data.

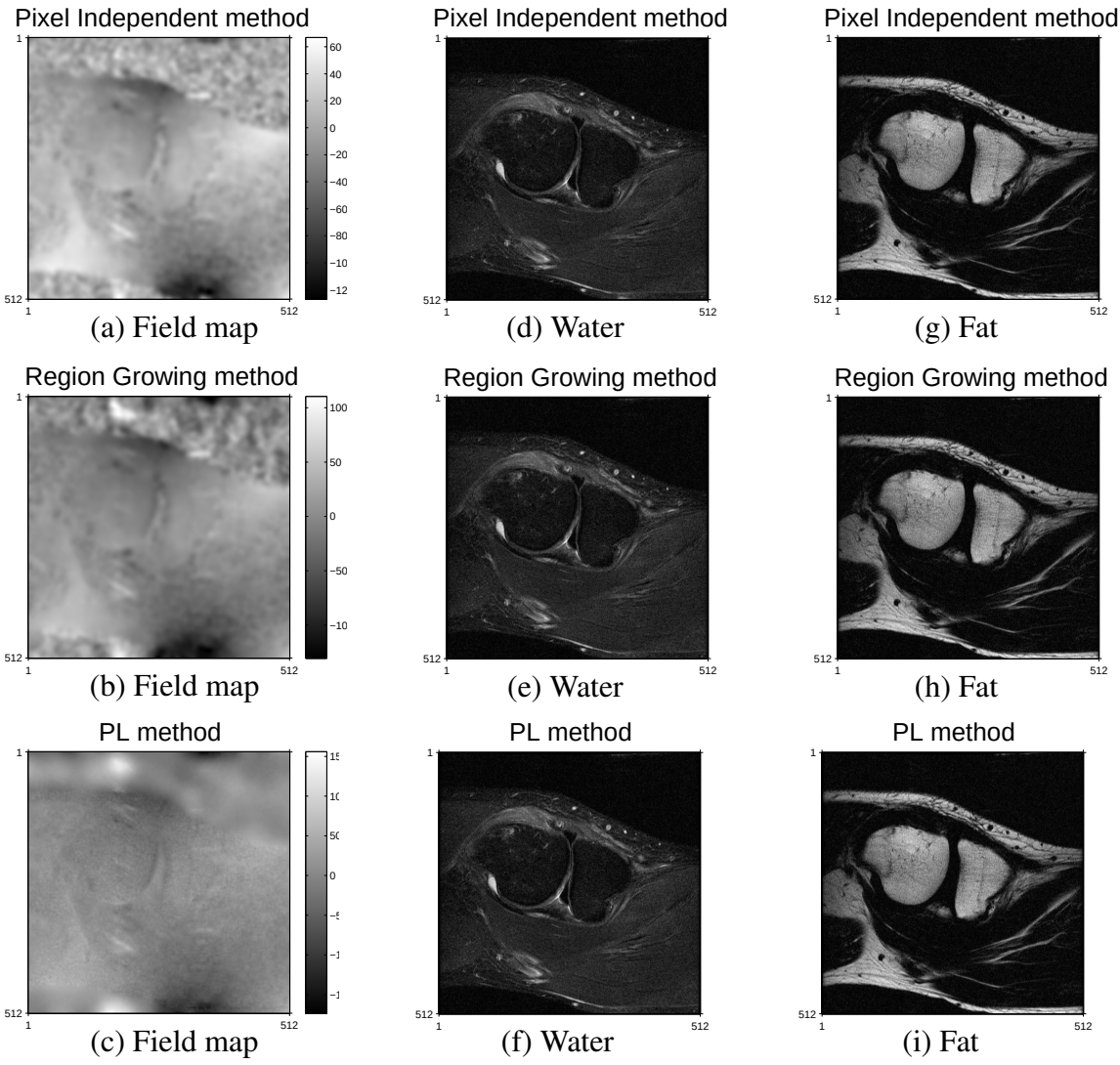

(a) Field map (d) Water (g) Fat

(b) Field map (e) Water (h) Fat

(c) Field map (f) Water (i) Fat

Fig. 4.5: First column: estimated field maps of three methods. Second column: estimated water images of three methods. Third column: estimated fat images of three methods.

CHAPTER 5

Water-Fat Decomposition from MR k-space Data using Regularized Field Map

This work is based on [26].

5.1 Introduction

The ability of MRI to separate chemical components, using methods such as IDEAL, Region Growing, and linear prediction (LP) [21,51,65], is important in clinical use. However, conventional approaches can be sensitive to field inhomogeneity. In Chapter 4, we proposed a PL method that yields smoother estimated field maps with lower RMS errors than the Region Growing method by using a regularizing roughness penalty. However, like other conventional approaches, our PL method also ignores any temporal changes during the readout in its model which may limit the accuracy of the PL method. This chapter describes a new regularized iterative algorithm, termed k-space method, that reconstructs water and fat and field map from MR k-space data. The k-space method considers phase evolution due to field inhomogeneity and chemical shift during MR data acquisition. In the method, the cost function includes a regularized term that exploits our prior knowledge that field maps are usually smooth. We use an iterative approach to jointly estimate the field map, water, and fat components. By modeling readout information in the cost function, the method yields improved estimates of the chemical components.

5.2 K-space method

The input data consists of L MR k-space data sets with different echo times τ_l, denoted by $y = (y^1, y^2, ..., y^L)$, where typically $L = 3$. Let Δm denote the chemical shift of the mth chemical component relative to water (Hz) and let ω_n denote the off-resonance of the nth voxel. We model the MR k-space data by including the data readout time, t_s, as follows:

$$y_s^l = \phi(\vec{k}(t_s)) \sum_n \sum_m (X_{nm} e^{-j2\Delta_m(t_s+\tau_l)} e^{-j\omega_n(t_s+\tau_l)} e^{-j2\pi(\vec{k}(t_s)\cdot\vec{r}_n)}) + \varepsilon_s^l,$$

for $l = 1, 2, ..L$, and $s = 1, 2, ..S$, where $\phi(\vec{k}(t_s))$ denotes the Fourier transform of the voxel basis function, τ_l denotes the echo time difference of the lth scan relative to the original scan, X_{nm} denotes the unknown amount of the mth chemical component in the nth voxel, and ε_s^l denotes the additive complex noise. We assume that the noise values, ε_s^l, are zero-mean independent white complex Gaussian. The goal here is to estimate the chemical components $\underline{X} = (X_{11}, X_{12}, ..., X_{NM})$ and the field map $\omega = (\omega_1, \omega_2, ..., \omega_N)$ from the MR data $\underline{y}$.

We propose an iterative method where we minimize the following function:

$$\begin{aligned}(\hat{\underline{X}}, \hat{\omega}) &= \arg \min_{\underline{X} \in \mathbb{C}^{N \cdot M}, \hat{\omega} \in \mathbb{R}^N} \Psi_{PL}(\underline{X}, \omega) \\ &= \arg \min_{\underline{X} \in \mathbb{C}^{N \cdot M}, \hat{\omega} \in \mathbb{R}^N} \sum_{l=1}^{L} \left\| \underline{y}^l - A^l(\omega) B^l \underline{X} \right\|^2 + \beta_1 \mathrm{R}(\underline{X}) + \beta_2 \mathrm{R}(\omega), \end{aligned} \tag{5.1}$$

where $[A^l(\omega)]_{s,n} = \phi(\vec{k}(t_s)) e^{-j\omega_n(t_s+\tau_l)} e^{-j2\pi(\vec{k}(t_s)\cdot\vec{r}_n)}$, $[B^l] = \mathrm{diag}(D_1^l, D_2^l, ..., D_N^l)$, $D_k^l = e^{-j\underline{\Delta}\tau_l}$ for all k, and $\underline{\Delta} = [\Delta_1, \Delta_2, ..., \Delta_M]$. Although the correct model would use $e^{-j2\Delta_m(t_s+\tau_l)}$, we used $e^{-j2\Delta_m\tau_l}$ in this study. To estimate the M chemical component maps, we repeatedly alternate between two major steps: updating the chemical component estimates and updating the field map estimates. First, we estimate chemical components based on the estimated field map in the previous iteration by minimizing the following penalized

least-squares (PL) cost function with respect to X:

$$\begin{aligned}\underline{\hat{X}}^{(i)} &= \arg\min_{\underline{X}\in\mathbb{C}^{N\cdot M}} \Psi^1_{PL}(\underline{X};\hat{\omega}^{(i-1)}) \\ &= \arg\min_{\underline{X}\in\mathbb{C}^{N\cdot M}} \sum_{l=1}^{L} \left\| \underline{y}^l - A^l(\hat{\omega}^{(i-1)})B^l\underline{X} \right\|^2 + \beta_1 \mathrm{R}(\underline{X}),\end{aligned} \tag{5.2}$$

Second we estimate the field map based on the estimated chemical components in the previous iteration as follows:

$$\begin{aligned}\hat{\omega}^{(i)} &= \arg\min_{\omega\in\mathbb{R}^N} \Psi^2_{PL}(\omega;\underline{\hat{X}}^{(i-1)}) \\ &= \arg\min_{\omega\in\mathbb{R}^N} \sum_{l=1}^{L} \left\| \underline{y}^l - A^l(\omega)B^l\underline{\hat{X}}^{(i-1)} \right\|^2 + \beta_2 \mathrm{R}(\omega).\end{aligned} \tag{5.3}$$

We solve this step using a similar approach to [47]. We denote i as the iteration index, $\underline{\hat{X}}^{(i)}$ and $\hat{\omega}^{(i)}$ as the estimated chemical component and the field map in the ith iteration. The regularizing roughness penalty uses differences between horizontal and vertical neighboring voxel values. Our algorithm repeatedly minimizes (5.2) and (5.3) until the changes in the estimated value of chemical components and field map are less than a stopping criteria. To minimize (5.2) and (5.3), we use an optimization transfer iteration that decreases the cost function monotonically. Thus the estimated chemical components and field map converge to a local minimizer of the PL cost function (5.1). To encourage the iteration to converge to a desirable local minimum, we choose the estimated field map in [22] as our initial field map, $\hat{\omega}^{(0)}$, for the iteration.

5.3 Results

We applied the k-space method to a simulated data set. The simulated data were generated with the IDEAL method (B0 = 1.5T; phase shifts = $-\pi/6, \pi/2, 7\pi/6$; time shifts = -0.4ms, 1.2ms, and 2.8ms).

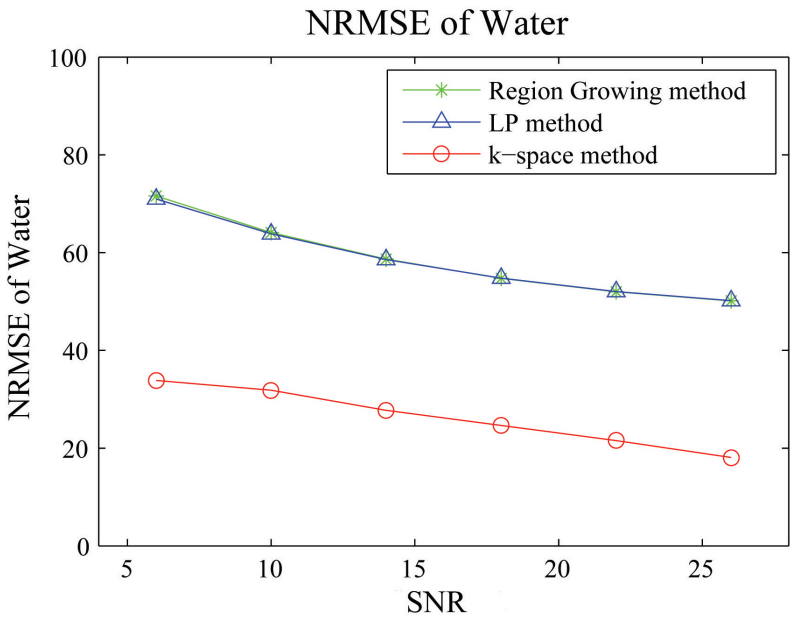

Fig. 5.1: Improvement of the k-space method in the NRMSE of water estimates

Fig. 5.1 and Fig. 5.2 show the improvement in NRMSE using the k-space method over Region Growing method and LP method [22]. The NRMSE of the k-space method was lower than the other methods for all levels of SNR.

Fig. 5.3 shows the simulated images and the estimated water and fat images of the k-space method and other methods when SNR = 20.

Fig. 5.4 shows the error of estimated water and fat images of three methods. Especially, where the absolute value of field map is high, the k-space method estimated water and fat components more precisely than other methods.

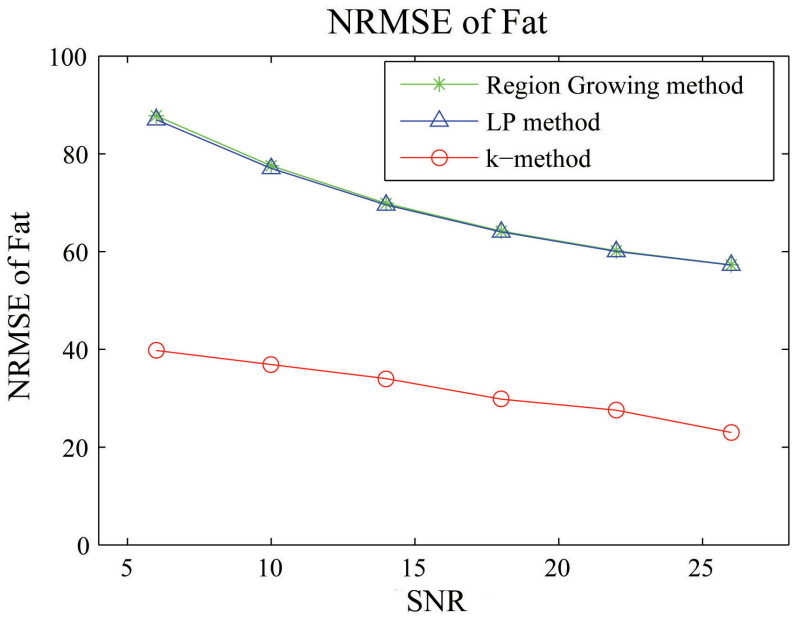

Fig. 5.2: Improvement of the k-space method in the NRMSE of fat estimates

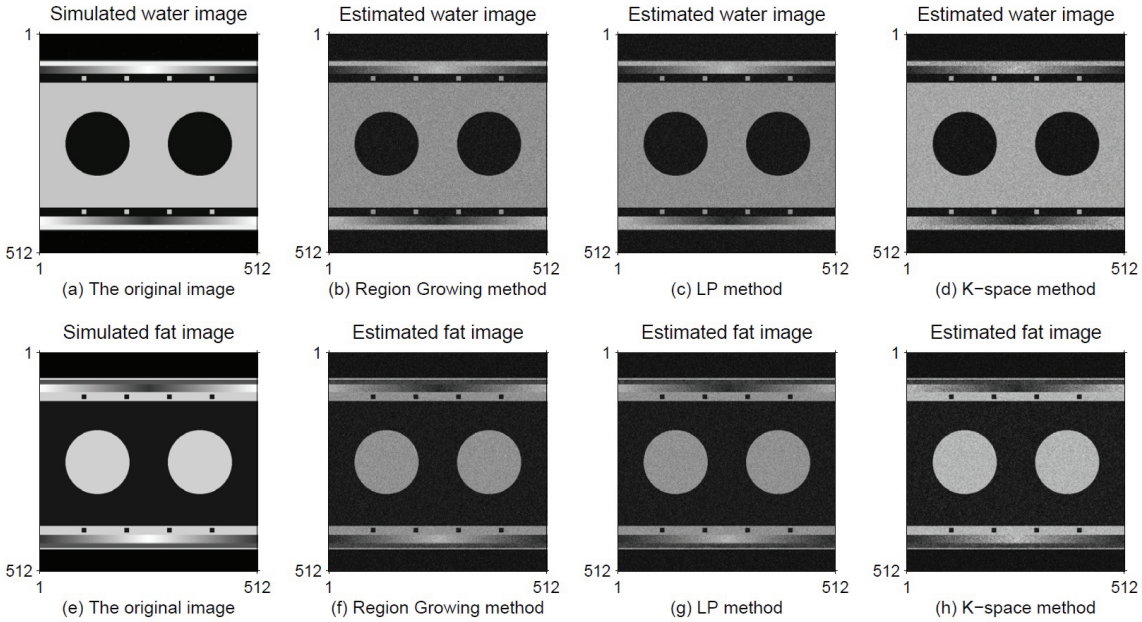

Fig. 5.3: First row: simulated water image and estimated water images of three methods. Second row: simulated fat image and estimated fat images of three methods.

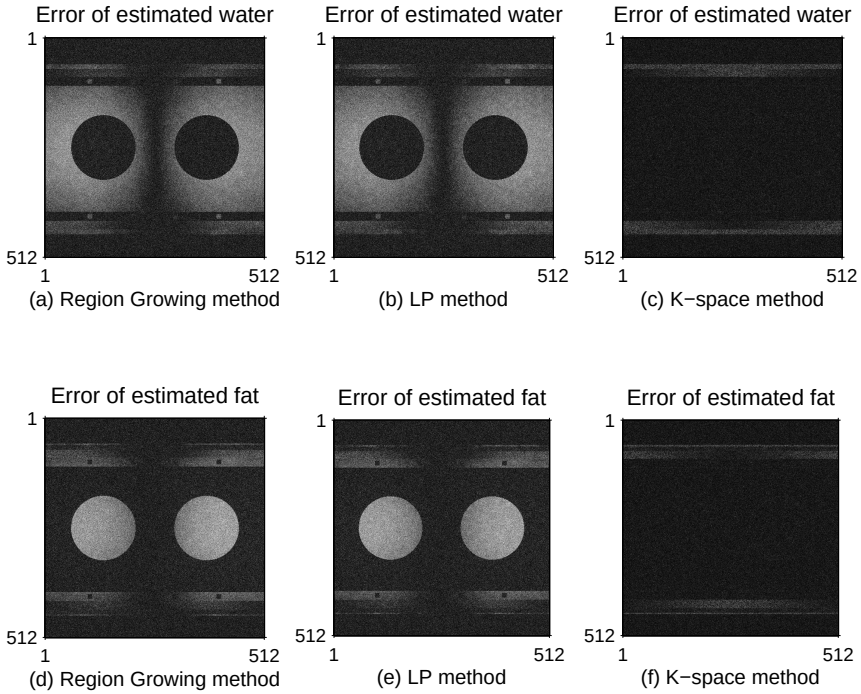

Fig. 5.4: First column: Region Growing method, Second column: LP method, Third column: K-space method.

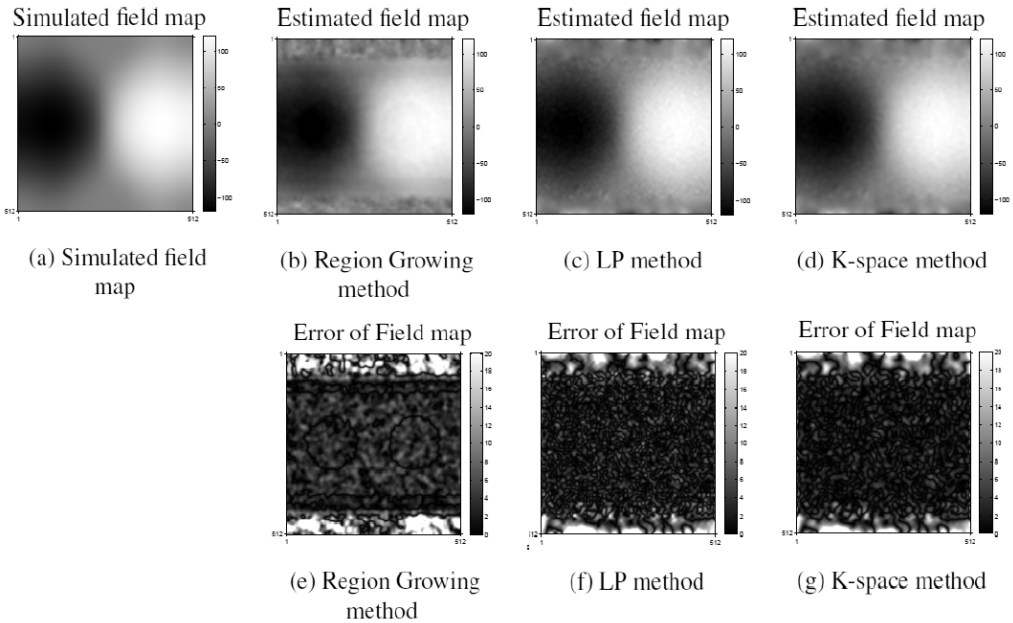

Fig. 5.5: First column : Simulated field map, Second column: Region Growing method, Third column: LP method, Fourth column: the k-space method.

Fig. 5.5(b), (c), and (d) show reconstructed field maps and Fig. 5.5(e), (f), and (g) show error images of the three methods. By looking at the error of field map for the three methods, it is evident that the LP method and the k-space method provide improved qualities over the region growing method, which contains the material structure. However, there were no apparent significant differences between estimated field maps of two methods. It remains somewhat mysterious why the MR¡SE in Fig. 5.1 and 5.2 were reduced so much by the K-space method.

5.4 Conclusions

We proposed a method for water-fat decomposition using MR K-space data. The experimental results show that the k-space method can lead to improved chemical components estimates compared Region Growing method and LP method as seen Fig. 5.1 and 5.2. The experimental results show that consideration of the data acquisition time can lead to enhanced chemical components estimates. Another potential advantage of the technique is that the RMSE of field map can be improved based on well estimated chemical components.

CHAPTER 6

CT Background

X-ray CT produces tomographic images of the spatial distribution of attenuation coefficient of the human body. These CT images are useful in medical diagnosis and in industry for nondestructive evaluation. We briefly describe the X-ray CT system with general measurement model and discuss the Dual-Energy CT measurement model and imaging methods in the following sections.

6.1 X-ray CT Measurement Physics

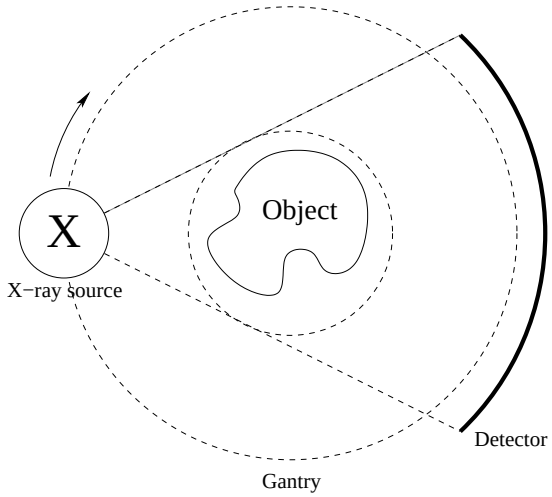

Fig. 6.1: Schematic diagram of a X-ray scanner.

The first major component of a CT system is the gantry which is a moveable frame that

contains the X-ray tube, the X-ray generator, detectors, and all associated electronics. Fig. 6.1 shows a typical X-ray scanner diagram. The source and the detector array are fixed on a gantry and rotate around the object. As the X-ray source produces radiation, detectors record thin beams of radiation that are attenuated by the patient at different angles. The final image is generated from these measurements utilizing basic principles, *e.g.*, filtered back projection (FBP).

6.1.1 General Measurement Model

Let Y_i denote the measurement for the ith ray of the incident spectrum. For a ray L_i of infinitesimal width, the mean of the projection measurements could be expressed as:

$$\bar{y}_i \triangleq \int I_i(\mathscr{E}) \exp\left(-\int_{\mathscr{L}_i} \mu(\vec{x},\mathscr{E})\,\mathrm{d}\ell\right) \mathrm{d}\mathscr{E} + r_i, \tag{6.1}$$

where $i = 1,...,N_d$ and N_d is the number of rays. $\mu(\vec{x},\mathscr{E})$ denotes the linear attenuation coefficient of the object which depends on the X-ray energy $\mathscr{E}_j$, $\int_{\mathscr{L}_i} \cdot\, \mathrm{d}\ell$ denotes the line integral along the ith ray, $I_i(\mathscr{E})$ denotes the product of the source spectrum for Ith ray, and the detector sensitivity at energy $\mathscr{E}$, and r_i denotes additive background contributions such as Compton scatter, dark current. The goal of X-ray CT image reconstructions (*e.g.*, FBP method) are to estimate $\mu(\vec{x},\mathscr{E})$ from the measured data, y_i. However, as we can notice in (6.1), it is not simple because $\mu(\vec{x},\mathscr{E})$ does not correspond to the CT measurements directly.

6.1.2 Dual-Energy CT Measurement Model

As we discussed in the previous section, linear attenuation coefficient depends on the X-ray energy because each photon energy is attenuated differently by the object. This dependence allows one to use CT scans to separate materials from CT measurements by using dual-energy X-ray imaging. Dual energy CT has many potential applications such

as material separation and attenuation correction for PET imaging. The dual energy CT measurement model has a very similar form to (6.1):

$$\bar{y}_{mi} \triangleq \int I_{mi}(\mathscr{E}) \exp\left(-\int_{\mathscr{L}_i} \mu(\vec{x},\mathscr{E})\,\mathrm{d}\ell\right) \mathrm{d}\mathscr{E} + r_{mi}, \tag{6.2}$$

where y_{mi} denotes the CT measurement for the ith ray for the mth incident spectrum, $m = 1,...,M_0$. Typically $M_0 = 2$ for DE CT.

We assume the linear attenuation coefficient can be represented using basis functions that are separable in the spatial and energy dimension as follows [2]:

$$\mu(\vec{x},\mathscr{E}) = \sum_{l=1}^{L_0} \sum_{j=1}^{N_\mathrm{p}} \beta_l(\mathscr{E}) b_j(\vec{x}) \rho_{lj}, \tag{6.3}$$

where $\beta_l(\mathscr{E})$ denotes the energy-dependent mass-attenuation coefficient of the lth material type, $\{b_j(\vec{x})\}$ are (unitless) spatial basis functions such as square pixels, and $\rho_l = (\rho_{l1},...,\rho_{lN_\mathrm{p}})$ denotes the vector of unknown density values of lth material type for each of the N_p voxels.

6.1.3 Dual-Energy Imaging Methods

The conventional approach to DE CT imaging is the dual-rotate mode (see Fig. 6.2). The gantry rotates around the object at one X-ray source voltage to collect sinogram data, a set of projections, and then the source voltage is changed and the source is rotated around again with the new kVp to collect a second sinogram. However, this conventional dual-rotate mode of DE CT is limited by motion artifacts: the patient may move between the two acquisitions, leading to inconsistencies between the two sinograms. Additionally due to the increased number of scans (one at a low energy and a second at a high energy), a dual energy CT system may necessitate higher radiation dose. To reduce the patient motion problems, several methods have been proposed. The three most common methods are the

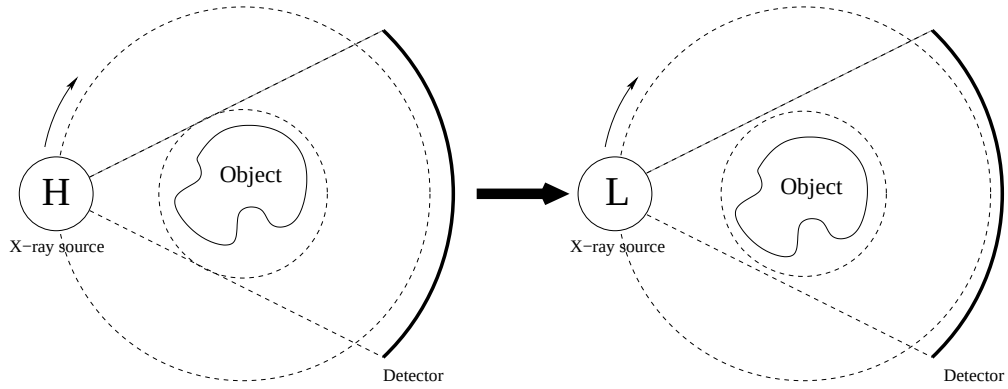

Fig. 6.2: Schematic diagram of a Dual rotate CT mode X-ray scanner.

dual-source CT mode [50], dual-layer detectors mode [18, 32], and fast kVp-switching mode [25, 28].

Dual source CT mode

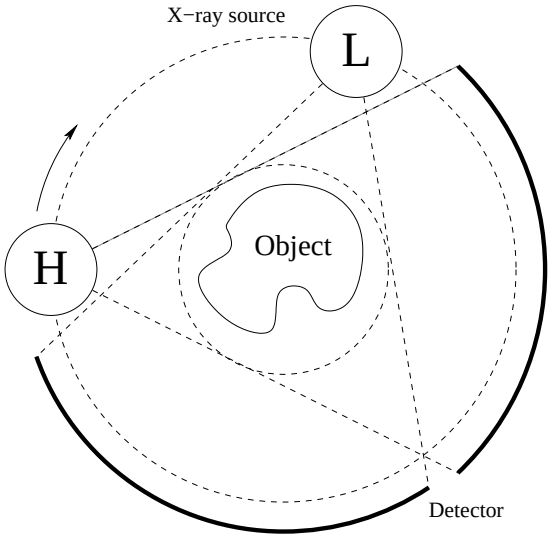

Fig. 6.3: Schematic diagram of a Dual source CT mode X-ray scanner.

The dual source CT system in Fig. 6.3 has two X-ray tubes and two corresponding detectors. Filtering, kVp, and intensity of the X-ray can be optimized for each of two X-ray tubes. The drawback of this mode is cross-scatter radiation; a natural consequence of simultaneous scanning with two X-ray sources. System cost is higher too.

Dual layer detectors mode

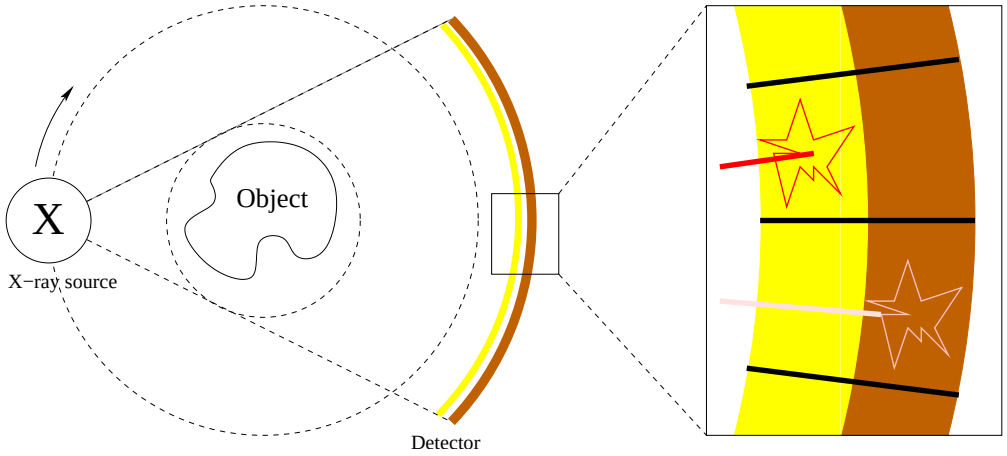

Fig. 6.4: Schematic diagram of a Dual-layer detectors mode X-ray scanner.

An alternative to using two X-ray sources using energy selective detectors. Fig. 6.4 illustrates a dual-layer detector that has only one source and two detectors; separation into low and high energy images occurs at the detector level. The upper detector layer primarily absorbs the low-energy x-ray spectrum, while the other layer detects the high-energy x-ray spectrum. In this dual-layer detectors mode, cross-scatter radiation problem is solved because it needs only one X-ray source tube. However, materials of detectors are difficult to optimize and the only filtering is due to the first layer so the recorded spectra are not very different between two layers.

Fast kVp-switching mode

For the fast kVp switching mode in Fig. 6.5, the X-ray source alternates between high and low tube voltages for alternating projection views. Modern CT systems rotate in less than 0.5 seconds, and collect about 1000 projection views, so the X-ray tube high voltage must be switched at kHz rates repeatably, which is a challenge that has been met only recently. In this switching mode, two sinograms are collected in a single rotation; the motion effect can be reduced dramatically. However, the fast kVp switching mode

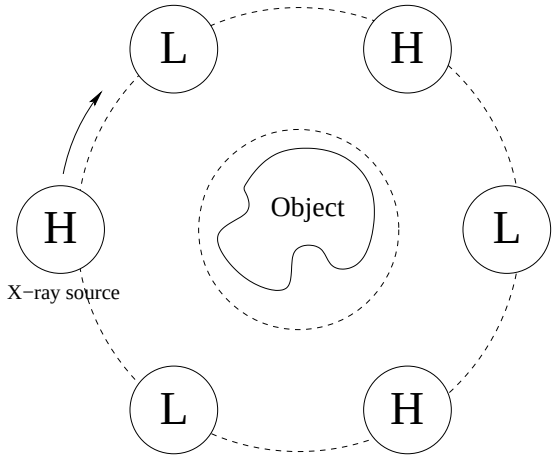

Fig. 6.5: Schematic diagram of a Fast kVp-switching mode X-ray scanner.

collects only half as many projection views as could be collected for each sinogram. We used the GE Discovery CT750HD CT scanner and the number of projections is 1968 projections/rotation (984 at 80 kVp and 984 at 140 kVp). Conventional sinogram domain DE decomposition methods require each ray to be measured twice by two different spectra (*e.g.*, two different tube voltages), but in the fast switching mode, the even projection views are at one voltage and the odd views are at the other voltage. This problem can be solved by using interpolation method or by iterative algorithms that will be described in chapters 7 and 8.

6.2 Filtered Back Projection

The goal of x-ray CT image reconstruction is to reconstruct the underlying object, (the patient), being imaged from the projection measurements. Image reconstruction methods or algorithms can be divided into two main categories: analytical methods, such as filtered back projection (FBP), and iterative methods, such as statistical methods. In this chapter, we briefly discuss the FBP method. We will present statistical methods in chapters 7 and 8.

FBP method is the most common analytical reconstruction technique. It is based on the Radon transform. The basic idea of the back projection is to duplicate measured sinogram

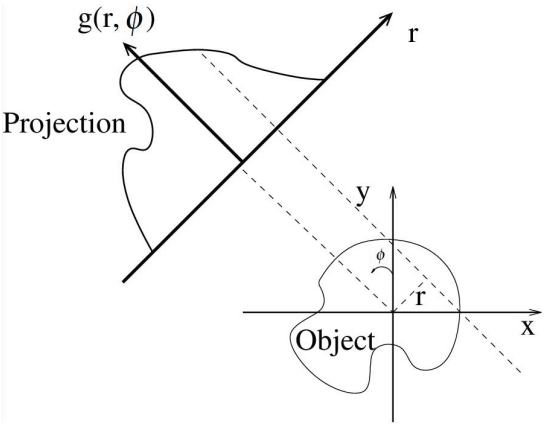

Fig. 6.6: Illustration of the back projection process.

values back into the object space along the corresponding rays. However, if we simply back project all measured projections, then this unfiltered back projection yields a blurry reconstructed image. Therefore, we need to apply filters to each projection such as a ramp filter before back projection.

Fig. 6.6 illustrates a parallel beam geometry. Let $g(r,\varphi)$ denotes the line integral through the object for projection angle φ, and $G_\varphi(\nu)$ denote 1D FT of the projection. By the projection-slice theorem, $G_\varphi(\nu) = F(\nu\cos\varphi, \nu\sin\varphi)$, where F denotes 2D Fourier transform of the object, $f(x,y)$. Therefore, the object $f(x,y)$ can be expressed as:

$$\begin{aligned} f(x,y) &= \int\int F(u,v)e^{-i2\pi(xu+yv)}dudv \\ &= \int_0^\pi \int_{-\infty}^\infty F(\nu\cos\varphi, \nu\sin\varphi)e^{-2\pi\nu(x\cos\varphi+y\sin\varphi)}|\nu|d\nu d\varphi \\ &= \int_0^\pi \breve{g}_\varphi(x\cos\varphi + y\sin\varphi)d\varphi, \end{aligned}$$

where $\breve{g}_\varphi$ denotes the filtered projection by using ramp filters as follows:

$$\breve{g}_\varphi(r) = \int_{-\infty}^\infty G_\varphi(\nu)|\nu|e^{i2\pi\nu r}d\nu. \tag{6.4}$$

Thus, the reconstructed object $\hat{f}(x,y)$ is defined as follows:

$$\hat{f}(x,y) = \int_0^{\pi} \breve{g}_{\varphi}(x\cos\varphi + y\sin\varphi)d\varphi. \tag{6.5}$$

This derivation ignores measurement noise and finite sampling, and leads to unnecessarily noisy reconstructed images. Model-based or statistical reconstruction methods, described next, can overcome these limitations of FBP.

CHAPTER 7

Model-based Image Reconstruction For Dual-Energy X-ray CT with Fast kVp Switching

This work is based on [25].

7.1 Introduction

The most recent generation of X-ray CT systems can collect dual energy (DE) sinograms by rapidly switching the X-ray tube voltage between two levels for alternate projection views. This reduces motion artifacts in DE imaging, but yields sinograms that may be angularly under-sampled. This chapter describes an iterative algorithm for statistical image reconstruction of material component images (*e.g.*, soft tissue and bone) directly from such under-sampled DE data, without resorting to the interpolation operations required by conventional DE reconstruction methods.

7.2 Dual-Energy Reconstruction

7.2.1 Models

Measurement model

Let y_{mi} denote the CT measurement for the ith ray for the mth incident spectrum, $m = 1, ..., M_0$, $i = 1, ..., N_\mathrm{d}$. For DE CT, $M_0 = 2$. The measurement means are related to

the line-integral projections of the object's attenuation via Beer's law. We assume that the measurements, y_{mi}, are random variables with the following ensemble means, $\bar{y}_{mi}$:

$$y_{mi} \sim \text{Poisson}\{\bar{y}_{mi}\} \tag{7.1}$$

$$\bar{y}_{mi} \triangleq \int I_{mi}(\mathscr{E}) \exp\left(-\int_{\mathscr{L}_i} \mu(\vec{x},\mathscr{E})\,\mathrm{d}\ell\right) \mathrm{d}\mathscr{E} + r_{mi}, \tag{7.2}$$

where $\int_{\mathscr{L}_i} \cdot\, \mathrm{d}\ell$ denotes the line integral along the ith ray, and $\mu(\vec{x},\mathscr{E})$ denotes the linear attenuation coefficient of the object being scanned at the spatial location $\vec{x}$, $I_{mi}(\mathscr{E})$ denotes the product of the mth incident source spectrum and the detector gain for the ith ray, and r_{mi} denotes additive background contributions such as room background, dark current, and scatter. We treat $I_{mi}(\mathscr{E})$ and r_{mi} as known nonnegative quantities [7, 53, 58].

Object model

The measurements are finite whereas μ is a continuous function of spatial location $\vec{x}$ and energy, $\mathscr{E}$. Thus for reconstruction we parameterize the linear attenuation coefficient using basis functions that are separable in the spatial and energy dimension as follows [2]:

$$\mu(\vec{x},\mathscr{E}) = \sum_{l=1}^{L_0} \sum_{j=1}^{N_\mathrm{p}} \beta_l(\mathscr{E}) b_j(\vec{x}) \rho_{lj}, \tag{7.3}$$

where $\beta_l(\mathscr{E})$ denotes the energy-dependent mass-attenuation coefficient of the lth material type (units cm^2/g), $\{b_j(\vec{x})\}$ are (unitless) spatial basis functions such as square pixels, and $\rho_l = (\rho_{l1}, ..., \rho_{lN_\mathrm{p}})$ denotes the vector of unknown density values of lth material type (units g/cm^3) for each of the N_p voxels. In DE CT, we usually choose $L_0 = 2$, *e.g.*, soft tissue (water) and bone. We use tabulated mass-attenuation coefficient values for water and bone [24].

Most conventional approaches to DE CT imaging have estimated the object material densities, $\{\rho_l\}_{l=1}^{L_o}$, from fully sampled measurements, $\{y_{mi}\}_{i=1}^{N_\mathrm{d}}$. Here our goal is to reconstruct the object from fast kVp-switched sinograms that are collected by alternating X-ray

source voltage over a single rotation. Therefore, the proposed method estimates $\{\rho_l\}_{l=1}^{L_0}$ from $\{y_{mi}\}_{i\in\mathscr{I}_m}$ where the sets of indexes $\{\mathscr{I}_m\}_{m=1}^{M_0}$ are a partition of whole index set $I=\{1,...,N_\mathrm{d}\}$. In particular, for DE CT with fast kVp-switching between two source voltages, $\mathscr{I}_1$ and $\mathscr{I}_2$ correspond to the rays in the odd and even projection views respectively. Using (7.2), (7.3), we rewrite the ensemble means of the measurements as follows:

$$\bar{y}_{mi}(\rho) = I_{mi}\mathrm{e}^{-f_{mi}(\mathbf{s}_i(\rho))} + r_{mi} \tag{7.4}$$

$$f_{mi}(\rho) \triangleq -\log v_{mi}(\mathbf{s}_i(\rho)) \tag{7.5}$$

$$v_{mi}(\rho) \triangleq \int p_{mi}(\mathscr{E})\mathrm{e}^{-\beta(\mathscr{E})\cdot\mathbf{s}_i(\rho)}\,\mathrm{d}\mathscr{E}, \tag{7.6}$$

for $m=1,...,M_0$, $l=1,...,L_0$, and $i\in\mathscr{I}_m$, where $I_{mi}=\int I_{mi}(\mathscr{E})\,\mathrm{d}\mathscr{E}$ denotes the total intensity for the mth incident spectrum and the ith ray, $p_{mi}(\mathscr{E}) \triangleq I_{mi}(\mathscr{E})/I_{mi}$ denotes the normalized intensity for the mth incident spectrum and the ith ray, and $\beta(\mathscr{E}) \triangleq (\beta_1(\mathscr{E}),...,\beta_{L_0}(\mathscr{E}))$ denotes the energy-dependent mass-attenuation coefficient, and we define the sinogram vector $\mathbf{s}_i$ as follows:

$$\mathbf{s}_i(\rho) \triangleq (\mathbf{s}_{i1}(\rho),...,\mathbf{s}_{iL_0}(\rho)),$$

$$s_{il}(\rho) \triangleq [A\rho_l]_i,$$

where A denotes the $N_\mathrm{d}\times N_\mathrm{p}$ system matrix having elements

$$a_{ij} \triangleq \int_{\mathscr{L}_i} b_j(\vec{x})\,\mathrm{d}\ell. \tag{7.7}$$

We refer to the nonlinear function $f_{mi}(\mathbf{s}_i)$ as the "beam hardening" function. If we had a monoenergetic source, then this function would be linear. But for polyenergetic spectra, this function depends nonlinearly on its arguments, the material density line integrals, and this nonlinearity is one of the challenges of DE CT reconstruction.

7.2.2 Conventional Interpolation/FBP approach

Due to the nonlinear model (7.2), it is challenging to estimate the object ρ directly. Therefore, conventional methods first estimate the nonlinear function values f_{mi} by inverting (7.4):

$$\hat{f}_{mi} \triangleq -\log\left(\text{smooth}\left\{\frac{Y_{mi}-r_{mi}}{I_{mi}}\right\}\right), \tag{7.8}$$

where radial smoothing is often included to reduce noise [23]. Note that, we used $|Y_{mi} - r_{mi}|$ instead of $Y_{mi} - r_{mi}$ to avoid negative value in this work. Using angular interpolation, one can reconstruct $\hat{f}_{mi}$ for all $i = 1,2,...,N_{\text{d}}$. For the results shown below, we simply averaged the two nearest projection views for interpolation. Then one applies conventional DE decomposition [2], followed by FBP reconstruction. In this work, we used the ramp filter apodized by a Hanning window having cutoff frequency 0.5 cycles / sample for FBP reconstruction. This approach is fast but suboptimal especially for low-dose X-ray CT.

7.2.3 Penalized Weighted Least Square (PWLS) approach

Instead of estimating ρ by using interpolation, we propose to estimate ρ directly by including a spatial roughness penalty $\text{R}(\rho)$ in the following penalized weighted least square cost function:

$$\hat{\rho} = \arg\min_{\rho \geq 0} \Psi(\rho) \tag{7.9}$$

$$\Psi(\rho) \triangleq \sum_{m=1}^{M_0} \sum_{i \in \mathscr{I}_m} \frac{w_{mi}}{2} (\hat{f}_{mi} - f_{mi}(\rho))^2 + R(\rho), \tag{7.10}$$

where ρ denotes a $2N_p^2 \times 1$ object vector in this study, w_{mi} denotes weights that we define as follows:

$$w_{mi} = Y_{mi}, \text{ for } i \in \mathscr{I}_m. \tag{7.11}$$

This cost function is non convex cost function so a good initial estimator is important to converge to a desirable local minimum. These weights are a reasonable choice because

CT measurements are approximately Poisson distributed and in the absence of smoothing the approximate variance of $\hat{f}_{mi}$ is [10, 11]:

$$\mathrm{Var}(\hat{f}_{mi}) \approx \frac{\mathrm{Var}(Y_{mi})}{(\bar{y}_{mi} - r_{mi})^2}. \tag{7.12}$$

Note that (7.10) uses *only* the measured rays ($i \in \mathscr{I}_m$); no interpolation is used. The regularizing penalty term in (7.10) is given by the following:

$$R(\rho) = \sum_{l=1}^{L_0} \sum_{j=1}^{N_\mathrm{p}} \sum_{k \in \mathscr{N}_j} \psi(\rho_{lj} - \rho_{lk}), \tag{7.13}$$

where ψ is a potential function and $\mathscr{N}_j$ is a neighborhood of pixel j. For ψ we used a hyperbola [4] and the modified regularizer in [15] to provide approximately uniform spatial resolution. Here we minimized the cost function in (7.10) using 100 iterations of a conjugate graduate method [8, 16, 55] with a monotone line search technique [13]. This could be accelerated greatly by using ordered subsets [1]. We initialized the iterations using the object estimated by the interpolation/FBP method in Section 7.2.2.

7.3 Results

To evaluate the feasibility of the proposed methods for image reconstruction, we performed a computer simulation of dual-energy CT scans and a real phantom DECT scans. In both cases, the reconstructed images were 512×512 with 0.1×0.1 cm^2 pixel size and the projection space was 888 radial samples $\times$ 984 angular views. We used source voltages 80kVp and 140kVp and we used X-ray spectra model provided by GE CATSIM software [9], including the effects of a standard large bow-tie filter. The rotation center is 54.1 cm from the source, and the detector is 94.9 cm form the source.

7.3.1 Simulation

We applied both the conventional dual-energy interpolation/FBP reconstruction method, and the proposed regularized PWLS method. We investigated 10 different numbers of incident photons per ray ($I_{mi} = I_0$) from 1×10^5 to 1×10^6.

Fig. 7.1 shows the density maps of the components: soft tissues and bone mineral and the estimated object of the two methods with $I_0 = I_{mi} = 10^5, i \in \mathscr{I}_m$. The PWLS images have reduced streak artifacts and lower noise than the conventional FBP images. As seen in Fig. 7.1, the PWLS images reconstructed from interpolated sinograms are very similar to the PWLS image reconstructed from the fast kVp-switching sinograms. This result is unsurprising because interpolation does not provide any new information, but rather simply uses combinations of existing data values. The main advantage of statistical image reconstruction methods is the ability to model the noise in sinogram measurements. Interpolation produces sinogram values that are correlated with each other and thus less amenable to statistical modeling. As noted previously, our statistical DE CT approach can use the original fast kVp-switching sinograms rather than needing interpolated sinograms, but this is a secondary benefit compared to the statistical modeling. However, it also appears that the estimated bone material component is nonzero in the soft tissue of the phantom. This bias could be caused by the regularizer; we discuss it further in Chapter 9.

Fig. 7.2 shows that the proposed PWLS method reduces significantly the NRMSE of the soft tissue and bone images compared to the conventional interpolation/FBP method.

Fig. 7.3 illustrates that the proposed PWLS method has lower noise than FBP without compromising the spatial resolution near object edges.

For completeness, we also applied the PWLS method to the interpolated sinogram data. Fig. 7.1(g) and (h) show their resulting component images. The global NRMSE of the soft tissue and bone components were 14.8% and 11.9% respectively, compared to

14.6% and 11.9% for PWLS applied to the sinograms without interpolation. Therefore, the results show that the qualities of the estimated material components with and without interpolation are essentially the same. When implemented efficiently, applying PWLS to interpolated data requires approximately twice the compute time per iteration as applying PWLS to the original fast kVp-switched data.

7.3.2 Phantom

We applied the conventional FBP reconstruction method, dual-energy interpolation/FBP reconstruction method, and the proposed regularized PWLS method to real phantom. The phantom image contains four cylinders: one large cylinder and three smaller cylinders. As described in [34], this 20 cm diameter phantom contains three 5 cm diameter cylindrical inserts containing (top) air, and (bottom) a solution of $CaCl_2$ equivalent to bone, having a 278 HU difference between 80 and 140 kVp scans and a dilute iodine-based contrast agent, with a 700 HU difference. The sinogram data was fully sampled so we downsampled the high- and low-energy sinograms to emulate a fast kVp-switching scan. (This emulation is imperfect because it disregards the finite rise and fall times of the tube kVp [64, 67] that can degrade spectral separation in an actual fast kVp scan.) This phantom scan was a low dose, 5mAs (10 mA $\times$ 0.5 sec), study and the slice thickness is 0.625 mm.

Fig. 7.4 shows the component material images reconstructed by the three methods. Fig. 7.4(a)-(b) shows the conventional (fully sampled) FBP images, whereas Fig. 7.4(c)-(d) shows interpolation/FBP method from emulated fast kVp-switching views. Both methods' results are noisy and have many streaks due to the low dose of this CT data. However, the PWLS images, in Fig. 7.4(e)-(f), have successfully reduced streak artifacts and yield lower noise than other two methods even though it also the used kVp-switched CT

data. For completeness, we also applied the proposed method to the interpolated DE data. Fig. 7.4(g)-(h) shows the resulting images. As shown in Fig. 7.4, the proposed method has almost the same performance and yields images that are very similar to Fig. 7.4(e) and (f). However, we observed undesirable variations in spatial resolution and cross talk between the soft tissue and bone material images. In Fig. 7.5 (a) the red box highlight the regions where this cross talk problem can be found for soft tissues in Fig. 7.1 (g). We zoom-in on this region in Fig. 7.5 (b).

7.4 Conclusion

We presented an iterative regularized PWLS algorithm for DE CT reconstruction from the type of under-sampled DE data that is collected by fast kVp-switching CT systems. Unlike other DE CT algorithms, the proposed method estimates material component images directly from only half as many projection views without *any* interpolation operation. The experiments show that the proposed method yields images with lower NRMS error than the conventional interpolation/FBP approach in Fig. 7.2. However, we observed the cross talk problem between the soft tissue and bone material images especially in edge areas. We believe that the cross-talk problem in the proposed approach to DE CT image reconstruction is caused by the fact that each measured sinogram (*e.g.*, low energy and high energy sinogram) depends on all material components. Even if the X-ray source were monoenergetic, and even if we had energy discriminating photon-counting detectors, each measured sinogram would still be influenced by all material components. This type of relationship appears to cause "coupling" between the material density estimates when using "conventional" regularized image reconstruction methods. We analyze this problem further in Chapter 9 and investigate an alternative reconstruction approach in Chapter 10.

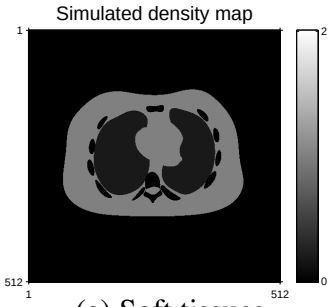

(a) Soft tissues

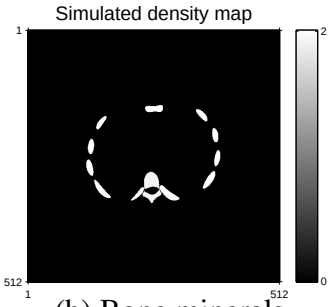

(b) Bone minerals

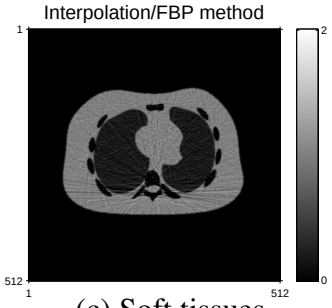

(c) Soft tissues

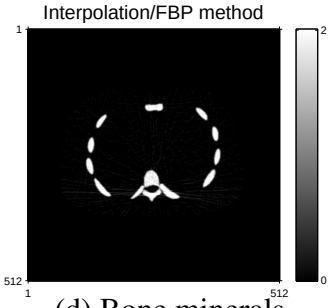

(d) Bone minerals

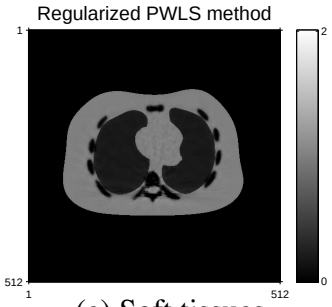

(e) Soft tissues

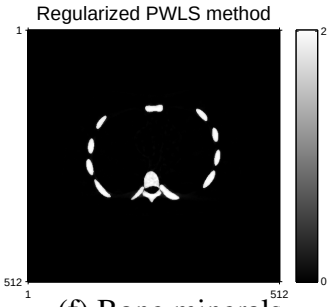

(f) Bone minerals

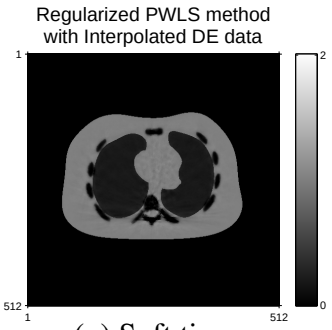

(g) Soft tissues

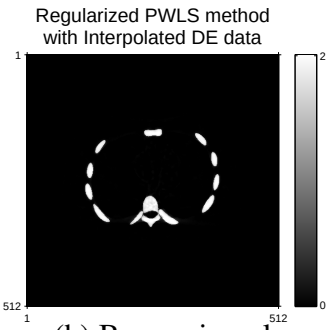

(h) Bone minerals

Fig. 7.1: First row: Two component simulated densities. Second row: Interpolation/FBP method with $I_0 = 10^5$. Third row: Regularized PWLS method with $I_0 = 10^5$. Fourth row: Regularized PWLS method with interpolated DE data.

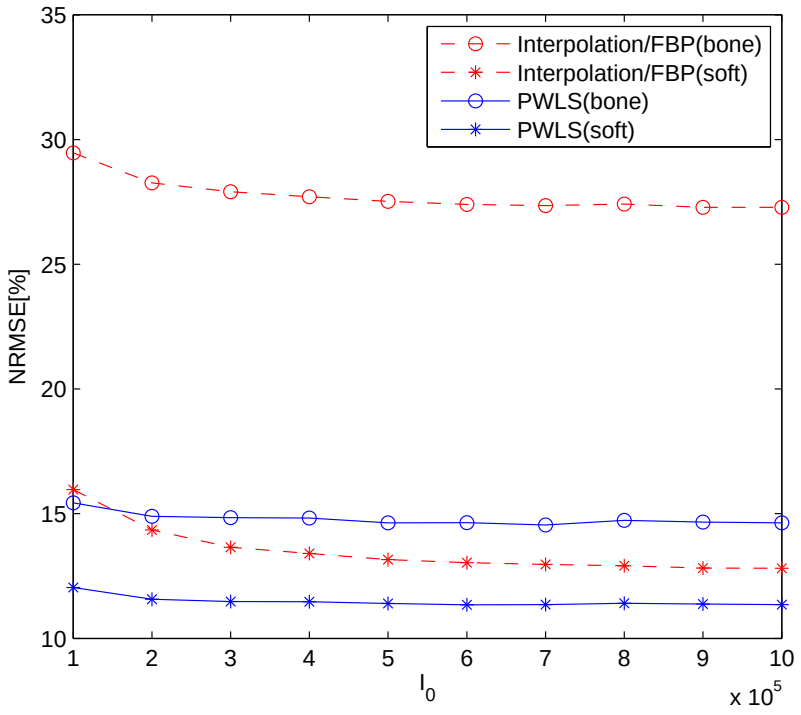

Fig. 7.2: NRMSE of estimated density maps: Interpolation/FBP method, and proposed PWLS algorithm.

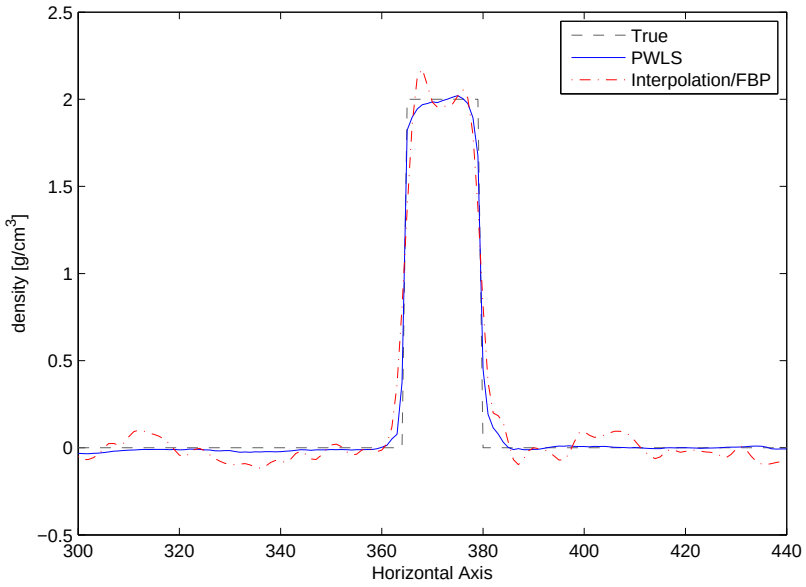

Fig. 7.3: Horizontal profile through the estimated bone images of the two methods and the true bone image.

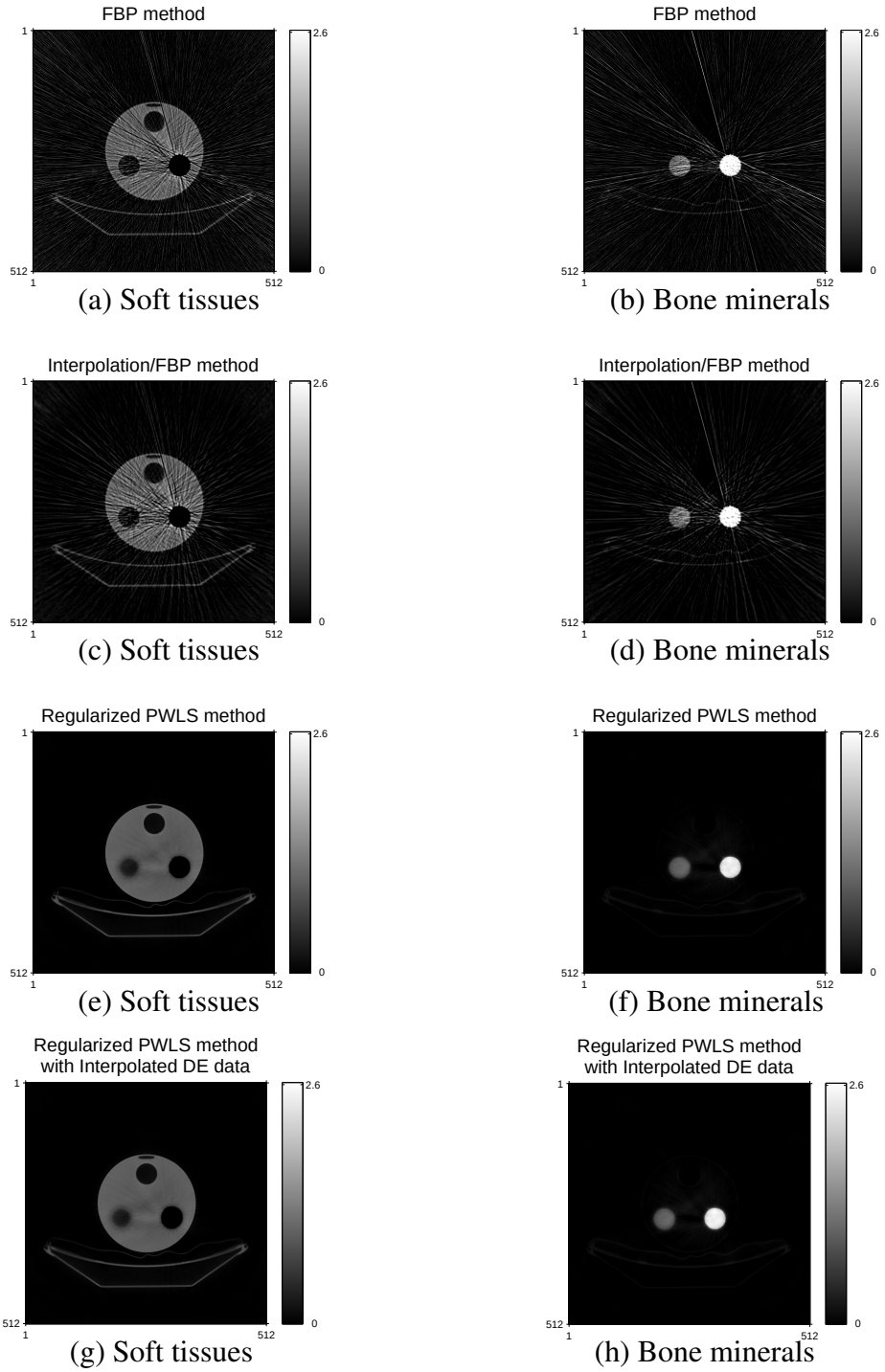

Fig. 7.4: First row: FBP method, Second row: Interpolation/FBP method, Third row: PWLS method, Fourth row: PWLS method from interpolated DE data.

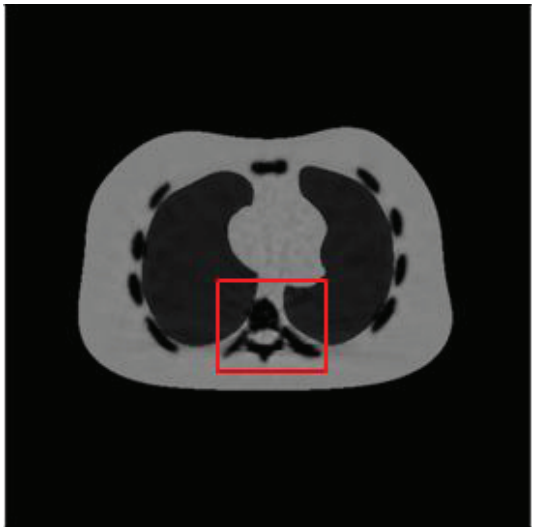

(a) Estimated soft tissues

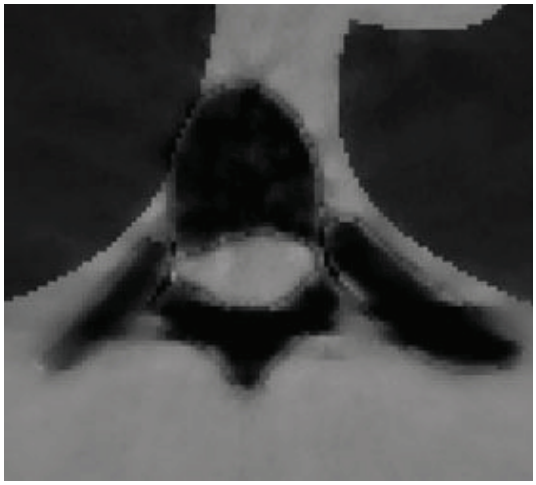

(b) Enlarged image

Fig. 7.5: Cross talk problem. (a) Estimated soft tissues where the red boxes indicate the regions where the effect of the cross talk problem is found. (b) Enlarged images of the boxed region.

CHAPTER 8

Fast kVp-Switching Dual-Energy CT for PET Attenuation Correction

This work is based on [28].

8.1 Introduction

CT-based attenuation correction (CTAC) for PET has advantages over conventional attenuation correction by PET transmission scans, including better spatial resolution and lower noise [3, 33, 35]. However, PET attenuation correction factors (ACFs) must be computed for 511 keV photon energy, whereas X-ray CT spectra cover a wide range of lower photon energies. These spectral differences can lead to imperfect PET attenuation correction, particularly when iodinated contrast agents are present [34, 56]. Conventional CTAC approaches use a single X-ray source voltage (kVp) and its corresponding spectrum. DECT imaging methods have the potential to improve attenuation correction in PET by exploiting the spectral information provided by using two different X-ray spectra. Noh et al. previously investigated a statistically motivated, sinogram-domain approach for estimating the line integrals of two material components from DECT scans followed by computing the 511 keV ACFs [45, 46]. That approach is iterative, but is relatively fast because the iterations are solely in the sinogram domain.

A disadvantage of sinogram-domain approaches to DECT decomposition is that the types of regularization that are suitable are limited. In contrast, by iteratively reconstructing images from the measured sinograms, one can apply a wide variety of sophisticated regularizers because there can be clear distinctions between different tissue types in the images. In the sinogram domain, region boundaries are barely visible, and other forms of prior information about the object's attenuation properties are not readily apparent. Therefore, the goal of this chapter is to study statistical methods for reconstructing material component images from DE sinogram data [14] for the purpose of PET attenuation correction. This section used the same parameters and equations as in section 7.2.

8.2 Attenuation Correction Factors

We assume PET measurements have independent Poisson distribution:

$$Y_i \sim \text{Poisson}\{\bar{Y}_i(\lambda)\}, i = 1, ..., N_r,$$

where N_r denotes the number of detector pairs, and $\bar{Y}_i$ denotes the mean of the ith measurement:

$$\bar{Y}_i(\lambda) = \sum_j p_i a_{ij} \lambda_j + s_i, \tag{8.1}$$

where the survival probability is

$$p_i = \exp\left(- \int_{L_i} \mu(\vec{x}; 511)\, \mathrm{d}\ell \right).$$

The system matrix is a_{ij} and scatter and s_i denotes the mean contribution of scatter and randoms to the ith ray. λ_j denotes the distribution of the radio-isotope.

For reconstructing the PET emission images, one must compensate for the attenuation of annihilated photons at the PET energy (511 keV). In CTAC, the ACF for the ith ray is defined as follows:

$$\text{ACF}_i \triangleq \exp\left(\sum_{l=1}^{L_0} \beta_l(\mathscr{E}) [A\hat{\rho}_l]_i \right) \Big|_{\mathscr{E}=511keV}, \tag{8.2}$$

where $\hat{\rho}_l$ is an estimated density map corresponding to the lth material.

In this work, we focused on the error in the PET images due to imperfections in the ACFs, so we generated noiseless PET data $\bar{Y}_i$ using (8.1) with no scatter or randoms ($s_i = 0$). We then divided the PET sinograms by the estimated ACFs (8.2) and applied the FBP method to reconstruct PET emission images.

We investigated four choices for the material density images ρ: i) The true density maps ρ; ii) density map estimates $\hat{\rho}$ formed by the "interpolate/FBP" approach, from fast kVp-switching DE sinograms; iii) density map estimates $\hat{\rho}$ formed from fully sampled DE sinograms with sinogram-domain decomposition followed by FBP reconstruction, called the "FBP method"; iv) density map estimates $\hat{\rho}$ reconstructed by the iterative PWLS method.

8.3 Results

We performed a preliminary examination of the proposed methods using a simulation of DE-based CTAC for PET. We applied the proposed method to dual-energy CT scans of a phantom with source voltages 80kVp and 140kVp. The reconstructed images were 512×512 with 0.1×0.1 cm^2 pixel size. The fan-beam projection space was 888 radial samples $\times$ 984 angular views over 360° degrees and we used X-ray spectra model provided by GE CATSIM software [9], including the effects of a standard large bow-tie filter. To evaluate the performance of the proposed method for CTAC, we compared it to two traditional methods: the (fully sampled) FBP method and the interpolation/FBP method. We applied three methods to simulated data with the same parameters used for the real phantom data in section 7.3.

Fig. 8.1 shows the NRMSE plot of estimated density maps with different incident intensities, I_0. We observed that the proposed method significantly reduces the NRMSE

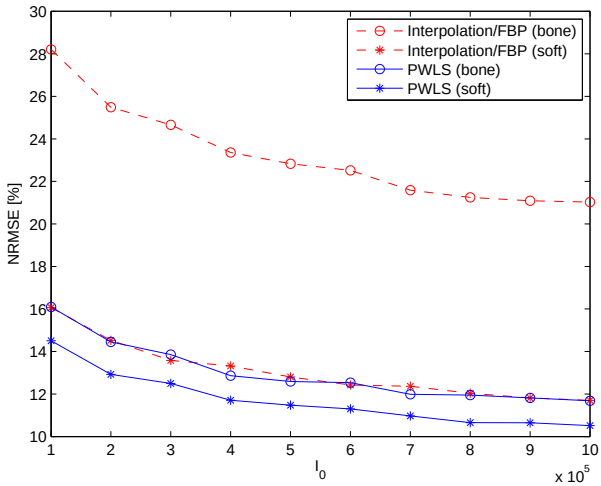

Fig. 8.1: NRMSE of estimated density maps: Interpolation/FBP method, and the proposed method.

of soft tissue and bone minerals compared to the interpolation/FBP method.

Fig. 8.2 shows the (FBP) reconstructed PET emission images based on the various methods for estimating the ACFs. The PET images in Fig. 8.2(d) are based on ACFs from the PWLS DE reconstruction method. This CTAC approach provides reduced noise and streak artifacts compared to the other methods in Fig. 8.2(b)-(c). We used the same estimated density maps of bone minerals and soft tissue in Chapter 7.

Fig. 8.3 compares the NRMSE of the reconstructed PET images. The NRMSE of the PET image based on the PWLS ACFs is significantly lower than the other competing methods investigated here.

8.4 Conclusion

We presented an iterative PWLS algorithm for DE CT reconstruction, motivated by improving attenuation correction in PET. The regularized method estimates the two material component images directly from DE sinograms including the type of under-sampled DE data that is collected by fast kVp-switching CT systems. Unlike other DE CT algorithms, the proposed method estimates material component images directly from only

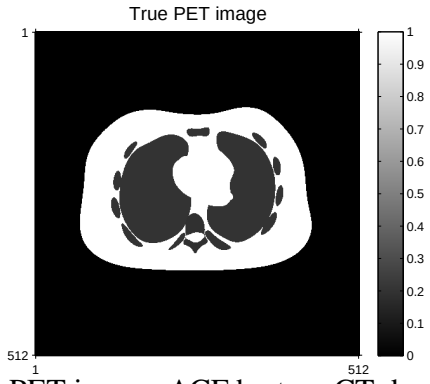

(a) PET image, ACF by true CT density map

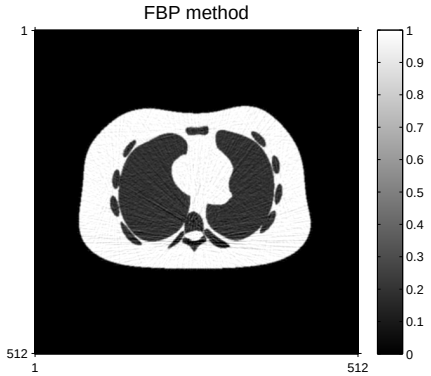

(b) PET image, ACF by FBP method

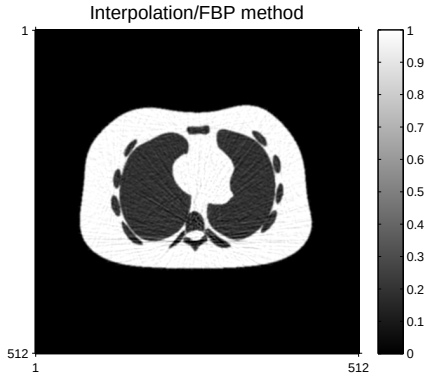

(c) PET image, ACF by Interpolation/FBP method

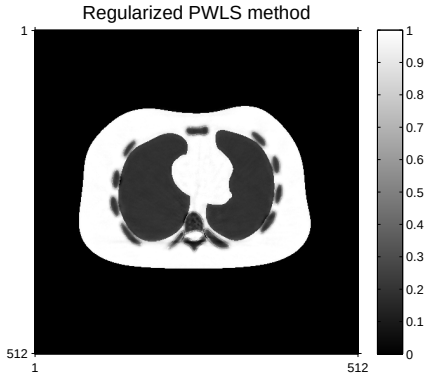

(d) PET image, ACF by Regularized PWLS method

Fig. 8.2: Reconstructed PET emission images using competing attenuation correction methods.

half as many projection views without *any* interpolation operation. Using these estimated DE CT images yields more accurate ACFs than conventional approaches. However, we observed the cross talk problem again and the next chapter explores this problem further.

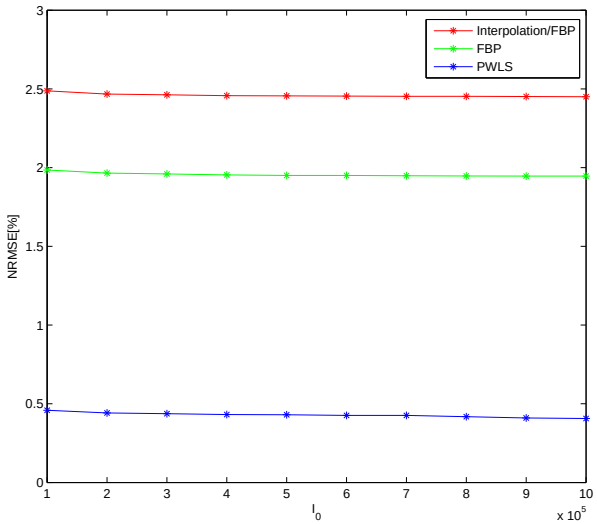

Fig. 8.3: NRMSE of reconstructed PET images: Interpolation/FBP method, and the proposed method, versus I_0 (number of incident X-ray photons per ray).

CHAPTER 9

Spatial Resolution Analysis

9.1 Introduction

In Chapter 7, we proposed an iterative algorithm for DE CT reconstruction. The regularized method estimates two material images from under-sampled DE sinograms without any interpolation. However, in both 7 and 8, we also observed undesirable variations in spatial resolution and cross talk between the reconstructed soft tissue and bone material images. This cross talk problem is challenging because of the nonlinearities of the beam hardening function $f(\cdot)$ in DECT with polyenergetic spectra.

In this chapter, we analyze the spatial resolution and noise properties of statistical methods in hopes of reducing the crosstalk between material component estimates. The goal of this chapter is to try to extend the regularization design of [15] so that one achieves object-independent spatial resolution for DE CT with PL reconstruction.

9.2 Local Impulse Response

First we define x_{lj} as the jth pixel of the lth object material, $j = 1,\ldots,N$, s_{li} as the ith pixel of the lth material sinogram, $i = 1,\ldots,M$ and G as a $M \times N$ system matrix to project image domain to sinogram domain. Our measurement model is:

$$\mathsf{E}[y_{mi}] = I_{mi} e^{-f_{mi}(x)} + r_{mi},\ i = 1,\ldots,M, \tag{9.1}$$

where $f_{mi}(x) = -\log v_{mi}(x), v_{mi}(x) = \int P_{mi}(\mathscr{E}) e^{-\sum_l \beta_l(\mathscr{E})[G\cdot x_l]_i} \, \mathrm{d}\mathscr{E}, P_{mi}(\mathscr{E}) = I_{mi}(\mathscr{E})/I_{mi}, I_{mi} = \int I_{mi}(\mathscr{E}) \, \mathrm{d}\mathscr{E}$, and $\beta_l(\mathscr{E})$ denotes the mass attenuation coefficients. For other parameters, this section used the same parameters in section 7.2. We proposed the penalized weighted least-squares cost function in section 7.2.3 as:

$$\hat{x}(y) = \arg\min_{x \geq 0} \Psi(x, y) \tag{9.2}$$

$$\Psi(x, y) \triangleq L(x, y) + R(x) \tag{9.3}$$

$$L(x, y) = \sum_m \sum_i \frac{w_{mi}}{2} (\hat{f}_{mi}(y) - f_{mi}(x))^2, \tag{9.4}$$

where, $w_{mi} = Y_{mi}$ for $i \in I_m$, $R(x)$ is a spatial roughness penalty function, $x \triangleq \begin{pmatrix} x_1 \\ x_2 \end{pmatrix}$, and x_l denotes the lth material. Note that in (9.3) we used the estimated log data of conventional methods, $\hat{f}_{mi}$, in our data fitting term:

$$\hat{f}_{mi}(y) \triangleq -\log\{\text{smooth}(\frac{y_{mi} - r_{mi}}{I_{mi}})\}. \tag{9.5}$$

For this cost function, the lth material's local impulse response (2.12) is

$$l_l^{(j)}(x) = [-\nabla^{[2,0]} L(\check{x}, \bar{y}(x)) + \beta \mathbb{R}(\check{x})]^{-1} [\nabla^{[1,1]} L(\check{x}, \bar{y}(x))] \frac{\partial}{\partial x_{lj}} \bar{y}(x) \tag{9.6}$$

$$= [-\nabla^{[2,0]} L(\check{x}, \bar{y}(x)) + \beta \mathbb{R}(\check{x})]^{-1} [\nabla^{[1,1]} L(\check{x}, \bar{y}(x))] \nabla \bar{y}(x) e_l^{(j)}, \tag{9.7}$$

where $\mathbb{R}(x)$ denotes the $2N \times 2N$ Hessian of the regularizer, $\bar{y} = \mathsf{E}[y]$, $\nabla \bar{y}(x) = \frac{\partial}{\partial x} \bar{y}(x)$, $\check{x} = \hat{x}(\bar{y}(x))$, and $e_1^{(j)}$ denotes the extended Kronecker impulse, e^j:

$$e_1^{(j)} = \begin{pmatrix} e^j \\ 0 \end{pmatrix} \text{ for } l = 1 \text{ and, } e_2^{(j)} = \begin{pmatrix} 0 \\ e^j \end{pmatrix} \text{ for } l = 2 \, .$$

Note that, the negative log-likelihood L in (9.4) is minimized at the true x when given noiseless data $\bar{y}(x)$. Therefore, $x = \arg\min_z L(z, \bar{y}(x))$, so

$$0 = \nabla^{[1,0]} L(x, \bar{y}(x)). \tag{9.8}$$

Therefore, when we differentiate both sides with respect to x:

$$\begin{aligned}
&\nabla^{[2,0]}L(x,\bar{y}(x)) + \nabla^{[1,1]}L(x,\bar{y}(x))\nabla\bar{y}(x) = 0 \\
\Longleftrightarrow &\nabla^{[2,0]}L(x,\bar{y}(x)) = -\nabla^{[1,1]}L(x,\bar{y}(x))\nabla\bar{y}(x) \\
\Longleftrightarrow &\nabla^{[2,0]}L(\check{x},\bar{y}(x)) \approx -\nabla^{[1,1]}L(\check{x},\bar{y}(x))\nabla\bar{y}(x). \qquad (9.9)
\end{aligned}$$

Substituting this (9.9) into (9.7) yields the final local impulse response of the penalized-likelihood:

$$l_l^{(j)}(x) = [F(\check{x}) + \beta\mathbb{R}(\check{x})]^{-1}F(\check{x})e_l^{(j)}, \qquad (9.10)$$

where $F(x) = \nabla^{[2,0]}L(\check{x},\bar{y}(x))$. For (9.4), L is additively separable and has the following gradients:

$$\begin{aligned}
[F_{l_1l_2}(x)]_{jk} &= \frac{\partial^2}{\partial x_{l_1j}\partial x_{l_2k}}L(x) \\
&= \sum_m\sum_i w_{mi}\left\{(\frac{\partial}{\partial x_{l_1j}}f_{mi}(x))(\frac{\partial}{\partial x_{l_2k}}f_{mi}(x)) - (\hat{f}_{mi}(y) - f_{mi}(x))(\frac{\partial^2}{\partial x_{l_1j}\partial x_{l_2k}}f_{mi}(x))\right\} \\
&\approx \sum_m\sum_i w_{mi}(\frac{\partial}{\partial x_{l_1j}}f_{mi}(x))(\frac{\partial}{\partial x_{l_2k}}f_{mi}(x)) \\
&= \sum_m\sum_i w_{mi}g_{ij}g_{ik}\frac{U_{mil_1}(x)U_{mil_2}(x)}{v_{mi}^2(x)},
\end{aligned}$$

where

$$U_{mil_1} = \int \beta_{l_1}(\mathscr{E})P_{mi}(\mathscr{E})e^{-\sum_l\beta_l(\mathscr{E})[G\cdot x_l]_i}\,\mathrm{d}\mathscr{E}.\ (\because \frac{\partial}{\partial x_{l_1j}}f_{mi} = g_{ij}(U_{mil_1}/v_{mi})) \qquad (9.11)$$

Therefore, the Fisher information matrix $F = \begin{pmatrix} F_{11}(x) & F_{12}(x) \\ F_{12}(x) & F_{22}(x) \end{pmatrix}$, can be factored as follows:

$$F(x) = G_2' \cdot D(x) \cdot G_2, \qquad (9.12)$$

where

$$G_2 = \begin{pmatrix} G & 0 \\ 0 & G \end{pmatrix}, \; D(x) = \begin{pmatrix} D_{11}(x) & D_{12}(x) \\ D_{21}(x) & D_{22}(x) \end{pmatrix},$$

$$D_{l_1 l_2}(x) = \text{diag}\{\sum_m w_{mi} \frac{1}{v_{mi}^2(x)} U_{mil_1}(x) U_{mil_2}(x)\}_{i=1}^M.$$

Note that from (9.11), $D_{l_1 l_2}(x) \geq 0$ for all l_1, and l_2, and $D_{12} = D_{21}$.

9.3 Conventional Local Impulse Response

In this section, we briefly review conventional spatial resolution analysis before we analyze DE CT case. We consider a conventional penalized weighted least-squares (PWLS) cost function of the following form:

$$\hat{x} = \arg\min_x \|y - Ax\|_{W^{1/2}}^2 + \beta R(x), \tag{9.13}$$

where A denotes a $M \times N$ system matrix, $W = \text{diag}\{w_i\}$ denotes the inverse of $M \times M$ covariance matrix of y and $R(x) = \frac{1}{2} x' \mathbb{R} x$ denotes quadratic regularization, and $\mathbb{R} = C'C$ denotes the Hessian matrix of the regularizer. According to [15], the local response of the conventional PWLS cost function is expressed:

$$l^{(j)} = [F + \beta \mathbb{R}]^{-1} F e^{(j)}, \tag{9.14}$$

where $F = A'WA$ is the Fisher information matrix and C denotes a $4N \times N$ differencing matrix. Now following [15], consider the Fisher information approximation:

$$F = A'WA = A'\text{diag}\{w_j\}A \approx \text{diag}\{\kappa_j\} A'A \text{diag}\{\kappa_j\}, \tag{9.15}$$

where we define the following kappa factors

$$\kappa_j = \sqrt{\sum_i g_{ij}^2 w_i / \sum_i g_{ij}^2}. \tag{9.16}$$

Substituting (9.15) into (9.14) and simplifying yields following conventional local impulse response approximation:

$$\begin{aligned} l^{(j)} &\approx [\mathrm{diag}\{\kappa_j\}A'A\mathrm{diag}\{\kappa_j\} + \beta\mathbb{R}]^{-1}(\mathrm{diag}\{\kappa_j\}A'A\mathrm{diag}\{\kappa_j\})e^{(j)} \\ &= \mathrm{diag}\{\frac{1}{\kappa_j}\}[A'A + \mathrm{diag}\{\frac{1}{\kappa_j}\}\mathbb{R}\mathrm{diag}\{\frac{1}{\kappa_j}\}]^{-1}A'A\kappa_j e^{(j)} \\ &\approx [A'A + \mathrm{diag}\{\frac{1}{\kappa_j^2}\}\mathbb{R}]^{-1}A'Ae^{(j)}. \end{aligned}$$

The final approximation suggests that the local impulse response depends on a local regularization parameter that is scaled by κ_j^2. This causes nonuniform spatial resolution [15]. To pursue uniform spatial resolution, several modified regularization methods have been proposed. One of the simplest approach is the following modified quadratic roughness penalty function:

$$R^*(x) = \beta \sum_{j=1}^{N} \sum_{i\in\mathcal{N}_j} \psi(\kappa_j x_j - \kappa_i x_i), \tag{9.17}$$

where $\psi(t) = \frac{t^2}{2}$, and $\mathcal{N}$ denotes the neighborhood of the jth pixel. This modified penalty yields approximately uniform spatial resolution at each pixel:

$$\begin{aligned} l^{(j)} &\approx [A'A + \mathrm{diag}\{\frac{1}{\kappa_j}\}\mathbb{R}^*\mathrm{diag}\{\frac{1}{\kappa_j}\}]^{-1}A'Ae^{(j)} \\ &= [A'A + \mathbb{R}]^{-1}A'Ae^{(j)}, \end{aligned} \tag{9.18}$$

where $\mathbb{R}^* = \mathrm{diag}\{\kappa_j\}\mathbb{R}\mathrm{diag}\{\kappa_j\}$ denotes the Hessian matrix of the modified regularizer $R^*(x)$. We believe that a roughness penalty function should be zero if the input image is perfectly uniform. However, the roughness penalty function in (9.17) is not zero when x is uniform. Therefore, [15] suggested following modified regularizer:

$$R^*(x) = \beta \sum_{j=1}^{N} \sum_{i\in\mathcal{N}_j} \psi(\kappa_j x_j - \kappa_i x_i) \approx \beta \sum_{j=1}^{N} \sum_{i\in\mathcal{N}_j} \psi(\sqrt{\kappa_j\kappa_i}(x_j - x_i)) \tag{9.19}$$

$$= \beta \sum_{j=1}^{N} \sum_{i\in\mathcal{N}_j} \kappa_j\kappa_i\psi(x_j - x_i), \tag{9.20}$$

where $\psi(t) = \frac{t^2}{2}$. It is reasonable approach because if the ith pixel and jth pixel are close to each other then $\kappa_i \approx \kappa_j$. The next sections extend this analysis of the local impulse response and design of modified roughness penalty functions to Dual-Energy CT.

9.4 Fisher Information Approximation for DE CT

This section focuses on pursuing uniform spatial resolution *e.g.*, [11,59,60] by considering an approximation of the Fisher information matrix in DE CT. The $2N \times 2N$ Fisher information simplifies as follows:

$$F(x) = \begin{pmatrix} F_{11}(x) & F_{12}(x) \\ F_{12}(x) & F_{22}(x) \end{pmatrix} = G_2' \cdot D(x) \cdot G_2 \approx K'(x) \cdot G_2' \cdot G_2 \cdot K(x), \tag{9.21}$$

where K is a $2N \times 2N$ block diagonal matrix of the kappa factors:

$$K(x) = \begin{pmatrix} K_{11}(x) & K_{12}(x) \\ K_{21}(x) & K_{22}(x) \end{pmatrix}, \tag{9.22}$$

$$K_{l_1 l_2} = \operatorname{diag}\{\kappa_{l_1 l_2 j}\}_{j=1}^{N}.$$

Note that

$$K' G_2' G_2 K = \begin{pmatrix} K_{11} & K_{21} \\ K_{12} & K_{22} \end{pmatrix} \begin{pmatrix} G'G & 0 \\ 0 & G'G \end{pmatrix} \begin{pmatrix} K_{11} & K_{12} \\ K_{21} & K_{22} \end{pmatrix} \tag{9.23}$$

$$= \begin{pmatrix} K_{11}G'GK_{11} + K_{21}G'GK_{21} & K_{11}G'GK_{12} + K_{21}G'GK_{22} \\ K_{12}G'GK_{11} + K_{22}G'GK_{21} & K_{12}G'GK_{12} + K_{22}G'GK_{22} \end{pmatrix}. \tag{9.24}$$

Usually, the largest elements of $F_{l_1 l_2}$ are located along its diagonal due to the $1/r$ response of 2D tomographic imaging. Therefore, we would like the approximation in (9.21) to be exact along its block diagonal elements. One way we can achieve this is by satisfying only

these three conditions:

$$[F_{11}(\check{x})]_{jj} = \sum_m \sum_i g_{ij}^2 w_{mi} \frac{U_{mi1}^2(\check{x})}{v_{mi}^2(\check{x})} \approx (\kappa_{11j}^2 + \kappa_{21j}^2) \sum_i g_{ij}^2, \tag{9.25}$$

$$[F_{22}(\check{x})]_{jj} = \sum_m \sum_i g_{ij}^2 w_{mi} \frac{U_{mi2}^2(\check{x})}{v_{mi}^2(\check{x})} \approx (\kappa_{12j}^2 + \kappa_{22j}^2) \sum_i g_{ij}^2, \tag{9.26}$$

$$[F_{12}(\check{x})]_{jj} = [F_{21}(\check{x})]_{jj} = \sum_m \sum_i g_{ij}^2 w_{mi} \frac{U_{mi1}(\check{x}) \cdot U_{mi2}(\check{x})}{v_{mi}^2(\check{x})} \tag{9.27}$$

$$\approx (\kappa_{11j}\kappa_{12j} + \kappa_{21j}\kappa_{22j}) \sum_i g_{ij}^2.$$

Of course there are many different possible methods but we consider two simple methods for designing the K values: $K_{12} = 0$, and $K_{21} = 0$. If we choose the constraint $K_{12} = 0$, conditions in (9.25), (9.26), and (9.27) simplify as follows:

$$[F_{11}(\check{x})]_{jj} = \sum_m \sum_i g_{ij}^2 w_{mi} \frac{U_{mi1}^2(\check{x})}{v_{mi}^2(\check{x})} \approx (\kappa_{11j}^2 + \kappa_{21j}^2) \sum_i g_{ij}^2,$$

$$[F_{22}(\check{x})]_{jj} = \sum_m \sum_i g_{ij}^2 w_{mi} \frac{U_{mi2}^2(\check{x})}{v_{mi}^2(\check{x})} \approx \kappa_{22j}^2 \sum_i g_{ij}^2,$$

$$[F_{12}(\check{x})]_{jj} = [F_{21}(\check{x})]_{jj} = \sum_m \sum_i g_{ij}^2 w_{mi} \frac{U_{mi1}(\check{x}) \cdot U_{mi2}(\check{x})}{v_{mi}^2(\check{x})} \approx \kappa_{21j}\kappa_{22j} \sum_i g_{ij}^2.$$

Therefore, we can solve for the kappa factors:

$$K(x) = \begin{pmatrix} K_{11}(x) & 0 \\ K_{21}(x) & K_{22}(x) \end{pmatrix}, \qquad \kappa_{4j} \approx \sqrt{[F_{22}(\check{x})]_{jj} / \sum_i g_{ij}^2},$$

$$\kappa_{3j} \approx \sqrt{[F_{12}(\check{x})]_{jj} / (\sum_i g_{ij}^2 \cdot \kappa_{22j})}, \qquad \kappa_{1j} \approx \sqrt{[F_{11}(\check{x})]_{jj} / \sum_i g_{ij}^2 - \kappa_{21j}^2}.$$

Similarly, if we choose the constraint $K_{21} = 0$, we can solve for the kappa factors:

$$K(x) = \begin{pmatrix} K_{11}(x) & K_{12}(x) \\ 0 & K_{22}(x) \end{pmatrix}, \qquad \kappa_{1j} \approx \sqrt{[F_{11}(\check{x})]_{jj} / \sum_i g_{ij}^2},$$

$$\kappa_{2j} \approx \sqrt{[F_{12}(\check{x})]_{jj} / (\sum_i g_{ij}^2 \cdot \kappa_{11j})}, \qquad \kappa_{4j} \approx \sqrt{[F_{22}(\check{x})]_{jj} / \sum_i g_{ij}^2 - \kappa_{12j}^2}.$$

Fig. 9.1 shows an example of kappa factors for the constraints $K_{12} = 0$.

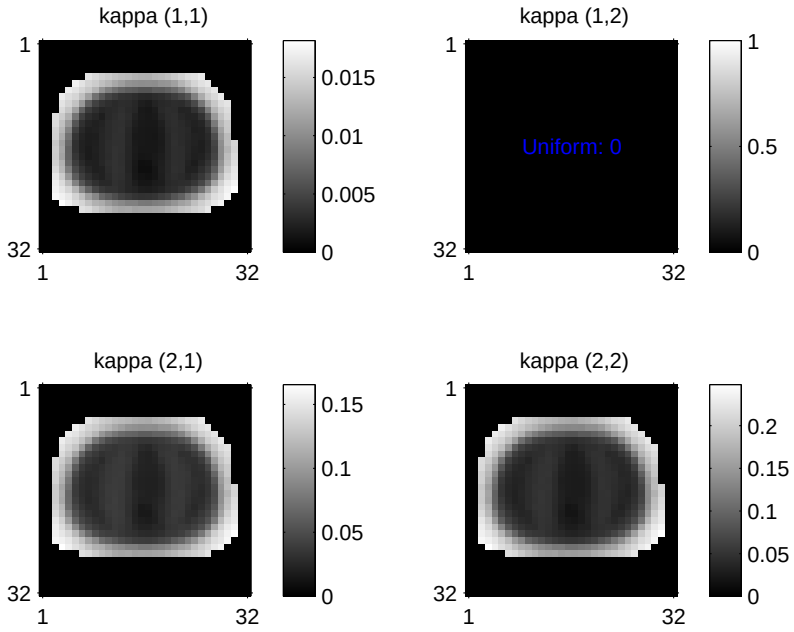

Fig. 9.1: An example of kappa factors that could be used for regularization in 2D DE CT.

9.5 Roughness penalty design

Based on (9.21), we propose the following modified roughness penalty:

$$R(x) = \sum_{m=1}^{2} \sum_{j} \sum_{i \in \mathcal{N}_j} w_{ij} \psi_j \Big(\sum_{l=1}^{2} ([K_{ml}]_j x_{lj} - [K_{ml}]_i x_{li}) \Big) = \underline{d}' \psi(CKx), \tag{9.28}$$

where w_{ij} (= 1 or $\sqrt{2}$) denotes the distance between jth voxel and ith voxel: $\underline{d} = [d_{C_1} d_{C_2} d_{C_3} d_{C_4}]' \otimes \underline{1}_{2N}$, d_{C_n} denotes nth neighbor offset's distance. Usually, we use 4 different neighbor offsets so $d_{C_1} = d_{C_3} = \sqrt{2}$ for diagonal neighbors and $d_{C_2} = d_{C_4} = 1$ for horizontal and vertical neighbors. Here, the $8N \times 2N$ matrix C and $2N \times 2N$ matrix K are

defined as:

$$C = \begin{pmatrix} \tilde{C}_1 \\ \tilde{C}_2 \\ \tilde{C}_3 \\ \tilde{C}_4 \end{pmatrix}, \tilde{C}_t = \begin{pmatrix} C_t & 0 \\ 0 & C_t \end{pmatrix}, K = \begin{pmatrix} K_{11} & K_{12} \\ K_{21} & K_{22} \end{pmatrix}, \tag{9.29}$$

where C_t denotes a $N \times N$ differencing matrix for tth offset. As discussed in section 9.3, we prefer to modify the roughness penalty function so that it is zero for a uniform input images. To acheive this goal, we define the $8N \times 8N$ matrix $\tilde{K}$ such that

$$CK \approx \tilde{K}C. \tag{9.30}$$

In particular:

$$CK = \begin{pmatrix} C_1 & 0 \\ 0 & C_1 \\ C_2 & 0 \\ 0 & C_2 \\ C_3 & 0 \\ 0 & C_3 \\ C_4 & 0 \\ 0 & C_4 \end{pmatrix} \begin{pmatrix} K_{11} & K_{12} \\ K_{21} & K_{22} \end{pmatrix} = \begin{pmatrix} C_1K_{11} & C_1K_{12} \\ C_1K_{21} & C_1K_{22} \\ C_2K_{11} & C_2K_{12} \\ C_2K_{21} & C_2K_{22} \\ C_3K_{11} & C_3K_{12} \\ C_3K_{21} & C_3K_{22} \\ C_4K_{11} & C_4K_{12} \\ C_4K_{21} & C_4K_{22} \end{pmatrix} \approx \begin{pmatrix} \tilde{K}_{11}^{(1)}C_1 + \tilde{K}_{12}^{(1)}C_1 \\ \tilde{K}_{21}^{(1)}C_1 + \tilde{K}_{22}^{(1)}C_1 \\ \tilde{K}_{11}^{(2)}C_2 + \tilde{K}_{12}^{(2)}C_2 \\ \tilde{K}_{21}^{(2)}C_2 + \tilde{K}_{22}^{(2)}C_2 \\ \tilde{K}_{11}^{(3)}C_3 + \tilde{K}_{12}^{(3)}C_3 \\ \tilde{K}_{21}^{(3)}C_3 + \tilde{K}_{22}^{(3)}C_3 \\ \tilde{K}_{11}^{(4)}C_4 + \tilde{K}_{12}^{(4)}C_4 \\ \tilde{K}_{21}^{(4)}C_4 + \tilde{K}_{22}^{(4)}C_4 \end{pmatrix} = \tilde{K}C, \tag{9.31}$$

where $\tilde{K} = \text{diag}\{\tilde{K}^{(t)}\}_{n=1}^{4}$ denotes a $8N \times 8N$ block diagonal matrix, $\tilde{K}^{(t)} = \begin{pmatrix} \tilde{K}_{11}^{(t)} & \tilde{K}_{12}^{(t)} \\ \tilde{K}_{21}^{(t)} & \tilde{K}_{22}^{(t)} \end{pmatrix}$, and $\tilde{K}_{lm}^{(t)}$ denotes a $N \times N$ diagonal matrix with elements $[\tilde{K}_{lm}^{(t)}]_{ij} = \sqrt{[K_{lm}]_{ij}[\text{S}(K_{lm},t)]_{ij}}$, $j = 1,\ldots,N$. Here, $\text{S}(A,n)$ denotes the A matrix shifted by tth offset, for $t = 1,\ldots,4$. Therefore, we modified the roughness penalty function (9.28) as follows:

$$R(x) = \underline{d}'\psi(CKx) \approx \underline{d}'\psi(\tilde{K}Cx) = \underline{d}'\psi(T_1T_2Cx), \tag{9.32}$$

where

$$T_1 = \text{diag}\{T_1^{(t)}\}_{t=1}^4, T_1^{(t)} = \begin{pmatrix} \tilde{K}_{11}^{(t)} & 0 \\ 0 & \tilde{K}_{22}^{(t)} \end{pmatrix} \tag{9.33}$$

$$T_2 = \text{diag}\{T_2^{(t)}\}_{t=1}^4, T_2^{(t)} = \begin{pmatrix} \mathbf{1} & \frac{\tilde{K}_{12}^{(t)}}{\tilde{K}_{11}^{(t)}} \\ \frac{\tilde{K}_{21}^{(t)}}{\tilde{K}_{22}^{(t)}} & \mathbf{1} \end{pmatrix}, \tag{9.34}$$

where T_1 and T_2 each denote $8N \times 8N$ matrixes, and $\tilde{K}_{l_1 l_2}$ denotes a $N \times N$ diagonal matrix for all l_1 and l_2. Note that T_1 is diagonal matrix, and our potential function ψ is similar to quadratic function near zero. If ψ is quadratic regularizer,

$$R(x) = x'C'T_2'T_1'\text{diag}\{\underline{d}\}T_1T_2Cx \tag{9.35}$$

$$= X'C'T_2'\text{diag}\{\tilde{\underline{d}}\}T_2Cx, \tag{9.36}$$

where $\tilde{\underline{d}} = T_1^2\underline{d}$ because T_1 is diagonal matrix. Therefore, we further modify the roughness penalty function $\tilde{R}(x)$ in (9.34) as follows:

$$\tilde{R}(x) \triangleq \underline{d}'T_1^2\psi(T_2Cx) = \sum_k \tilde{d}_k \psi_k(\underline{\tilde{c}}_k'x), \tag{9.37}$$

where, $\underline{\tilde{c}}_k'$ is defined kth row of the matrix $\tilde{C} = T_2C$, and $\tilde{d}_k = d_k \cdot [T_1^2]_{kk}$. Therefore,

$$\nabla\tilde{R}(x) = \sum_k \tilde{d}_k \nabla\psi_k(\underline{\tilde{c}}_k'x) = \sum_k \underline{\tilde{c}}_k\tilde{d}_k\dot{\psi}_k([\tilde{C}x]_k) = \sum_k \tilde{d}_k\underline{\tilde{c}}_k w_k([\tilde{C}x]_k)[\tilde{C}x]_k = \tilde{C}'\tilde{D}_1\tilde{C}x, \tag{9.38}$$

$$\nabla^{(2)}\tilde{R}(x) = \sum_k \tilde{d}_k \nabla^{(2)}\psi_k(\underline{\tilde{c}}_k'x) = \sum_k \tilde{d}_k\underline{\tilde{c}}_k\ddot{\psi}_k([\tilde{C}x]_k)\underline{\tilde{c}}_k' = \tilde{C}'\tilde{D}_2\tilde{C}. \tag{9.39}$$

where $\tilde{D}_1 = \text{diag}\{\tilde{d}_k w_k([\tilde{C}x]_k)\}$, $\tilde{D}_2 = \text{diag}\{\tilde{d}_k\ddot{\psi}_k([\tilde{C}x]_k)\}$, and the potential weighting function $w_k(t) \triangleq \frac{\dot{\psi}_k(t)}{t}$. If we choose ψ to be a hyperbola, then $w(t) = (1 + (\frac{t}{\delta})^2)^{-\frac{1}{2}}$, and $\ddot{\psi}(t) = (1 + (\frac{t}{\delta})^2)^{-\frac{3}{2}}$. Note that the matrix T_1 and T_2 depend on the object x so we need to update these matrix after iterating a while or to carefully choose the initial value in the iterative algorithm.

9.6 Cross Talk Problem

In previous sections, we analyzed kappa factors and roughness penalty design for DE CT. This section focuses on analyzing the cross talk problem with a simple quadratic regularizer $R(x)$:

$$R(x) = \psi(CKx) = \frac{1}{2}x'K'C'CKx. \tag{9.40}$$

Substituting kappa factors (9.21) and $\mathbb{R}^* = \nabla^{(2)}R(x) = K'C'CK$ into (9.10), we can derive the local impulse response:

$$\begin{aligned} l_l^{(j)} &\approx [F + \mathbb{R}^*]^{-1} F(x) e_l^{(j)} \\ &= [K'G_2'G_2K + K'C'CK]^{-1} K'G_2'G_2Ke_l^{(j)} \\ &= K^{-1}[G_2'G_2 + C'C]^{-1} G_2'G_2Ke_l^{(j)} \\ &= K^{-1}B_2Ke_l^{(j)}. \end{aligned} \tag{9.41}$$

where $B_2 = \begin{pmatrix} B & 0 \\ 0 & B \end{pmatrix} = [G_2'G_2 + C'C]^{-1}G_2'G_2$, $B = [G'G + \sum_{t=1}^{4} C_t'C_t]^{-1}G'G$. When we use kappa factors for which $K_{12} = 0$ as in section 9.4 then,

$$K^{-1} = \begin{pmatrix} K_{11}^{-1} & 0 \\ -K_{21} \cdot (K_{11}K_{22})^{-1} & K_{22}^{-1} \end{pmatrix}. \tag{9.42}$$

Combining (9.41) with (9.42) yields the following expression for the local impulse response:

$$
\begin{aligned}
l_l^{(j)} &\approx K^{-1} B_2 K e_l^{(j)} = K^{-1} \begin{pmatrix} B & 0 \\ 0 & B \end{pmatrix} K e_l^{(j)} \\
&= K^{-1} \begin{pmatrix} B & 0 \\ 0 & B \end{pmatrix} \begin{pmatrix} K_{1l} e^{(j)} \\ K_{2l} e^{(j)} \end{pmatrix} = K^{-1} \begin{pmatrix} K_{1l} B e^{(j)} \\ K_{2l} B e^{(j)} \end{pmatrix} \\
&= \begin{pmatrix} \kappa_{1lj} \cdot K_{11}^{-1} \cdot B \cdot e^{(j)} \\ [\kappa_{2lj} \cdot K_{22}^{-1} - \kappa_{1lj} \cdot \cdot K_{21} \cdot (K_{11} K_{22})^{-1}] \cdot B \cdot e^{(j)} \end{pmatrix}.
\end{aligned}
$$

Note that, $\kappa_{12j} = 0$ for all j. So the local impulse response for $l = 1$ can be expressed as

$$
l_1^{(j)} \approx \begin{pmatrix} \kappa_{11j} \cdot K_{11}^{-1} \cdot B \cdot e^{(j)} \\ [\kappa_{21j} \cdot K_{22}^{-1} - \kappa_{11j} \cdot K_{21} \cdot (K_{11} K_{22})^{-1}] \cdot B \cdot e^{(j)} \end{pmatrix}, \tag{9.43}
$$

and when $l = 2$ can be expressed as

$$
l_2^{(j)} \approx \begin{pmatrix} \kappa_{12j} \cdot K_{11}^{-1}(x) \cdot B \cdot e^{(j)} \\ \kappa_{22j} \cdot K_{22}^{-1}(x) \cdot B \cdot e^{(j)} \end{pmatrix},
$$

Therefore, if we want to solve the cross talk problem, we have to find appropriate kappa factors that satisfy these conditions for all j:

$$
[\kappa_{21j} \cdot K_{22}^{-1} - \kappa_{11j} \cdot K_{21} \cdot (K_{11} K_{22})^{-1}] \cdot B \cdot e^{(j)} = 0 \tag{9.44}
$$

$$
\kappa_{12j} \cdot K_{11}^{-1} \cdot B \cdot e^{(j)} = 0. \tag{9.45}
$$

Equation (9.45) is satisfied because $\kappa_{12j} = 0$ for all j. However, unfortunately we could not find appropriate kappa factors that satisfy equation (9.44). Fig. 9.2 shows examples of local impulse responses with bone mineral impulse, $l = 2$. Even though there only a bone mineral impulse, the local impulse response appeared in both soft tissue and bone minerals material estimates. We tested the local impulse response with or without Fisher

information approximation and roughness penalty design and there were no big difference among these cases.

9.7 Conclusion

In this chapter, we analyzed the spatial resolution properties of PWLS reconstruction for DECT. We tried to reduce the cross talk problem by designing extended roughness penalty function. However, section 9.6 showed that the cross talk problem comes from the statistical model and we were unable to solve it by changing kappa factors in the roughness penalty. Therefore, we considered a new approach that changed the cost function that will be introduced in the next chapter.

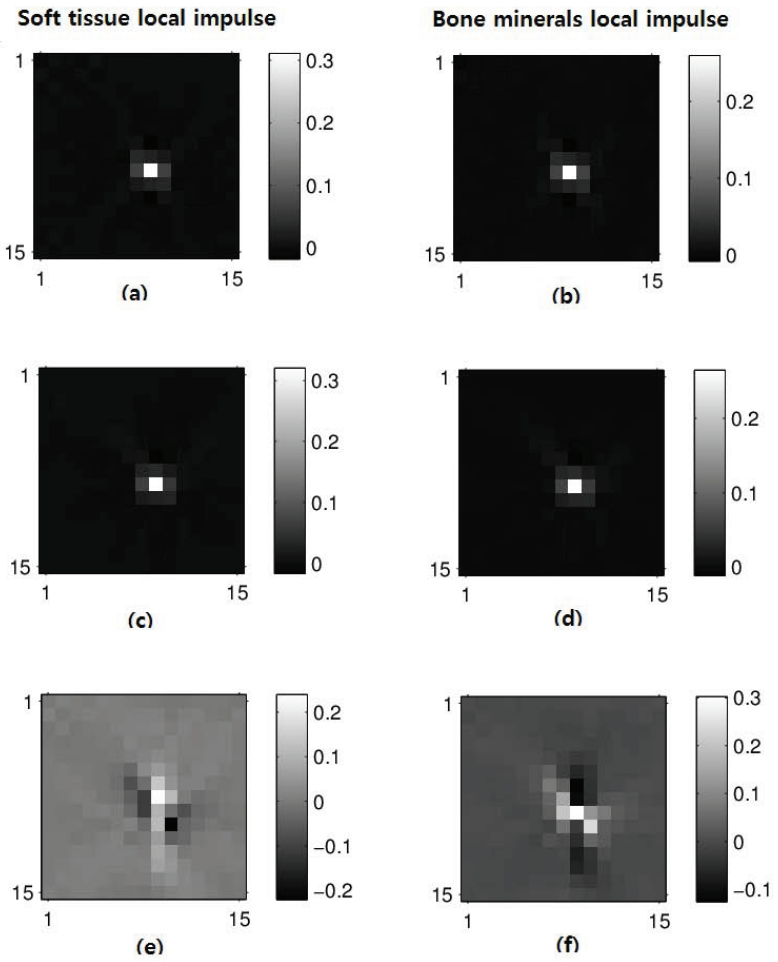

Fig. 9.2: Examples of local impulse responses with bone mineral impulse: (a) Soft tissue local impulse response in (9.43). (b) Bone minerals local impulse response in (9.43). (c) Soft tissue local impulse response with Fisher information approximation in (9.21). (d) Bone minerals local impulse response with Fisher information approximation in (9.21). (e) Soft tissue local impulse response with roughness penalty design in (9.37). (f) Bone minerals local impulse response with roughness penalty design in (9.37).

CHAPTER 10

Iterative image reconstruction for dual-energy X-ray CT using regularized material sinogram estimates

This work is based on [27].

10.1 Introduction

In Chapter 7 and 8, we discussed iterative Dual-Energy CT reconstruction algorithms. These methods estimate the object image or material sinogram based on log sinogram data. However, noise in the estimated log data is a limitation of these methods. Additionally, it is very hard to prevent the cross talk problem; some of the signal of one material appeared in the estimated image of the other material image, when we estimated the object image directly with those approaches. This chapter describes a DE reconstruction method based on statistical models that avoids using a logarithm. We first estimate material sinograms directly from the raw DE data (without any logarithm), with mild regularization to control noise and avoid outliers. We then apply a penalized weighted least squares (PWLS) method to reconstruct images of the two material components from the material sinogram estimates. We also propose a joint edge-preserving regularizer that uses the prior knowledge that the two material images have many region edges located in the same positions. Preliminary simulation results suggest that this iterative method improves image quality

compared to conventional approaches based on log data for low-dose DE CT scans. This section uses the same parameters and models as in section 7.2.

10.2 Dual-Energy Reconstruction

Recently, several iterative methods were presented, such as single energy CT [36], and statistical sinogram restoration for DECT [46], and PWLS DE CT reconstruction from $\hat{f}$ [28]. At each iteration, the DE methods estimate the material images or material sinograms based on $\hat{f}$. However, accuracy of $\hat{f}$ limits these methods; $\hat{f}$ in (7.8) uses the logarithm that is sensitive to noise especially when $y_{mi} - r_{mi}$ is small. In this chapter, we propose a Dual-Energy log-free (DELF) approach that estimates material sinograms from raw CT data directly without using any logarithm. Fig. 10.1 summarizes several possible methods for DE CT reconstruction.

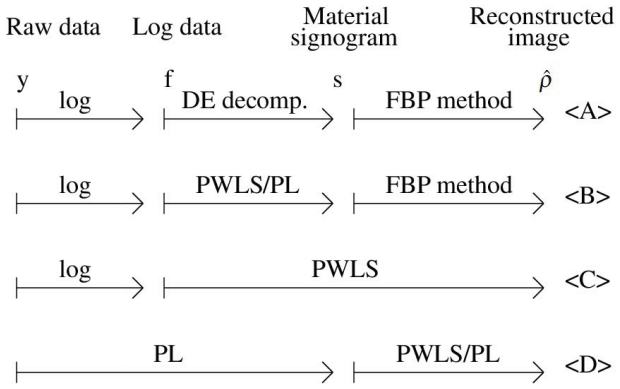

Fig. 10.1: Four different DE CT reconstruct algorithms. <A> conventional method [2], <B> statistical sinogram restoration [46], <C> PWLS DE CT reconstruction from $\hat{f}$ [28], <D> DELF method.

10.2.1 Dual-Energy log-free (DELF) approach

The DELF algorithm consists of two steps: (i) estimating material sinograms $\hat{\mathbf{s}}$ directly from the raw sinograms, y, and (ii) reconstructing the material density ρ from the estimated material sinogram. We use suitable regularization for both steps.

Instead of estimating f by using log function, we propose to estimate the material sinograms, s, from X-ray CT measurement data, y, directly. By including a sinogram-domain roughness penalty R in the cost function, we can also control noise and handle cases where $y_{mi} - r_{mi}$ is negative. Our sinogram domain non convex cost function is defined as:

$$\hat{\mathbf{s}} = \arg\min_{s} \Psi_1(\mathbf{s}), \tag{10.1}$$

$$\begin{aligned} \Psi_1(\mathbf{s}) &\triangleq L(\mathbf{s}) + \beta_1 R(\mathbf{s}) \\ &= \sum_m \sum_i \frac{w_{mi}}{2} |y_{mi} - \bar{y}_{mi}(\mathbf{s})|^2 + \beta_1 R(\mathbf{s}), \end{aligned} \tag{10.2}$$

where $\mathbf{s} \triangleq (\mathbf{s}_1, \ldots, \mathbf{s}_{N_d})$, $\mathbf{s}_i \triangleq (s_{i1}, \ldots, s_{iL_0})$, $\bar{y}_{mi}$ was defined in in (7.2) and in (7.4), and the sinogram weighting is

$$w_{mi} \triangleq \frac{1}{\mathrm{Var}(y_{mi})} \approx \frac{1}{y_{mi}}. \tag{10.3}$$

For sinogram regularization we used roughness penalty:

$$R(s) = \sum_{i=1}^{N_d} \sum_{k \in \mathcal{N}_i} \psi(s_{li} - s_{1k}, s_{2i} - s_{2k}), \tag{10.4}$$

where ψ is a potential function and $\mathcal{N}_i$ is a neighborhood of pixel i and the modified regularizer in [15] is used to provide uniform spatial resolution. For $\mathcal{N}_i$ we used the 8 nearest neighbors of the ith pixel. For ψ we used a modified hyperbola discussed in the next section.

We minimize (10.2) using a conjugate gradient (CG) algorithm with a monotone line search [13].

After estimating the material sinogram $\hat{\mathbf{s}}$, we use it as the data fitting term to estimate

the object ρ by minimizing the following convex cost function:

$$\hat{\rho} = \arg\min_{\rho} \Psi_2(\rho), \tag{10.5}$$

$$\begin{aligned}\Psi_2(\rho) &\triangleq L(\rho) + \beta_2 R(\rho) \\ &= \sum_l \sum_i \frac{\tilde{w}_{il}}{2} |\hat{s}_{il} - s_{il}(\rho)|^2 + \beta_2 R(\rho),\end{aligned} \tag{10.6}$$

where by error propagation (assuming β_1 small):

$$[\mathrm{diag}\{\tilde{w}_{i1}, \ldots, \tilde{w}_{iL_0}\}]^{-1} \tag{10.7}$$

$$\approx \mathrm{Cov}\{\hat{\mathbf{s}}_i\} \approx (\nabla y_i)^{-1} \mathrm{Cov}\{\hat{y}_i\} [(\nabla y_i)^{-1}]' \tag{10.8}$$

$$\approx (\nabla y_i)^{-1} \mathrm{diag}\{Y_{mi}\} [(\nabla y_i)^{-1}]'. \tag{10.9}$$

The regularizer in (10.6) is described in section 10.2.2 below. We minimized the cost function (10.6) using an ordered subsets method [1]. We initialized the iterations using the image estimated by the conventional algorithm in [28] and by using a suitable stopping criteria; the number of iterations did not exceed 200.

10.2.2 Joint edge preserving regularizer

In the previous chapters we used a hyperbolic potential function ψ to preserve edges. However, that penalty function ignores the fact that water and bone material images share many common edges. To improve the accuracy of the algorithm, we should consider both materials' edge positions jointly when we estimate the object. Adapting [19], we investigated the following potential function for the case $L_0 = 2$:

$$\psi(\Delta\rho_1, \Delta\rho_2) = \sqrt{1 + (\frac{\Delta\rho_1}{\delta})^2 + (\frac{\Delta\rho_2}{\eta})^2} - 1 \tag{10.10}$$

and the following roughness penalty function:

$$R(\rho_1,\rho_2) = \sum_j \sum_{i\in\mathcal{N}_j} \psi(\rho_{1j}-\rho_{1i},\rho_{2j}-\rho_{2i})$$
$$= \sum_j \sum_{i\in\mathcal{N}_j} \sqrt{1+\left(\frac{\rho_{1j}-\rho_{1i}}{\delta}\right)^2+\left(\frac{\rho_{2j}-\rho_{2i}}{\eta}\right)^2},$$

where $\mathcal{N}_j$ denotes the neighborhood of pixel j. We need set the values of δ and η differently due to the differences of the two material images; roughly we want $\delta^2 \propto \mathrm{Var}(\hat{\rho}_{1j})$ and $\eta^2 \propto \mathrm{Var}(\hat{\rho}_{2j})$ to preserve edges while suppressing noise.

10.3 Results

We applied the DELF method to simulated DE CT scans and to real phantom DE CT scans. In both cases, the phantom consists of six different materials: fat, bolus, organs, muscle, inner-bone, and white-bone. This phantom was scanned with low dose, 150mAs (150mA*1sec), with source voltages 80kVp and 140kVp and the slice thickness was 1.25mm. For this data, the standard GE proprietary scatter correction was already applied to sinograms, so we used $r_{mi} = 0$ in (7.2). The fan-beam projection space was 888 radial samples $\times$ 984 angular views over 360° degrees and we used X-ray spectra model provided by GE CATSIM software [9], including the effects of a standard large bow-tie filter. For simulated data in the next section, we used the same X-ray spectra model, filter, and other parameters of the phantom data. However, there were only two materials, soft tissues and bone minerals, for simulated data.

10.3.1 Simulated result

We simulated DE CT scans to evaluate the feasibility of the DELF method for image reconstruction. The reconstructed images were 128×128 for the simulated DE CT scans with 0.4 $\times$ 0.4 cm^2 pixel size and field of view was 50cm $\times$ 50cm. We applied the

conventional dual-energy FBP reconstruction method, DE CT reconstruction algorithm in [28], and DELF method. We investigated 10 different X-ray source intensities ($I_{mi} = I_0$), from 1×10^4 to 1×10^5 photons per ray. We assumed $r_{mi} = 0$ in (7.2), *i.e.*, no scatter was simulated.

Fig. 10.2 illustrates estimated material sinograms based on the conventional logarithm approach <A> and the DELF method <D> in Fig. 10.1. The DELF method has reduced noise and outliers, particularly in the photon starved regions of the sinogram, because of the regularizer in (10.2).

Fig. 10.3 shows that the DELF method reduces significantly the NRMSE of the material sinogram estimates compared to the conventional sinogram estimation <A> based on log function. For the DELF method, we chose $\log_2 \beta_1 = -4$, $\log_2 \beta_2 = -10.2$ and $\delta = 0.1(g/cm^3)$ and $\eta = 0.2(g/cm^3)$ empirically. It is difficult to assess error in the sinogram domain, so we now turn to the image domain.

Fig. 10.4 shows the density maps of the material components: soft tissues and bone mineral and the estimated object of the three methods with $I_0 = I_{mi} = 2 \cdot 10^4$. Fig. 10.4(a)-(b) shows the simulated two component images. Fig. 10.4(c)-(d) shows FBP method images <A>, whereas Fig. 10.4(e)-(f) shows the previous iterative method <B> images. The previous iterative method succeeded in reducing streak artifacts compared to the FBP images. However, the previous method image contains many outlier voxels whose magnitudes are larger than 5 g/cm^3 even though the bone density is at most 2 here. In contrast, the DELF method, in Fig. 10.4(g)-(h), has reduced streaks and yields lower noise than other two methods. Plus, its voxels have more reasonable density values for all spatial locations than the conventional approaches.

Fig. 10.5 shows the RMSE plot of the reconstructed object images with different incident intensities, I_0. We observed that the DELF method significantly reduces the RMSE

of soft tissue and bone minerals estimates compared to the other methods.

10.3.2 Phantom Result

In this section, we applied DELF method to DE CT scans of a phantom. The reconstructed images were 512×512 for the phantom DE CT scans with 0.1×0.1 cm^2 pixel size and field of view was 50cm $\times$ 50cm. We separated the phantom scans into soft tissues (organ) and bone minerals (white-bone) sinograms. Fig. 10.6 illustrates estimated material sinograms based on the conventional method, the previous approach and the DELF approach. The DELF method has reduced noise and outliers in the soft tissue sinogram. However, the estimated bone minerlas sinograms of two approaches are similarly noisy and it is hard to find difference between them. Fig. 10.7 shows the estimated density maps of soft tissue and bone minerals. In the previous section, DELF method successfully reduced noise and streaks with the simulated data. However, with the phantom data, there is no significant difference among FBP method <A>, previous method <B>, and DELF method <D>. The DELF method succeeded in reducing streak artifacts in the estimated soft tissue image compared to the FBP reconstructed images but it was too blurred. Plus, some of soft tissues appears in the estimated bone minerals.

There are three major reasons why DE CT phantom scans were not decomposed successfully by the DELF method. First, there may be a mismatch in the spectrum model that is provided by the GE CATSIM software. Second, for these results, we assumed additive background contributions $r_{mi} = 0$, which assumes scatter was perfectly corrected. However, scatter correction might be imperfect. Note that this study used narrow collimation (1.25 mm at isocenter) so one would expect the scatter contribution to be small. Third, the object contains six distinct materials, but we tried to model six components mixture with only two mass-attenuation coefficient basis functions. We choose mass-attenuation

coefficient of organ and white-bone as our basis materials but they cannot represent all six materials perfectly. We discuss this aspect further in the next section.

10.3.3 Simulations using multiple object materials

As we discussed above there are at least three possible reasons for the unsuccessful decomposition of the DE CT phantom scans. In this section, we show through simulations that the object model mismatch most likely does not play a major role in the unsuccessful decomposition. We generated simulated DE CT data based on the phantom data in section 10.3.2. Simulated data used the same parameters of the phantom data and simulated density maps of soft tissues and bone minerals were also similar to the reconstructed images in Fig. 10.7. The data has no spectrum mismatch and no scatter is simulated. For reconstruction, we need to separate the object, which consists of six different materials, into two mass-attenuation coefficient basis functions. Naturally, we would like to choose the two basis functions that are able to best represent the six materials. Table 10.1 shows

	fat	muscle	organs	bolus	inner bone	white bone
Density (g/cc)	0.955	1.065	1.015	1.005	1.115	1.41
H	8.38	8.51	8.05	8.16	7.23	5.82
C	67.66	67.12	65.23	66.03	59.68	51.86
N	2.11	2.01	2.05	2.08	1.85	1.82
O	21.78	20.34	22.83	22.47	25.42	27.89
Cl	0.07	0.07	0.07	0.07	0.06	0.06
Ca	0	1.95	1.77	1.19	5.76	12.55

Table 10.1: Elemental composition of materials $(\%)$

the elemental compositions and mass densities of the six materials. Note that Bolus refers to the material between organs. Fig. 10.8 shows the six basis materials' energy dependent mass-attenuation coefficient. As we can see, the plots corresponding to Fat, Organ, Muscle, and Bolus are clustered together whereas the White-bone is well-separated from the others. Therefore, out of the $\binom{6}{2}$ candidate pairs, in the following simulation, we only

consider Fat and White-bone, Organ and White-bone, and Muscle and White-bone pairs. We did not consider bolus as one of the candidates because it is less informative than other materials in medical imaging. For each of these pairs we computed the weighted least square fitted density coefficients, where the cost function is given as follows:

$$(\hat{\rho}_1, \hat{\rho}_2) = \underset{\rho_1,\rho_2}{\arg\min} \int I(\mathscr{E})(\mu(\mathscr{E}) - \beta_1(\mathscr{E})\rho_1 - \beta_2(\mathscr{E})\rho_2)^2 \, \mathrm{d}\mathscr{E}, \tag{10.11}$$

where $\hat{\rho}_l$ denotes lth weighted least square fitted density coefficient, β_l denotes lth basis materials' energy-dependent mass-attenuation coefficient, and we used the same notations in the 7.6 and 6.3. We expect that if we choose good basis materials, then the weighted least square fitted density coefficients are close to 1 or 0. Table 10.2 - 10.4 show the weighted least square fitted density coefficients for several possible pairs of basis materials. Unfortunately, it was impossible to separate inner-bone perfectly because inner-bone has both fat and bone minerals. If we were to choose fat and white-bone as our basis materials, then more than 15% of the organs and muscle density can appear in the bone minerals density maps. However, when we choose organ and white-bone as our basis, according to Table 10.3, we can expect reasonable results.

	Basis	Fat	Organ	Muscle	Bolus	Inner-bone	White-bone
$\beta_1(\mathscr{E})$	Fat	1.0000	0.8567	0.8586	0.9049	0.5394	0.0000
$\beta_2(\mathscr{E})$	White-bone	-0.0000	0.1478	0.1417	0.0952	0.4608	1.0000

Table 10.2: Weighted least square fitted density coefficients with Fat and White-bone basis.

	Basis	Fat	Organ	Muscle	Bolus	Inner-bone	White-bone
$\beta_1(\mathscr{E})$	Organ	1.1672	1.0000	1.0022	1.0563	0.6296	0.0000
$\beta_2(\mathscr{E})$	White-bone	-0.1725	0.0000	-0.0065	-0.0609	0.3678	1.0000

Table 10.3: Weighted least square fitted density coefficients with Organ and White-bone basis.

In these tables, negative values indicate that negative coefficients gave the best linear combination of basis materials to fit a given linear attenuation coefficient function.

	Basis	Fat	Organ	Muscle	Bolus	Inner-bone	White-bone
$\beta_1(\mathscr{E})$	Muscle	1.1647	0.9978	1.0000	1.0540	0.6282	0.0000
$\beta_2(\mathscr{E})$	White-bone	-0.1650	0.0065	0.0000	-0.0541	0.3718	1.0000

Table 10.4: Weighted least square fitted density coefficients with Muscle and White-bone basis.

Simulated material sinograms are shown in Fig. 10.9(a) and (d). We applied sinogram restoration approach <B> and DELF method <D> to the simulated data. Fig. 10.9(b) and (e) display method <B>'s resulting component images and Fig. 10.9(c) and (f) show the estimated density maps of DELF method. The DELF approaches have reduced outliers and lower noise than the PWLS method.

Fig. 10.10 (a) and (b) show the density maps of the materials: soft tissues (sum of fat, organ, muscle, and bolus images), and bone minerals (sum of inner-bone and white-bone). Fig. 10.10 (c)-(h) compare the estimated organ and white-bone materials produced by the three methods. As shown in Fig. 10.10 (c)-(f), the results of method <A> and method <B> are very noisy. However, the estimated density maps of the DELF method, shown in Fig. 10.10 (g) and (h), are improved as shown in Table 10.5. The DELF method recon-

	FBP method	PWLS method	DELF method
Soft tissue	0.0210	0.0198	0.0167
Bone minerals	0.0156	0.0149	0.0114

Table 10.5: RMSE of estimated material density maps of three method.

structed the simulated data by using organ and white-bone materials as our basis materials and it yielded much less biased estimated density maps. Therefore, the only remaining reason for the cross talk problem is having used too simplified background model and we believe that we need to estimate background contributions, especially scatters, when the size of phantom is big enough.

10.4 Conclusion

We presented a new iterative approach for DE CT reconstruction. Unlike other DE CT algorithms, the DELF method first estimates material component sinograms directly from X-ray DE CT sinograms without using a logarithm. Preliminary simulation results show that the DELF method estimates material sinograms more precisely than the conventional logarithm method. The improved sinograms yield images with lower RMS error than the PWLS approach in Fig. 10.5. However, the DELF method does not work well with the phantom data because of mismatches in the models such as imperfect scatter and spectral model mismatch. To reconstruct real data, we need to investigate improved models that consider the effect of scatter and other possible errors.

10.5 Acknowledgement

We thank Prof. Goodsitt Mitchell for collecting the realistic CT data used in this chapter.

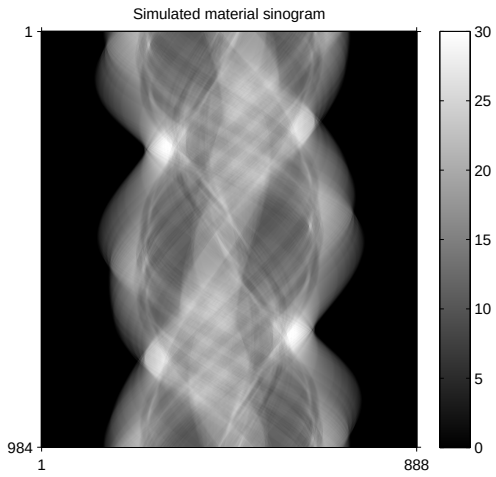

(a) Soft tissues

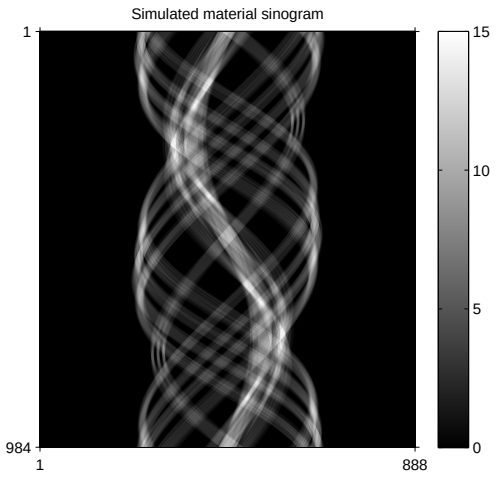

(b) Bone minerals

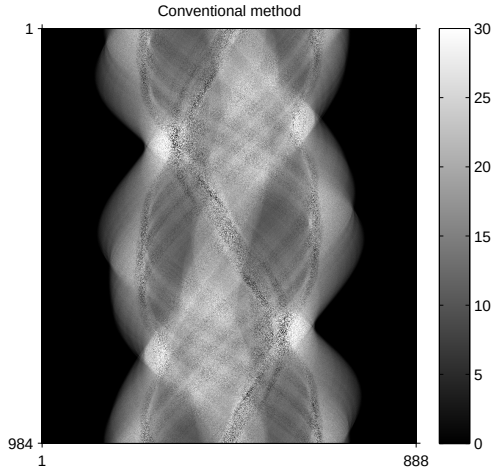

(c) Soft tissues

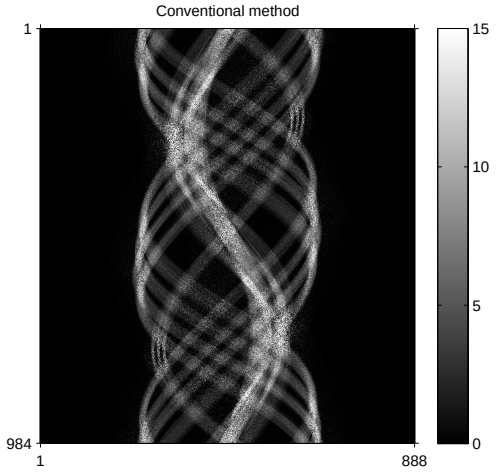

(d) Bone minerals

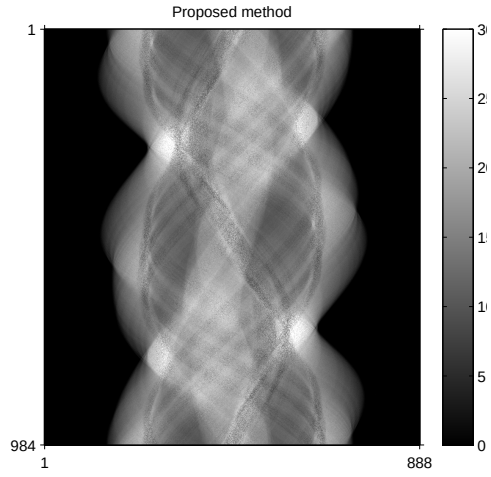

(e) Soft tissues

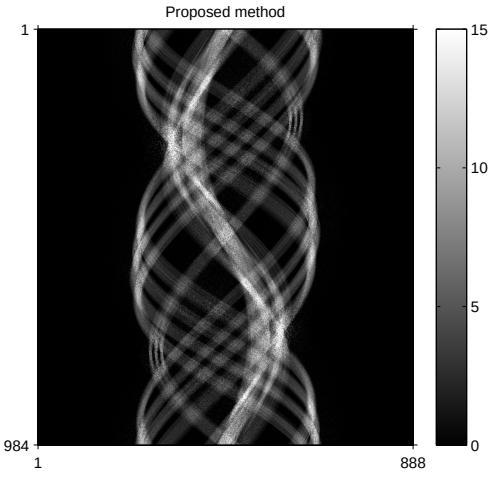

(f) Bone minerals

Fig. 10.2: First row: simulated material sinograms. Second row: previous method <A> sinogram estimates with $I_0 = 2 \cdot 10^4$. Third row: DELF method <D> sinogram estimates with $I_0 = 2 \cdot 10^4$.

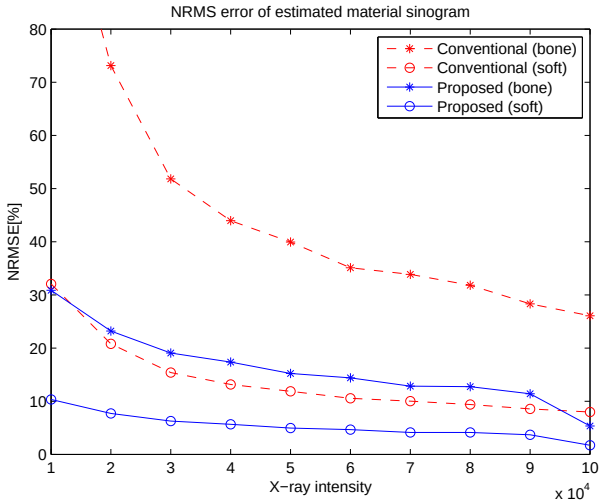

Fig. 10.3: NRMSE of estimated material sinograms: previous method <A>, and the DELF method <D>, versus I_0 (number of incident X-ray photons per ray).

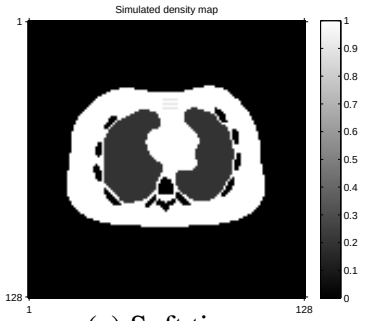

(a) Soft tissues

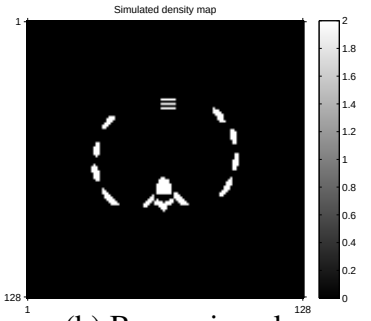

(b) Bone minerals

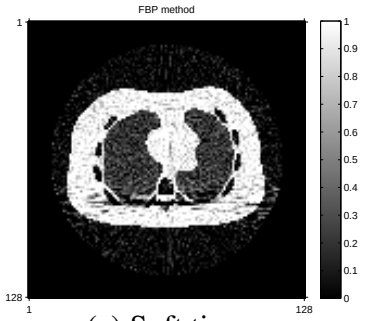

(c) Soft tissues

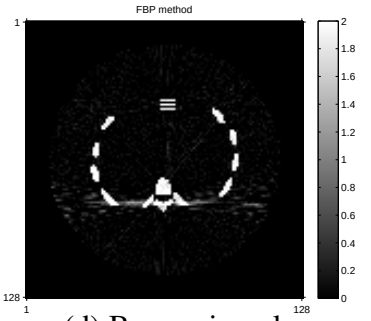

(d) Bone minerals

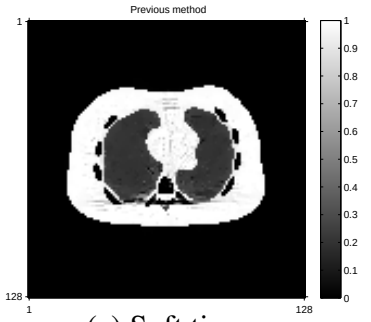

(e) Soft tissues

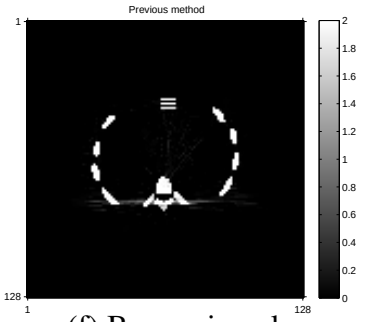

(f) Bone minerals

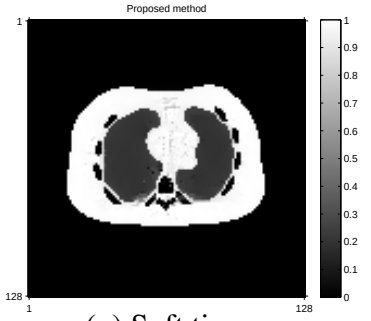

(g) Soft tissues

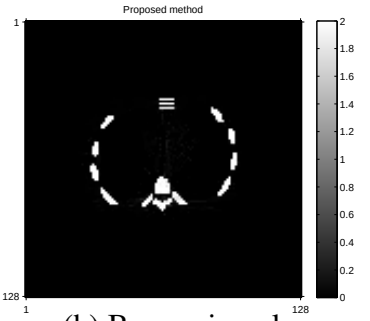

(h) Bone minerals

Fig. 10.4: First row: Two component simulated densities. Second row: FBP method <A> with $I_0 = 2 \cdot 10^4$. Third row: previous method <B> with $I_0 = 2 \cdot 10^4$. Fourth row: DELF method <D> with $I_0 = 2 \cdot 10^4$.

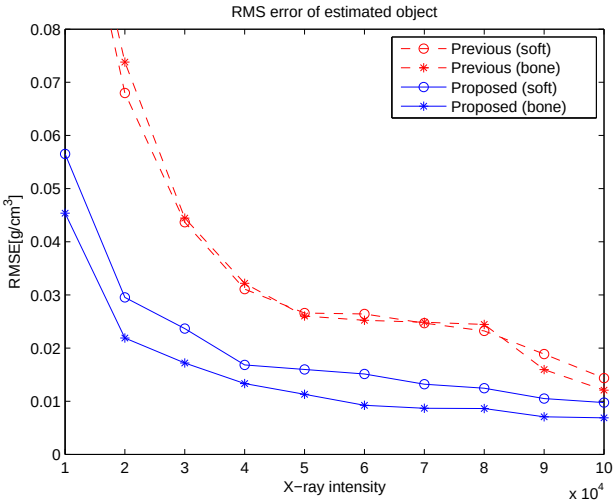

Fig. 10.5: RMSE of reconstructed material density images: previous method <B>, and the DELF method <D>, versus I_0 (number of incident X-ray photons per ray).

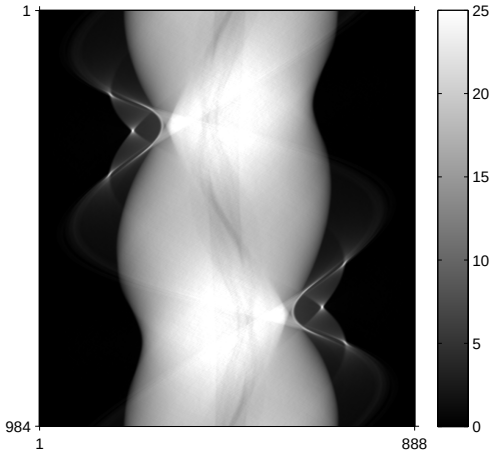

(a) Soft tissue

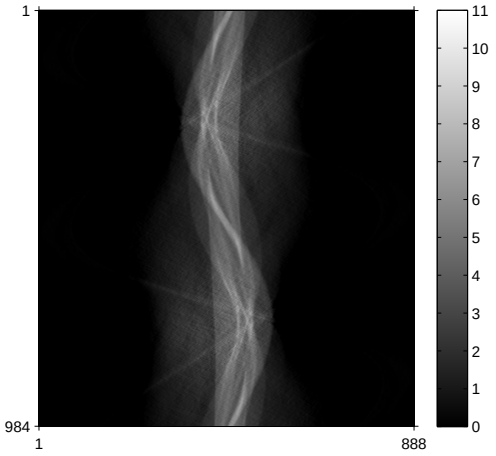

(b) Bone minerals

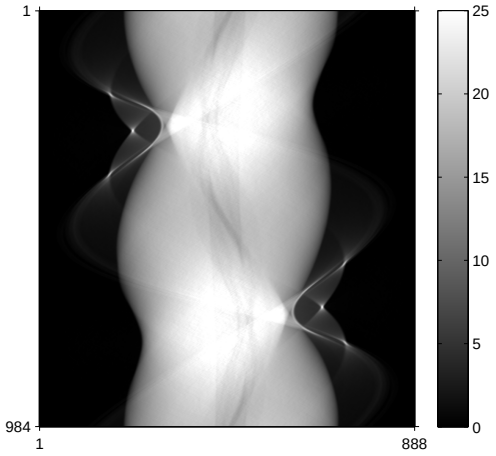

(c) Soft tissue

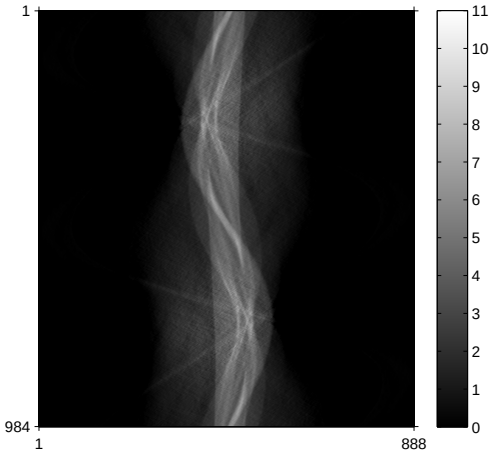

(d) Bone minerals

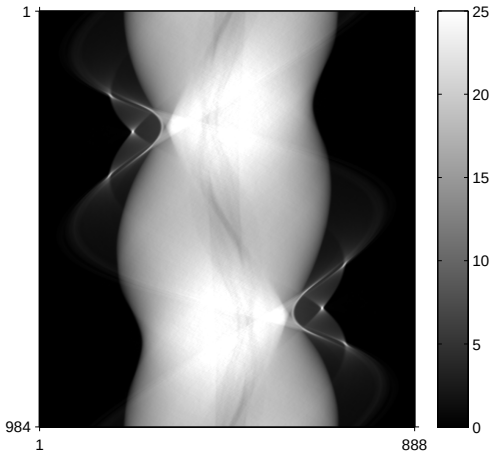

(e) Soft tissue

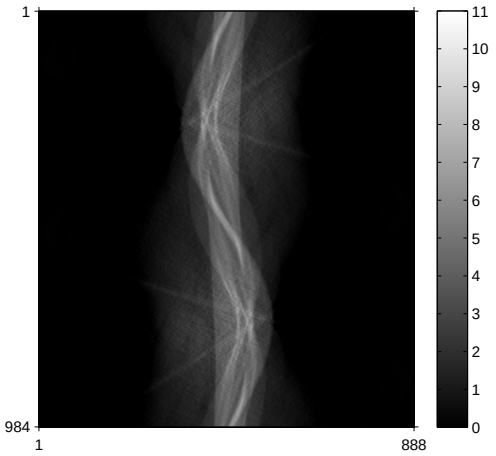

(f) Bone minerals

Fig. 10.6: Sinogram estimates for real phantom scan. First row: conventional method <A>. Second row: previous method <B>. Third row: DELF method <D>.

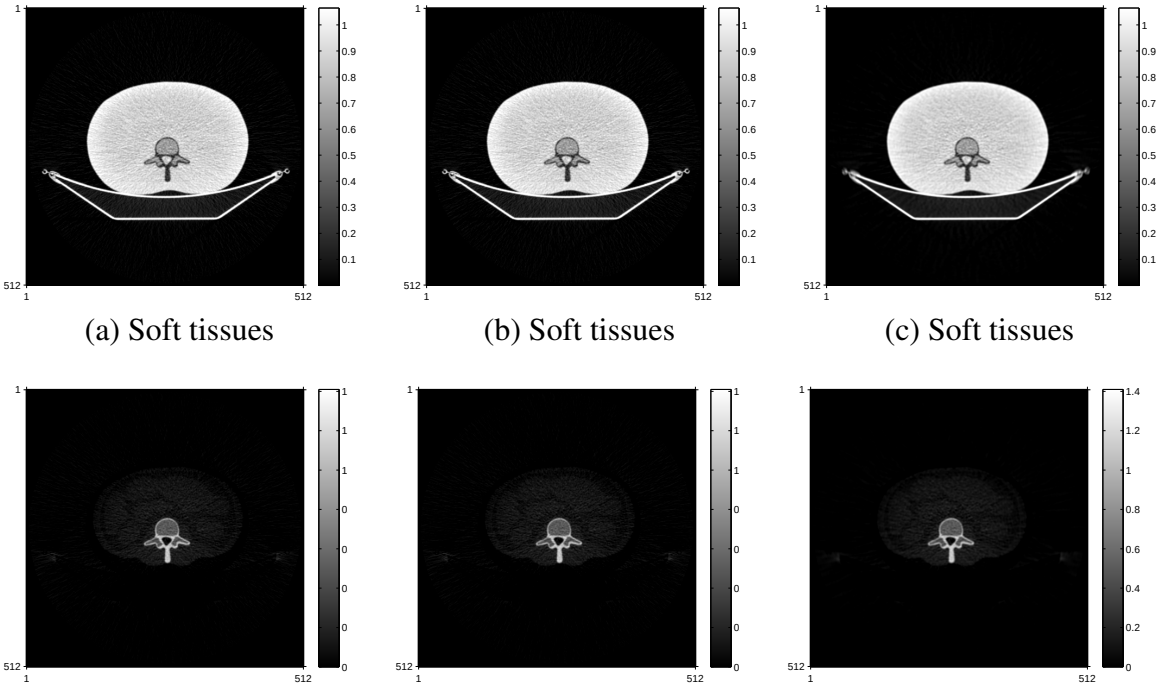

(a) Soft tissues (b) Soft tissues (c) Soft tissues

(d) Bone minerals (e) Bone minerals (f) Bone minerals

Fig. 10.7: Estimated soft tissues and Bone minerals density maps. First column: FBP method <A>. Second column: previous method <B>. Third column: DELF method <D>.

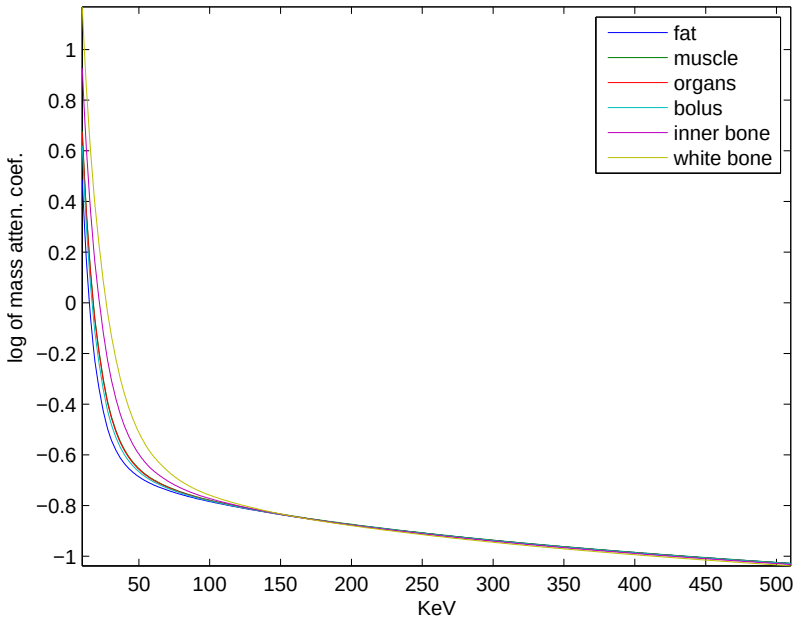

Fig. 10.8: $\log_{10}$ of mass attenuation coefficients of six materials.

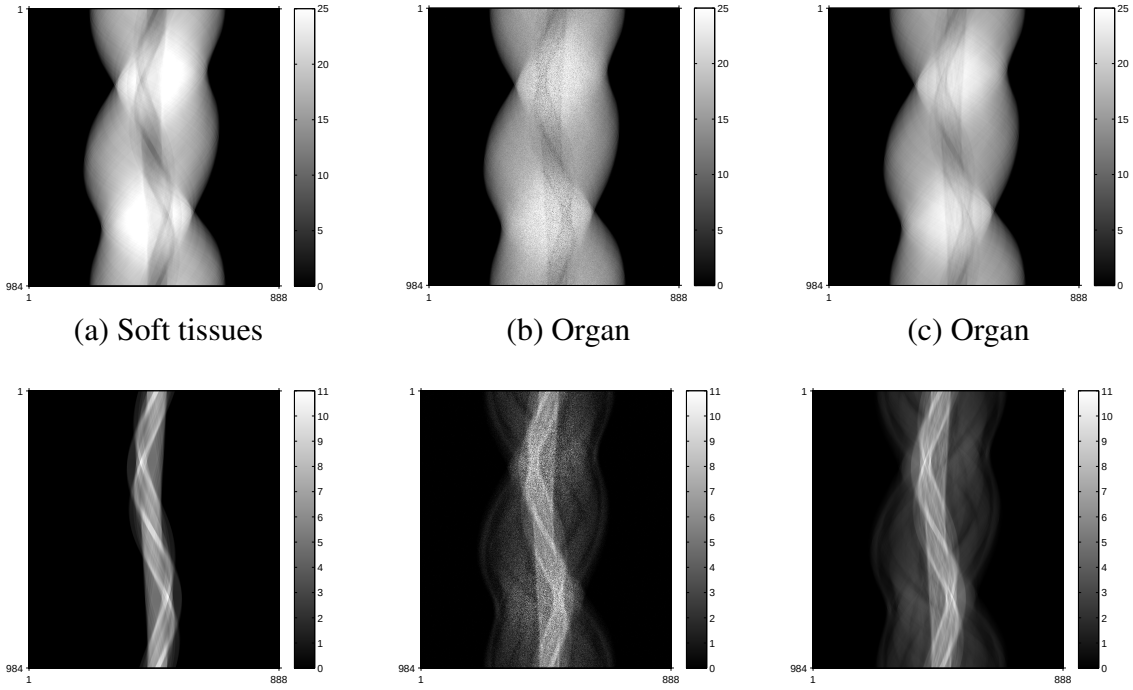

(a) Soft tissues (b) Organ (c) Organ

(d) Bone minerals (e) White-bone minerals (f) White-bone minerals

Fig. 10.9: First column: simulated sinogram of two components. Second column: previous method <B>. Third column: DELF method <D>.

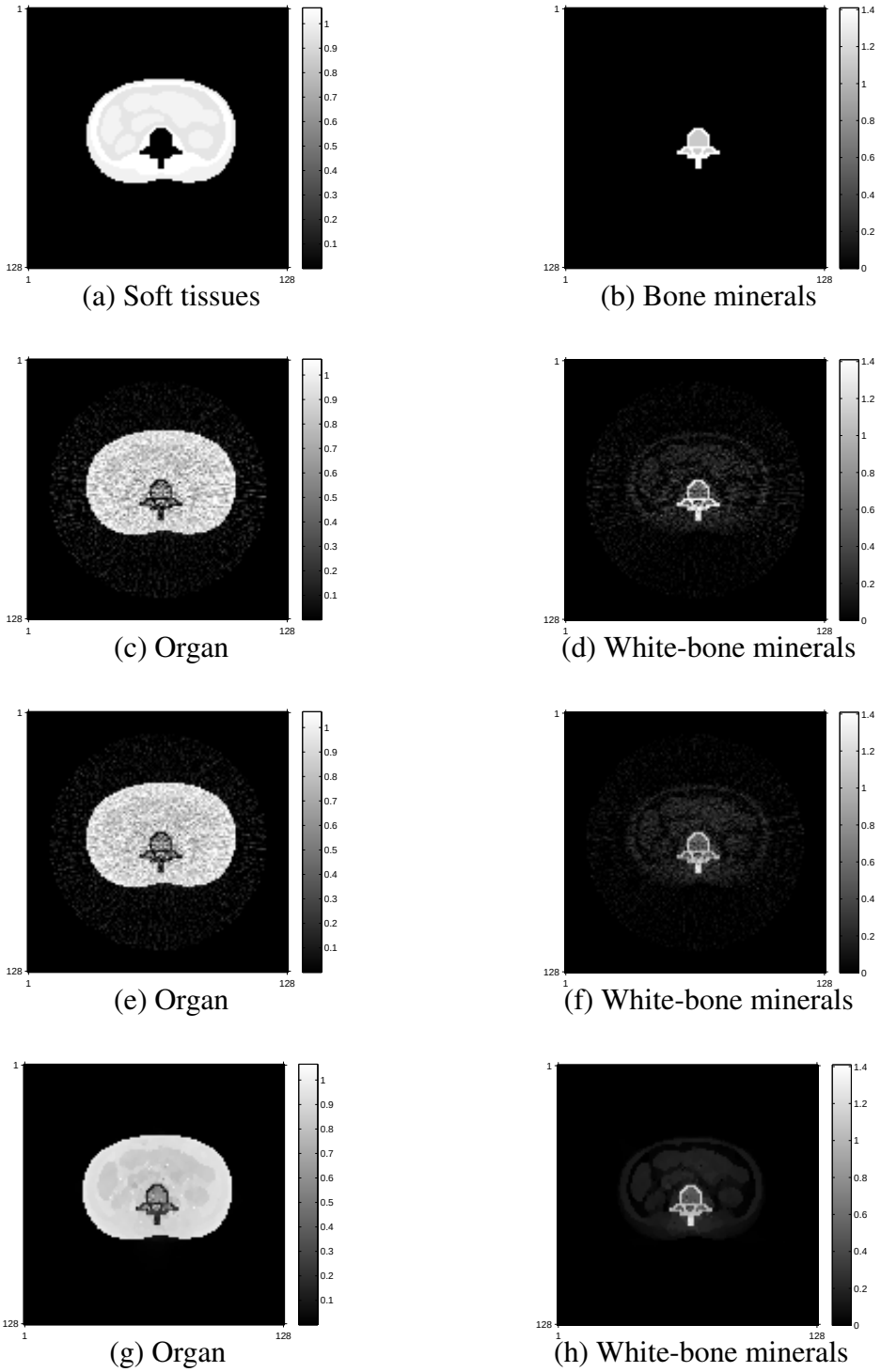

(a) Soft tissues (b) Bone minerals

(c) Organ (d) White-bone minerals

(e) Organ (f) White-bone minerals

(g) Organ (h) White-bone minerals

Fig. 10.10: First row: Two component simulated densities based on the phantom data. Second row: FBP method <A>. Third row: previous method <B>. Fourth row: DELF method <D>.

CHAPTER 11

Conclusion

11.1 Summarize

We have conducted research addressing two major medical imaging areas: MRI and X-ray CT applications. In this dissertation, we investigated iterative regularized algorithms to separate maps of important material components, analyzed the spatial resolution and noise properties, and explored a new roughness penalty to estimate two materials jointly.

Chapter 4 and 5 proposed regularized methods for water-fat decomposition in MRI. Chapter 4 proposed a PL method that includes a regularization term based on the prior knowledge that field maps are usually smooth. After water and fat component estimates were represented in terms of the field map, the PL cost function reduces to a function of the field map only. Hence, we can jointly estimate water and fat components with field map. The proposed method led to improved chemical components estimates compared to the traditional Pixel Independent method and Region Growing method. We also investigated a simple discretized ML estimator for providing good initial images for the proposed iterative algorithm. Chapter 5 presented a k-space method that also considers phase evolution due to field inhomogeneity during MR data acquisition. To reconstruct chemical component maps, the k-space method repeatedly alternates between updating the field map and updating the chemical component estimates. This method allowed us to estimate water and

fat component images based on the MR data directly and the experimental results verified that the k-space method improved estimated chemical component images and estimated field map.

In Chapter 7, 8, and 10, we presented iterative algorithms for DE CT reconstruction. Chapter 7 and 8 proposed a PWLS method that estimates soft tissues and bone minerals' density maps from fast kVp-switching DE data without any interpolation. It allows DE data to be collected in a single rotation and it yields less motion effects which can lead to inconsistency between two sinograms. The proposed method improves images in terms of RMSE and reduced streak artifacts. However, conventional methods (including the PWLS method) estimate the material images or sinograms based on log sinogram data which is sensitive to noise. Therefore, we proposed the DELF method in Chapter 10 to estimate the components' density maps directly from DE CT sinogram data without using any logarithm. The DELF method first estimates the material sinograms and then reconstructs the material density maps. Preliminary simulation results show that the proposed method reduced RMS error compared to other conventional approaches. However, the DELF method did not show a dramatic improvement compared to FBP for real phantom data, presumably due to some form of model mismatch such as scatter or imprecise spectra. Further investigation is required to determine whether or not these are the major reasons for the lack of improvement.

11.2 Future work

- We have proposed model-based DE CT image reconstructions for PET attenuation correction. However, the DELF method was not effective to phantom data. We believe ignoring the effect of background contributions (scatter) in its cost function is the most likely reason for this problem. Future work should consider scatter more

thoroughly.

- We used organ and white-bone as basis materials in Chapter 10. Further research is needed to find better basis materials for representing the six materials in the phantom data.

- The DELF method estimates material density maps with two major steps: first it estimates material sinogram images, second it reconstructs component images based on the estimated material sinograms. In this case, we need two iterative algorithms and we have to find good parameters twice, *e.g.*, roughness penalty parameters, and δ values of the roughness penalty function in equation (10.11). Choosing good parameters is difficult because it could be sensitive to radiation dose. If parameters are too small, the method could not reduce noise well whereas large values for parameters would cause bias. Therefore, we should investigate a DE CT reconstruction method that estimates material density maps from DE CT data directly with only one iterative algorithm [14].

- Furthermore, as a challenge we can try to separate more than three materials by using some constraints such as: density of each material is nonnegative, sum of materials' densities are known (or fixed), or sum of volume or mass fractions of the materials is unity [66].

- In this research, we have focused on estimating the density maps of two materials (such as soft tissue and bone minerals) from DE CT sinograms. These density maps are useful for PET attenuation correction, but they may not be the most suitable images for displaying to a radiologist. Other possible methods for display include synthetic or "virtual" monoenergetic images [40, 42, 66] or images of effective density and effective atomic number Z_{eff} [5, 20, 41, 43, 54, 62]. These alternatives should

be explored in future work.

BIBLIOGRAPHY

BIBLIOGRAPHY

[1] H. Erdoğan and J. A. Fessler. Ordered subsets algorithms for transmission tomography. *Phys. Med. Biol.*, 44(11):2835–51, November 1999.

[2] R. E. Alvarez and A. Macovski. Energy-selective reconstructions in X-ray computed tomography. *Phys. Med. Biol.*, 21(5):733–44, September 1976.

[3] T. Beyer, D. W. Townsend, T. Brun, P. E. Kinahan, M. Charron, R. Roddy, J. Jerin, J. Young, L. Byars, and R. Nutt. A combined PET/CT scanner for clinical oncology. *J. Nuc. Med.*, 41(8):1369–79, August 2000.

[4] P. Charbonnier, L. Blanc-Féraud, G. Aubert, and M. Barlaud. Two deterministic half-quadratic regularization algorithms for computed imaging. In *Proc. IEEE Intl. Conf. on Image Processing*, volume 2, pages 168–71, 1994.

[5] G. Christ. Exact treatment of the dual-energy method in CT using polyenergetic X-ray spectra. *Phys. Med. Biol.*, 29(12):1511–25, December 1984.

[6] N. H. Clinthorne. A constrained dual-energy reconstruction method for material-selective transmission tomography. *Nucl. Instr. Meth. Phys. Res. A.*, 353(1):347–8, December 1994.

[7] A. P. Colijn and F. J. Beekman. Accelerated simulation of cone beam X-ray scatter projections. *IEEE Trans. Med. Imag.*, 23(5):584–90, May 2004.

[8] W. C. Davidon. Variable metric methods for minimization. Technical Report ANL-5990, AEC Research and Development Report, Argonne National Laboratory, USA, 1959.

[9] B. De Man, S. Basu, N. Chandra, B. Dunham, P. Edic, M. Iatrou, S. McOlash, P. Sainath, C. Shaughnessy, B. Tower, and E. Williams. CatSim: a new computer assisted tomography simulation environment. In *Proc. SPIE 6510, Medical Imaging 2007: Phys. Med. Im.*, page 65102G, 2007.

[10] J. A. Fessler. Hybrid Poisson/polynomial objective functions for tomographic image reconstruction from transmission scans. *IEEE Trans. Im. Proc.*, 4(10):1439–50, October 1995.

[11] J. A. Fessler. Mean and variance of implicitly defined biased estimators (such as penalized maximum likelihood): Applications to tomography. *IEEE Trans. Im. Proc.*, 5(3):493–506, March 1996.

[12] J. A. Fessler. *Image reconstruction: Algorithms and analysis*. ?, 2006. Book in preparation.

[13] J. A. Fessler and S. D. Booth. Conjugate-gradient preconditioning methods for shift-variant PET image reconstruction. *IEEE Trans. Im. Proc.*, 8(5):688–99, May 1999.

[14] J. A. Fessler, I. Elbakri, P. Sukovic, and N. H. Clinthorne. Maximum-likelihood dual-energy tomographic image reconstruction. In *Proc. SPIE 4684, Medical Imaging 2002: Image Proc.*, volume 1, pages 38–49, 2002.

[15] J. A. Fessler and W. L. Rogers. Spatial resolution properties of penalized-likelihood image reconstruction methods: Space-invariant tomographs. *IEEE Trans. Im. Proc.*, 5(9):1346–58, September 1996.

[16] R. Fletcher and C. M. Reeves. Function minimization by conjugate gradients. *Comput. J*, 7(2):149–54, 1964.

[17] A. K. Funai, J. A. Fessler, D. T. B. Yeo, V. T. Olafsson, and D. C. Noll. Regularized field map estimation in MRI. *IEEE Trans. Med. Imag.*, 27(10):1484–94, October 2008.

[18] G. C. Giakos, S. Chowdhury, N. Shah, K. Mehta, S. Sumrain, A. Passerini, N. Patnekar, E. A. Evans, L. Fraiwan, O. C. Ugweje, and R. Nemer. Signal evaluation of a novel dual-energy multimedia imaging sensor. *IEEE Trans. Med. Imag.*, 51(5):949–54, October 2002.

[19] X. He, J. A. Fessler, L. Cheng, and E. C. Frey. Regularized image reconstruction algorithms for dual-isotope myocardial perfusion SPECT (MPS) imaging using a cross-tracer edge-preserving prior. *IEEE Trans. Med. Imag.*, 2010. To appear as TMI-2010-0116.

[20] P. W. Henson and R. A. Fox. A relationship between the percentage of calcium by mass and the effective atomic number of regions containing bone. *Phys. Med. Biol.*, 29(8):979–84, August 1984.

[21] D. Hernando, J. Haldar, J. Ma, and Z-P. Liang. A linear prediction approach to joint estimation of water/fat images and field inhomogeneity map. In *Proc. Intl. Soc. Mag. Res. Med.*, page 1629, 2007.

[22] D. Hernando, J. P. Haldar, B. P. Sutton, J. Ma, P. Kellman, and Z-P. Liang. Joint estimation of water/fat images and field inhomogeneity map. *Mag. Res. Med.*, 59(3):571–80, March 2008.

[23] J. Hsieh. Adaptive streak artifact reduction in computed tomography resulting from excessive x-ray photon noise. *Med. Phys.*, 25(11):2139–47, November 1998.

[24] J. H. Hubbell and S. M. Seltzer. Tables of X-ray mass attenuation coefficients and mass energy-absorption coefficients, 1995. National Institute of Standards and Technology http://physics.nist.gov/PhysRefData/XrayMassCoef.

[25] W. Huh and J. A. Fessler. Model-based image reconstruction for dual-energy X-ray CT with fast kVp switching. In *Proc. IEEE Intl. Symp. Biomed. Imag.*, pages 326–9, 2009.

[26] W. Huh and J. A. Fessler. Water-fat decomposition with MR data based regularized estimation in MRI. In *Proc. Intl. Soc. Mag. Res. Med.*, page 2846, 2009.

[27] W. Huh and J. A. Fessler. Iterative image reconstruction for dual-energy x-ray CT using regularized material sinogram estimates. In *Proc. IEEE Intl. Symp. Biomed. Imag.*, pages 1512–5, 2011.

[28] W. Huh, J. A. Fessler, A. M. Alessio, and P. E. Kinahan. Fast kVp-switching dual energy CT for PET attenuation correction. In *Proc. IEEE Nuc. Sci. Symp. Med. Im. Conf.*, pages 2510–5, 2009.

[29] W. Huh, J. A. Fessler, and A. A. Samsonov. Water-fat decomposition with regularized field map. In *Proc. Intl. Soc. Mag. Res. Med.*, page 1382, 2008.

[30] M. W. Jacobson and J. A. Fessler. Properties of MM algorithms on convex feasible sets: extended version. Technical Report 353, Comm. and Sign. Proc. Lab., Dept. of EECS, Univ. of Michigan, Ann Arbor, MI, 48109-2122, November 2004.

[31] W. A. Kalender, W. H. perman, J. R. Vetter, and E. Klotz. Evaluation of a prototype dual-energy computed tomographic apparatus. 1. Phantom studies. *Med. Phys.*, 13(3):334–9, May 1986.

[32] S. Kappler, M. Grasruck, D. Niederlohner, M. Strassburg, and S. Wirth. Dual-energy performance of dual-kVp in comparison to dual-layer and quantum-counting CT system concepts. *In Proc. SPIE 7258, Medical Imaging 2009: Phys. Med. Im.*, page 725842, 2009.

[33] P. Kinahan, J. A. Fessler, A. Alessio, and T. K. Lewellen. Quantitative attenuation correction for PET/CT using iterative reconstruction of low-dose dual-energy CT. In *Proc. IEEE Nuc. Sci. Symp. Med. Im. Conf.*, volume 5, pages 3285–9, 2004.

[34] P. E. Kinahan, A. M. Alessio, and J. A. Fessler. Dual energy CT attenuation correction methods for quantitative assessment of response to cancer therapy with PET/CT imaging. *Technology in Cancer Research and Treatment*, 5(4):319–28, August 2006.

[35] P. E. Kinahan, D. W. Townsend, T. Beyer, and D. Sashin. Attenuation correction for a combined 3d PET/CT scannter. *Med. Phys.*, 25(10):2046–53, October 1998.

[36] P. J. La Riviere, J. Bian, and P. A. Vargas. Penalized-likelihood sinogram restoration for computed tomography. *IEEE Trans. Med. Imag.*, 25(8):1022–36, August 2006.

[37] P. J. La Riviere and P. Vargas. Penalized-likelihood sinogram decomposition for dual-energy computed tomography. In *Proc. IEEE Nuc. Sci. Symp. Med. Im. Conf.*, pages 5166–9, 2008.

[38] J. M. N. Leitão and Mário A T Figueiredo. Absolute phase image reconstruction: a stochastic nonlinear filtering approach. *IEEE Trans. Im. Proc.*, 7(6):868–82, June 1998.

[39] K. Lu, T. T. Liu, and M. Bydder. Optimal phase difference reconstruction: comparison of two methods. *Mag. Res. Im.*, 26(1):142–5, January 2007.

[40] M. Maddah, P. Mendonca, and R. Bhotika. Physically meaningful virtual unenhanced image reconstruction from dual-energy ct. In *Proc. IEEE Intl. Symp. Biomed. Imag.*, pages 808–, 2010.

[41] A. H. Mahnken, S. Stanzel, and B. Heismann. Spectral ρ Z-projection method for characterization of body fluids in computed tomography: ex vivo experiments1. *Acad. Radiol.*, 16(6):763–9, June 2009.

[42] K. Matsumoto, M. Jinzaki, Y. Tanami, A. Ueno, M. Yamada, and S. Kuribayashi. Virtual monochromatic spectral imaging with fast kilovoltage switching: Improved image quality as compared with that obtained with conventional 120-kVp CT radiology. *radiology*, 259(1):257–62, April 2011.

[43] M. R. Millner, W. D. McDavid, R. G. Waggener, M. J. Dennis, W. H. Payne, and V. J. Sank. Extraction of information from CT scans at different energies. *Med. Phys.*, 6(1):70–1, January 1979.

[44] D. G. Nishimura. Principles of magnetic resonance imaging, 1996. Unpublished textbook.

[45] J. Noh, J. A. Fessler, and P. E. Kinahan. Low-dose dual-energy computed tomography for PET attenuation correction with statistical sinogram restoration. In *Proc. SPIE 6913, Medical Imaging 2008: Phys. Med. Im.*, pages 691312:1–10, 2008.

[46] J. Noh, J. A. Fessler, and P. E. Kinahan. Statistical sinogram restoration in dual-energy CT for PET attenuation correction. *IEEE Trans. Med. Imag.*, 28(11):1688–702, November 2009.

[47] V. T. Olafsson, D. C. Noll, and J. A. Fessler. Fast joint reconstruction of dynamic R_2^* and field maps in functional MRI. *IEEE Trans. Med. Imag.*, 27(9):1177–88, September 2008.

[48] J. A. O'Sullivan and J. Benac. Alternating minimization algorithms for transmission tomography. *IEEE Trans. Med. Imag.*, 26(3):83–297, March 2007.

[49] A. R. Pineda, S. B. Reeder, Z. Wen, and N. J. Pelc. Cramer-Rao bounds for three-point decomposition of water and fat. *Mag. Res. Med.*, 54(3):625–35, September 2005.

[50] A. N. Primak, J. C. Ramirez Giraldo, X. Liu, L. Yu, and C. H. McCollough. Improved dual-energy material discrimination for dual-source CT by means of additional spectral filtration. *Med. Phys.*, 36(4):1359–69, March 2009.

[51] S. B. Reeder, A. R. Pineda, Z. Wen, A. Shimakawa, H. Yu, J. H. Brittain, G. E. Gold, C. H. Beaulieu, and N. J. Pelc. Iterative decomposition of water and fat with echo asymmetry and least-squares estimation (IDEAL): Application with fast spin-echo imaging. *Mag. Res. Med.*, 54(3):636–44, September 2005.

[52] S. B. Reeder, Z. Wen, H. Yu, A. R. Pineda, G. E. Gold, M. Markl, and N. J. Pelc. Multicoil Dixon chemical species separation with an iterative least-squares estimation method. *Mag. Res. Med.*, 51(1):35–45, January 2004.

[53] C. Ruth and P. M. Joseph. Estimation of a photon energy spectrum for a computed tomography scanner. *Med. Phys.*, 24(5):695–702, May 1997.

[54] R. A. Rutherford, B. R. Pullan, and I. Isherwood. X-ray energies for effective atomic number determination. *Neuroradiology*, 11(1):23–8, May 1976.

[55] J. R. Shewchuk. An introduction to the conjugate gradient method without the agonizing pain, 1994. http://atol.ucsd.edu/ pflatau/scatlib/conjugate.html.

[56] M. Shirmohammad, M. R. Ay, S. Sarkar, H. Ghadiri, and A. Rahmim. Comparative assessment of different energy mapping methods for generation of 511-keV attenuation map from CT images in PET/CT systems: A phantom study. In *Proc. IEEE Intl. Symp. Biomed. Imag.*, pages 644–7, 2008.

[57] T. E. Skinner and G. H. Glover. An extended two-point Dixon algorithm for calculating separate water, fat, and B_0 images. *Mag. Res. Med.*, 37(4):628–30, April 1997.

[58] D. L. Snyder, C. W. Helstrom, A. D. Lanterman, M. Faisal, and R. L. White. Compensation for readout noise in CCD images. *J. Opt. Soc. Am. A*, 12(2):272–83, February 1995.

[59] J. W. Stayman and J. A. Fessler. Compensation for nonuniform resolution using penalized-likelihood reconstruction in space-variant imaging systems. *IEEE Trans. Med. Imag.*, 23(3):269–84, March 2004.

[60] J. W. Stayman and J. A. Fessler. Efficient calculation of resolution and covariance for fully-3D SPECT. *IEEE Trans. Med. Imag.*, 23(12):1543–56, December 2004.

[61] P. Sukovic and N. H. Clinthorne. Penalized weighted least-squares image reconstruction for dual energy X-ray transmission tomography. *IEEE Trans. Med. Imag.*, 19(11):1075–81, November 2000.

[62] J. Weber and D. J. van den Berge. The effective atomic number and the calculation of the composition of phantom materials. *Brit. J. Radiology*, 42(497):378–83, May 1969.

[63] R. E. Williamson, R. H. Crowell, and H. F. Trotter. *Calculus of vector functions*. Prentice-Hall, New Jersey, 1972.

[64] D. Xu, D. A. Langan, X. Wu, J. D. Pack, T. M. Benson, J. E. Tkaczky, and A. M. Schmitz. Dual energy CT via fast kVp switching spectrum estimation. In *Proc. SPIE 7258, Medical Imaging 2009: Phys. Med. Im.*, page 72583T, 2009.

[65] H. Yu, S. B. Reeder, A. Shimakawa, J. H. Brittain, and N. J. Pelc. Field map estimation with a region growing scheme for iterative 3-point water-fat decomposition. *Mag. Res. Med.*, 54(4):1032–9, October 2005.

[66] L-J. Zhang, J. Peng, S-Y. Wu, Z. Jane Wang, X-S. Wu, C-S. Zhou, X-M. Ji, and G-M. Lu. Liver virtual non-enhanced CT with dual-source, dual-energy CT: a preliminary study. *European Radiology*, 20(9):2257–64, 2010.

[67] Y. Zou and M. D. Silver. Analysis of fast kV-switching in dual energy CT using a pre-reconstruction decomposition technique. In *Proc. SPIE 6913, Medical Imaging 2008: Phys. Med. Im.*, pages 691313–12, 2008.